Alma Mater Studiorum – Università di Bologna

DOTTORATO DI RICERCA IN

Geofisica

Ciclo XXXI

Settore Concorsuale: 04/A4

Settore Scientifico Disciplinare: GEO/10

A new approach for landslide modelling: applications to the 1783 Scilla event and to potential Marsili volcano collapses

Presentata da: Glauco Gallotti

Coordinatore Dottorato	**Supervisore**
Prof. Nadia Pinardi	**Prof. Stefano Tinti**

Esame finale anno 2019

“Così la neve al sol si disigilla;

così al vento nelle foglie levi

sì perdea la sentenza di Sibilla”

Dante, Paradiso XXXIII

Abstract

In this study, we present a new 2D numerical model (UBO-Inter) capable to simulate the motion of a landslide down generic surfaces. The body is represented by N point masses that can be seen as the projection on the sliding surface of the center of mass of the elements the system is discretized into. The masses are strictly adherent to the surface and interact with each other by means of inner forces that involve pairs of point masses. The inner force pattern can be schematized by a mass grid where the grid nodes are the point masses and the pairs of interacting masses are connected through edges. The external forces acting on the point masses are: gravity, which is the driving force, the reaction force of the surface, basal friction and drag exerted by the environmental fluid (namely water, since the air drag is negligibly small).

After a short introduction depicting the state-of-the-art knowledge and the present understanding of landslide phenomena and processes in Chapter 1, and after touching the main approaches for their numerical simulation in Chapter 2, we give a formal description of the problem in Chapter 3. The N point-mass system is governed by a set of differential equations that are solved through a fourth-order Runge-Kutta scheme. Further, we present a first set of applications on simple-geometry cases that can be solved analytically and that can be used as a first benchmark to the code. For these cases we consider only inner forces that keep the distance between the interacting pairs of point masses constant and study force pattern based on Delaunay triangulations. This kind of inner forces are adequate to simulate the motions of semi-rigid systems. To deal with deformable landslides, in Chapter 4 we introduce mass grids based on force patterns formed of quadrilaterals (rather than triangles) and consider two kinds of inner forces: forces keeping constant the distance between the interacting pairs (like in the previous cases) acting on the sides of the quadrilateral, and elastoplastic forces acting on the diagonals, that account for diagonal shortening and/or lengthening to a certain extent. In Chapter 5, Section 5.2, we test the UBO-Inter model on the 1783 Scilla tsunamigenic landslide, a historical case that serves as a benchmark due to the abundance of coeval data and recent observations on the onshore detachment niche, run-out distance and offshore deposits. Eventually, in Section 5.3 we investigate three scenarios of mass movements down the eastern flanks of the Marsili submarine volcano (located in the southern Tyrrhenian Sea). They are relevant because cover a broad range of slide volume, from small to huge, and different types of movements. We outline that this is the first time that slope instabilities of Marsili are given specific attention. Though in this thesis we do not address the tsunami generation and propagation problem, Marsili mass failures have the potential to be tsunamigenic and hence our study may be also seen as a significant contribution to tsunami hazard assessment in a broad area of the Tyrrhenian region. All scenarios of the last two Sections have been also modeled by means of the code UBO-Block (1D and 2D versions for the Scilla and Marsili scenarios respectively), that is a code developed by the Tsunami Research Team of the University of Bologna based on landslide block-partition and a Lagrangian approach. The comparisons show that results are consistent.

CONTENT

Chapter 1

1. Overview of landslide phenomena

1.1. Introduction

Landslides are important natural agents that shape mountainous areas and redistribute sediment in gentler terrain. Much of the present Earth's landscape has been extensively sculpted by episodic large landslides. Subtler, but significant modifications have also been made by frequent, smaller-scale mass movements. In general terms, we can define a landslide as a variety of processes that result in the downward movement of materials composed of natural rocks, soil, artificial fill, or combination of these materials. The displaced mass can move in several different ways. Gravity is always the primary driving force, and water can play a very important role. The conditions that permit gravity to overcome the inertial forces of friction and cohesion (that hold a slope together) include several kinds of processes such as variations in soil/rock water content, moisture levels, freezing of ice in jointed rock, seismic/volcanic activity, destabilizing human activities, etc. Broadly speaking, heavy rains and earthquakes are the cause of the major landslides. Several excellent summaries and books have been published on prediction, analysis, and control of landslides, particularly from an engineering or geotechnical perspective [*Turner and Schuster*, 1996; *Abramson et al.*, 2001; *Cornforth*, 2005]. Additionally, several significant books have focused on specific landslide processes and environments [*Brunsden*, 1985; *Dikau et al*., 1996].

Another important section of studies is focused on the hazard assessment and prediction methods. Essentially, methods of assessing landslide hazards can be roughly divided into four categories: terrain stability mapping [e.g. *Ives and Messerli*, 1981; *Kienholz et al*., 1984; *Howes and Kenk*, 1988]; simple rainfall-landslide and earthquake-landslide relationship [e.g. *Nelson Caine*, 1976; *Keefer et al*., 1987; *Larsen*, 1993]; multi-factor, empirical landslide hazard assessments [e.g. *Gupta and Joshi*, 1990; *Pachauri and Pant*, 1992]; distributed, physically based models [e.g. *Miller*, 1995; *Wu and Sidle*, 1995]. Some of these methods are more amenable to assessing relative landslide hazard at regional scales, others can be used as predictive tools for more specific sites, while others can be used to develop real-time warning systems. Since this work is focused on the dynamics of landslides, hazard assessment will not be treated in detail.

1.2. Classification system

To introduce the various classification systems, a brief description of landslides morphology is required.

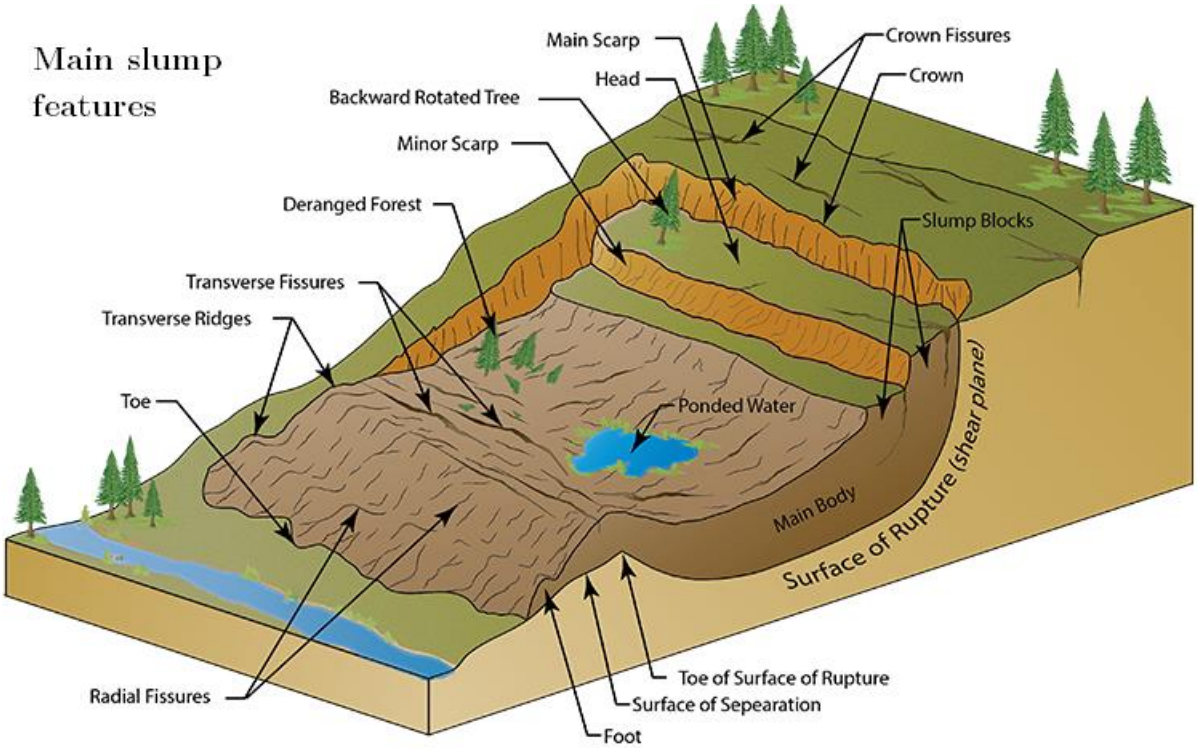

Figure 1.1 Schematic diagram of a typical slump in a forested area [Adapted from *Idaho Geological Survey*].

As is shown in Figure 1.1, we can define typical landslide features:

1. Crown: the practically non-displaced material still in place and adjacent to the highest parts of the main scarp.

2. Main scarp: a steep surface on the undisturbed ground at the upper edge of the landslide, caused by the movement of the displaced material away from the undisturbed ground.

3. Top: the highest point of contact between the displaced material and the main scarp.

4. Minor scarp: a steep surface on the displaced material of the landslide produced by differential movements within the displaced material.

5. Main Body: the part of the displaced material of the landslide that overlies the surface of rupture between the main scarp and the toe of the surface of rupture.

6. Foot: the portion of the landslide that has moved beyond the toe of the surface of rupture and overlies the original ground surface.

7. Toe: the lower, usually curved margin of the displaced material of a landslide. It is the most distant from the main scarp.

8. Surface of Rupture: the surface which forms (or which has formed) the lower boundary of the displaced material below the original ground surface.

9. Toe of the Surface of Rupture: the intersection (usually buried) between the lower part of the surface of rupture of a landslide and the original ground surface.

10. Surface of Separation: the part of the original ground surface overlain by the foot of the landslide.

Furthermore, geometrical characteristics of landslides are generally defined as:

1. Total length L: the minimum length from the tip of the landslide to the crown.

2. Total width W: the distance between the landslide lateral borders.

3. Total depth D: the maximum vertical length from the landslide summit to the sliding surface.

4. Length of the displaced mass L_d: minimum distance from the tip to the top.

5. Width of the displaced mass W_d: maximum breadth of the displaced mass perpendicular to the length of the displaced mass.

6. Depth of the displaced mass D: the maximum depth of the displaced mass, measured perpendicular to the plane containing W_d and L_d.

From a geological point of view, several materials and soil characterizations have been defined. Essentially, a classification system can be taxonomic, implying a hierarchy of descriptors to form a branch-like structure, or it can be a filing system. In this case, different items are placed into classes based on various attributes. Alternatively, a typological classification is particularly useful. This is based on selected features and is designed to present solutions at the problem at hand. Slope movements have been classified in many ways, with each method having some usefulness or applicability related to the recognition, avoidance, control or correction of the hazard. The most widely used classification, due to *Varnes* [1978] (Figure 1.2) distinguishes five types of mass movements:

1. Falls: the sliding mass is free to fall over a steep slope. Velocity range can reach values of a free-falling body.

2. Topples: rotational motion of rock blocks around a hub located under the blocks or on the blocks base. The motion is generally gravity induced. The dimensions can reach considerable values (up to $10^3\ m$).

3. Slides: movement parallel to planes of weakness and occasionally parallel to the slope. The motion is caused by shear stresses acting on inward surfaces. Generally, two types of slides are defined: rotational and translational. In the first ones, the failure plane is typically concave, and the movement is extremely slow (less than $1\ m/day$). The second ones occur on existing disruption surfaces with an inclination equal (or lower) to the slope one. The sliding mass can go through lots of kilometres, reaching a velocity of $50\ m/s$ in the rocks slide.

4. Spreads: huge lateral motion over a plastic-like surface. The movement is generally slow ($0.1\ m/min$ -$1\ m/day$)

5. Flows: viscous to fluid–like motion.

Other classes are defined as combinations of these principal types along with the type of material: bedrock (rock underlying the surface), coarse soils and predominately fine soils. Further subdivision is based on the speed of movement. When a landslide passes through several phases as it progresses downslope, it can be considered complex, even if one type usually predominates in different parts of the moving mass or at different times during the period of displacement. An example relevant for this

thesis is the 1783 Scilla landslide that can be classified as a complex movement. Nevertheless, in the subaerial part, it possesses the features of a rock avalanche, as we will show later on in this thesis. Several modifications of the original *Varnes* [1978] classification have been made: [*Cruden and Varnes*, 1996, *Brunsden*, 1985]. *Keefer* [2002] employed similar principles and terminology as *Varnes* [1978] to classify earthquake-induced landslides based on material type (soil or rock), type of movement (disrupted or coherent), and other characteristics (e.g. velocity, depth, water content). Keefer's classification includes three main categories of landslides:

1. Disrupted slides and falls.

2. Coherent slides (e.g. slumps, earthflows)

3. Lateral spreads and flows.

Moreover, based on the frequency of occurrence during 40 earthquakes (M 5.2 to 9.2), *Keefer* [2002] categorized landslides as very abundant ($> 2500\ event^{-1}$), abundant ($250 - 1000\ event^{-1}$), and uncommon.

Sidle and Dhakal [2002] proposed another classification that recognizes the importance of combinations of mass displacements and follows the terminology employed by *Varnes* [1978] as much as possible. Five functional categories of mass movements are described:

1. **Shallow, rapid landslides.** Debris slides and avalanches are typical shallow movement types in steep (> 25° slope) terrain. Soils are characteristically $< 5m$ deep and have low cohesive properties. The shallow soil mantle overlies either bedrock or another permeability layer (e.g., glacial or marine till) that acts as a failure plane. This plane is generally oriented parallel to the soil surface, allowing the use of the infinite slope model. These landslides are typically longer than their width, have length to depth ratio < 0.1 [*Wentworth*, 1943; *Skempton and Hutchinson*, 1969; *Cruden and Varnes*, 1996] and initiate on slopes that are typically either concave or linear [*Swanston*, 1969; *Gao*, 1993; *Palacios et al.*, 2003]. Sequence of linked debris slides, avalanches, and flows are major sources of sedimentation in mountain streams. Typically, this kind of landslides are generally triggered by rainstorms, rapid snowmelt, earthquakes, or combinations of these factors. Also, lahars (debris flows that initiate on volcanic slopes in recently deposited ash or debris) belong to this category (see Figure 1.3).
2. **Rapid, deep slides and flows.** Rapid, deep slides and flows include large debris slides, debris flows, dry flows, bedrock slides, rock avalanches and certain block glides and rapid earthflows. Some of the terrain and material characteristics are like those of shallow, rapid landslides but responses to triggering factors often differ. Anyway, the main difference with respect to the previous category is the slide thickness ($> 5m$). Furthermore, the sliding mass often include a significant proportion of weathered or fractured bedrock. The main trigger mechanisms are typically long rainfall periods or strong earthquakes. In fact, a strong ground motion is sometimes required to initiate failures in deeper regoliths [e.g. *Shoaei and Ghayoumian*, 2000].

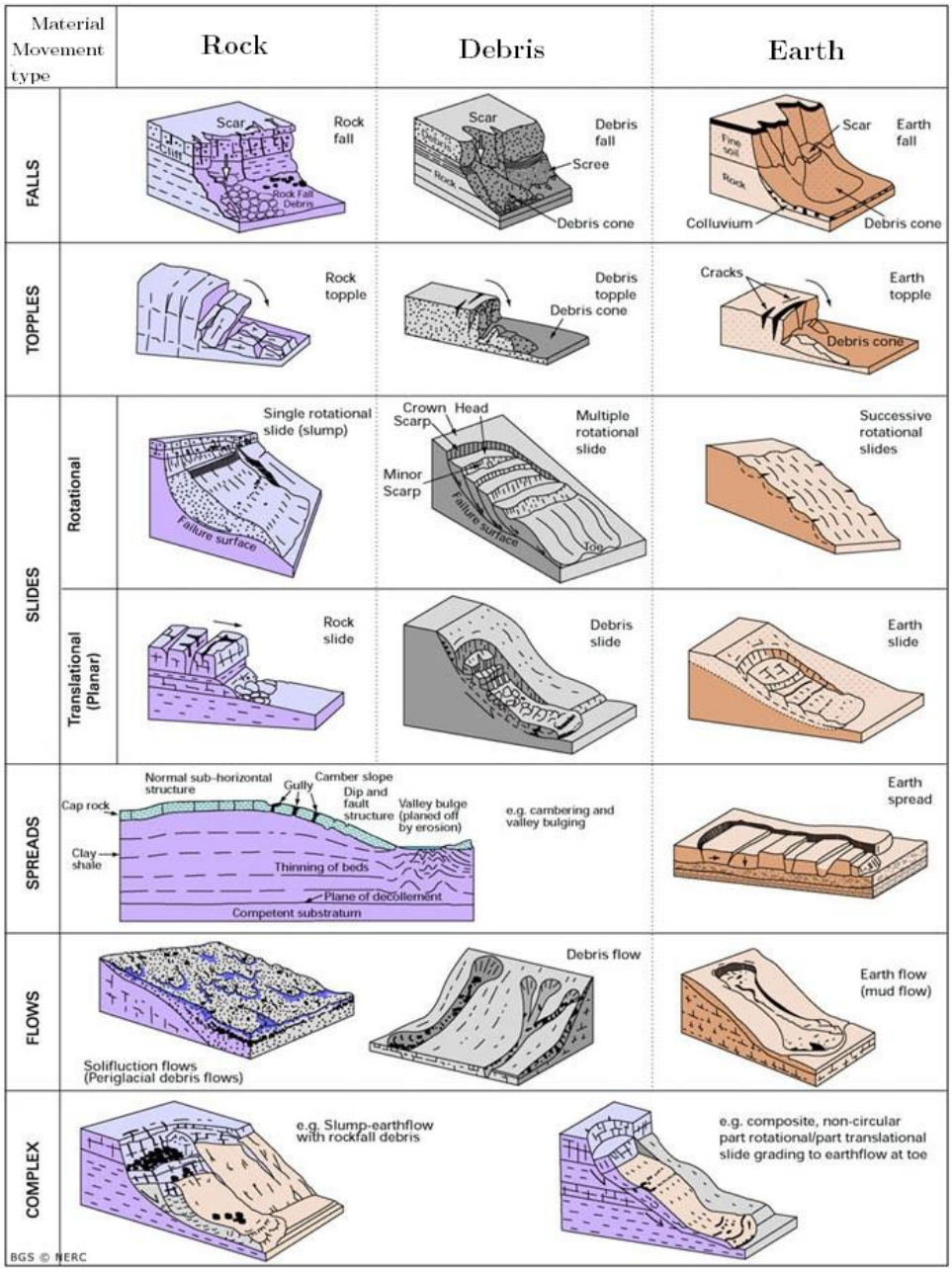

Figure 1.2 Varnes [1978] landslides classification system [Adapted from *British Geological Survey*].

3. **Slower, deep-seated landslides.** The deep-seated landslides include slumps, earthflows and lateral spreads that move at rates generally $< 1m\ day^{-1}$. Both active and dormant slides characteristically occur in gently sloping topography that is often hummocky with immature drainage system [*Swanston and Swanson*, 1976; *Ocakoglu et al.*, 2002]. Failure occurs in deep, heavily weathered clay–rich soils or regoliths that exhibit plastic behaviour over a range of water contents. Slumps and earthflows are quite often a coupled phenomenon: the initial movement is typically a rotational slump, and subsequent downslope movement of the mass is by earthflow [e.g. *Okunishi et al.*, 1999; *Rohn et al.*, 2003]. The dimensions of these displacements are generally larger than shallow rapid landslides and move in response to seasonal or at least multiday accretion of groundwater related to inputs from rainfall or snowmelt: once a critical level of groundwater is present, movement accelerates rapidly [*Furuya et al.*, 1999; *Coe et al.*, 2003]. It is important to underline that, despite their slower rates, deep-seated mass movements are responsible for the transport of large volumes of

sediment to streams and rivers in certain regions [*Sasaki et al*., 2000]. Lateral spreads (Figure 1.4) can be defined as the lateral displacement of a large mass of cohesive rock or soil overlying a deforming mass of soft materials [*Dikau et al*., 1996; *Cruden and Varnes*, 1996]. Movement is initiated by high internal pore water pressure from rainfall or snowmelt or by earthquakes.

Figure 1.3 Lahar formed after the 1982 Mount St. Helens eruption in Washington State, USA, as an example of shallow and rapid landslide. The red arrows depict the main directions of motion [Adapted from *Tom Casadevall*, USGS].

4. **Slow flows and deformations**. These displacements occur as soil creep that is not properly a failure per se, but a plastic deformation of the soil mantle. Active soil creep is often associated with slump earthflows; thus, terrain characteristics are the same. Movement rates typically decrease with depth [*Swanston*, 1969; *Sonoda*, 1998] and have values of the order of millimetres per year.

Figure 1.4 Lateral spreads at Hebgen Lake near West Yellowstone, USA. Shaking from the M_w=7.2 August 18, 1959, earthquake. The red arrows depict the main directions of motion [Adapted from USGS].

5. **Superficial mass wasting.** This motion is generally not considered together with landslides. However, it is a gravity-driven process that is technically a mass movement. In fact, dry ravel and dry creep belong to this category even if they are superficial processes. They involve the downslope of individual soil grains, aggregates, and coarse fragments by rolling, sliding or bounding. The main cause of these mechanisms can be found in the loss of interlocking frictional resistance among soil aggregates or grains [*Pradhan and Siddique*, 2019]. These are a less perceptible type of erosion and usually transport far less sediment compared to other mass wasting processes.

The classifications just introduced are useful tools to quickly understand the kind of motion related to the various materials. In this thesis work, we will focus attention on the rapid motion of rocks. Overall, the slide cases we will study can be considered as rock avalanches of various depths.

1.3. Earthquake-induced landslides

There are several natural factors influencing landslides, but in this section we will focus our attention on seismicity. Studies have shown that they often occur in convex topography because convex landforms respond strongly to earthquake motion [e.g., *Harp et al.*, 1981; *Murphy*, 1995; *Okunishi et al*., 1999]. It's generally very difficult to associate earthquake-induced motion to landslide mass displacement because quakes exert very complex stresses on slopes since the seismic loads vary dynamically. Virtually, all types of landslides can be associated with different magnitude earthquakes in various settings. Furthermore, quakes can also reactivate dormant or slow-moving landslides. From a physical point of view, the propagation of seismic waves causes an acceleration of the soil mantle. The cyclic loading and unloading of soils during earthquakes depend on many factors and exert major

stresses that can cause landslides. Moreover, cycling loading of regoliths may generate high pore water pressures that trigger landslides. Many factors related to earthquakes and the settings in which they propagate affect the number, size and type of landslides. Even if the intrinsic physical features of the earthquake (magnitude, focal depth, etc.) are fundamental, factors related to the environments in which shaking occurs are essential. The most crucial are:

1. Inert stability of the potential failure sites.
2. Existence of old or dormant landslides.
3. Vegetation and land use.
4. Orientation of potential failures in relation to the earthquake epicentre.
5. Orientation of existing faults with respect to the direction of seismic wave propagation.
6. Regolith wetness.
7. Slope gradient and other topographic factors.

All these factors, at least at some degree, are quite difficult to separate. Broadly speaking, rock falls, rock slides, soil falls, and disrupted soil slides are triggered by the weakest seismic activity; deep-seated slumps and earthflows are generally initiated by stronger (and probably of longer duration) seismic activity; lateral spreads, debris flows and subaqueous landslides require the greatest seismic activity [*Keefer et al.* 1987, *Keefer*, 2002]. Compared to other land shapes, convex landforms exhibit stronger seismic amplification. Particularly, mountain ridges shake strongly during earthquake and shear failure may occur on these slopes, triggering a landslide [*Harp and Jibson*, 1996; *Tang and Grunert*, 1999; *Khazai and Sitar*, 2004]. This phenomenon is generally called topographic effect. Studies have demonstrated that significant amplification occurs when the wavelength of the seismic wave is the same as the length of the land shape [*Nishimura and Morii*, 1984]. Intensification of ground acceleration by as much as 75% can occur, but in areas of complex topography the overall influence of ground motion cannot be easily predicted. Evidence have shown that scarps that face away the direction of incoming seismic waves are most prone to landslides. In other cases, large topographic effects have been observed at sites where slope gradient changed and on convex land shape along streams [*Harp et al.*, 1981]. However, despite the many empirical investigations that associate topographic effects with earthquake-induced landslides, the degree to which such effects amplify seismic motion and the influence of this amplified motion on the resultant stress have yet to be clarified, due to the lack of detailed seismic observations in mountainous areas. Hence, to determine the degree of the topographic effect, behaviour of slopes during an earthquake is generally quantitatively modelled to estimate the acceleration response [*Havenith et al.,* 2003]. Results have proved that a large response to the acceleration waveform input is observed from the bottom of the model in a direction orthogonal to the ridge line. Furthermore, the amplification can be caused also by the contact of jointed rock masses [*Rovelli et al.,* 2002; *Lenti and Martino,* 2012]. Based on seismometric records, this effect can be identified in terms of mono-frequential wave packages of recorded earthquakes; of clear frequency peaks in both horizontal to vertical spectral ratios and site-to-reference spectral ratios; of directional effects in energy azimuthal distribution. Another factor influencing earthquake-induced landslides is represented purely by geologic aspects. In some areas of Japan and southern Italy, numerous earthquake-induced landslides occurred in weathered and foliated rocks formed mainly by quartz and mica (‘biotite gneiss’) [*Murphy*, 1995]. Moreover, many studies have noted the susceptibility of poorly consolidated sedimentary rocks and sediments to landslides during earthquakes.

1.4. Tsunamigenic landslides

Tsunamis are long waves induced by a strong and quick impulse that can propagate in an ocean basin also for long distances. Basically, tsunami waves are generated by a rapid displacement or motion of large volumes of water. The main sources of such events are submarine earthquakes, volcanic eruptions and subaerial or submerged landslides. The tsunami wavelength in deep waters can be very considerable (hundreds of kilometres) with respect to its elevation (few centimetres up to one meter, or exceptionally some meters) and tsunami velocity may be in the order of hundreds of kilometres per hour. When a tsunami approaches shallower waters, due to mass and energy conservation, it slows down and increases its elevation. Due to its time and space scale, it is easy to imagine how potentially destructive and dangerous this phenomenon can be. Since the focus of this study is the dynamics of landslides we will touch only marginally the capability of landslides to produce tsunami waves. There are well-documented cases of large landslides falling into water and causing large localized waves. One of the most spectacular examples was the Lituya Bay (Alaska) landslide on July 10, 1958. The landslide, triggered by an earthquake, fell into a narrow fjord and caused a wave that climbed up the opposite side of the fjord up to the maximum height of 520 m. However, when the wave reached the open ocean, its amplitude was much lower [*Fritz et al.*, 2009]. The Vajont reservoir disaster in 1963 [*Trollope*, 1980; *Zaniboni and Tinti*, 2014, 2018] represents another event of this nature. In this case, the northern flank of Mount Toc collapsed into the below basin (Figure 1.5), and the water was suddenly pushed away over the opposite side, without a real propagation into the water basin. Then most of the water flow overtopped the reservoir dam and reached catastrophically the valley below it (Valle del Piave) causing about 2000 fatalities. Such kinds of water displacements are physically treated in a way different from long waves propagating into the ocean. Anyhow, we define both phenomena as "tsunami" waves due to their common origin.

Despite the landslide amplitude and source, the following three stages in the evolution of the landslide generating tsunami can be distinguished:

I. Triggering of slope failure

II. Post-failure landslide evolution

III. Tsunami generation and propagation.

Slope failure (stage I) occurs primarily on open continental-margin slopes and in the active river deltas in under, and normally consolidated, sandy and clayey sediments. At the onset of stage II, when the slide breaks out, it starts moving. During the sliding process, some landslides mobilize into flows and turbidity currents, whereas others remain slides or slumps with limited deformations and displacements [*Locat and Lee*, 2002]. Interacting with water, the slide generates water waves (stage III), that propagate through the water towards the shore and offshore. Commonly, three different problems for the analysis of tsunami waves are distinguished: wave generation at the source; wave propagation in the open water; wave approaching the coast and running up into the shore. While stages II and III of the evolution processes are usually viewed as dynamic processes, the conventional analysis of the slope failure (stage I) focuses commonly on the final limiting equilibrium state, which is a static condition. Researchers have been studying the process of tsunami generation by submarine and subaerial landslides mainly through numerical methods [*Harbitz*, 1992; *Pelinovsky and Poplavsky*, 1996; *Ward*, 2001; *Tinti and Piatanesi*, 1997; *Satake*, 2001; *Murty*, 2003; *Dutykh and Dias*, 2009]. To explain higher maximum velocities, models accounting for the initial acceleration from earthquakes have been developed [e.g., *Harbitz*, 1992]. However, it is known that this is not

always legitimate. For instance, in the Aitape 1998 event, the submerged landslide occurred some 10−15 min after the earthquake [*Davies et al.*, 2003]. Consequently, earthquake acceleration cannot always explain an initial landslide velocity. Overall, the whole process is complex, and every case needs to be studied ad hoc to be properly described. In the 2002 Stromboli, Italy, volcano eruption [e.g., *Tinti et al., 2005*] two different slides induced a series of tsunami waves. The first one was mainly submarine, while the second detached about 500 m above sea level. Different sliding volumes and impact velocities produced different kinds of waves that hit the surrounding coasts in different ways. In fact, peculiar characterizations must be done on the tsunami fronts direction, that is strongly dominated by the bathymetry. Even if larger and thicker landslides generally produce larger tsunamis, geometry and sliding speed can induce effects that influence the tsunami propagation and incidence on the coastline.

Figure 1.5 Vajont reservoir, Italy, after the 1963 catastrophic mass displacement [credit: USGS].

1.5. Submarine volcanoes

The structures or the places that allow for the escape of gases, solid, and various rocks from the Earth's mantle into the surface are generally considered *volcanoes*. Due to these material ejecta, the typical shape of a volcanic structure is a hill- or a mountain-like one. Such eruptions are somehow periodic in all the systems, but the eruption kind and timing can vary drastically from a structure to another. Several books on the description of these processes can be found in the literature [*Sigurdsson et al,* 1999; *Sigurdsson,* 2015; *Dobran,* 2001; *Fagents et al.*, 2013]. The formal explanation of the volcanic system is not the object of this study. Hence, we will introduce the general frame just in terms of qualitative characteristics, with attention to the submarine structures since some of the scenarios treated in this thesis deal with a submarine volcano.

Most of the volcanoes on Earth are submarine, typically located on the midocean ridges, such as the Mid-Atlantic Ridge that extends from the Arctic to the Antarctic. Overall, volcanic eruptions are easily produced near the edges of the plates or along the subduction zone. Volcanic structures can be divided into three main kinds:

1. **Rift volcanoes.** Produced along the spreading plate boundaries. They are generally beneath the water, with some exceptions in Iceland and in the rift valley of East Africa. Their formation is due to the passive spreading where the lithosphere is weaker because of tectonic forces.
2. **Subduction volcanoes.** These structures are the consequence of the slow collision of converging plates. They generally occur in regions where one plate overcomes the other plate. Typical examples of such nature are the island arcs of New Zealand, the southern Pacific, the Philippines and the Andes Range.
3. **Hot-spot volcanoes.** This kind of volcanoes is produced from the so-called magma plumes (large batches of magma) that rise from the overlying plate. The nature of the uprising convective motion that forms the hot-spot is still poorly known. Typical examples are the Hawaii, Azores and Galapagos volcanoes.

Despite the origin of the volcano dome, each eruption ejects gases and rock materials that can have solid or liquid forms. We commonly refer to *magma* as the melted rock material in the volcano that becomes lava once it reaches the surface. The nature of the eruption is strongly related to the physical and rheological characteristics of the magma mixture, crystal and gases that interact with air or water once they reach the surface [*Cas and Wright,* 1993]. Once the rising magma pressure is reduced, it liberates gas bubbles that can rapidly grow and obstruct the flow passage. At this stage, several changes in the flow regime can occur and the flow itself can be blocked in the so-called *magma fragmentation zone*. Thus, the different chemical and physical characteristics of the magmas lead to different kinds of eruption processes.

Volcanoes related to subduction zones generally contain large quantities of volatiles, produced from the mix between magma and seafloor sediments. In other cases, due to pressure and temperature conditions, silica-rich magmas concentrating a large amount of gas can be found. The interaction between magma and water can lead to *explosive hydrovolcanic* eruptions. Anyhow, most submarine eruptions in deep water are mainly basaltic, resulting in a more effusive eruption style, also because of the high pressure of the ambient. In fact, even if the interaction between water and magmas can produce strong explosions, when the critical water pressure is reached (about 3 km water depth), steam explosions are practically impossible. Thus, the nature of an eruptive site controls the eruptive behaviour, at least in the deeper basin. It must be pointed out that no submarine lava flows have ever been recorded at great depths.

To the purpose of this study, it is important to properly describe the seamounts origin and the island building process. Overall, seamounts of volcanic origin are the most abundant volcanoes on Earth, even if their origin and evolution are still poorly understood [e.g. *Sigurdsson*, 2015; *Hunt and Jarvis*, 2017]. The morphology of such structures is indeed manifold. Their shapes are controlled by a series of characteristics: size, geometry and temporal evolution of the magmatic conduits; magma chemical properties; developments of local craters; general topography; and surrounding gravitational stresses. The large stresses applied to the oceanic crust by the volcanic island, in response to magma ascension, can lead to relevant phenomena of subaqueous instability. The growth and evolution of this kind of structures are hence often related with mass displacement of various sizes [e.g. *Krastel et al.*, 2001; *Watt et al.*, 2015; *Hunt and Jarvis*, 2017]. Generally, the upward growth stages are characterized by an increase of the vesicularity of lava flows, of the proportion in volcaniclastics (reworked pyroclastic rocks), and of the percentage of mass-wasting deposit. Following these criteria, three growth stages have been depicted: deep-water stage; intermediate water/shallowing stage; and emergent/island stage. The uplift process of the La Palma (Canary Island, Spain) basement is a good example of this theoretical division (Figure 1.6): in panel A, the beginning of volcanic activity with the intrusion of feeder dykes is depicted. At this stage, the eruption style is just effusive. In the deep-water stage (B) the bulk of the seamount is forming with several mass displacement processes. This stage ends with the beginning of explosive eruptions, which leads to the intermediate phase (C). Most of the clastic materials produced are redeposited by debris flows on the volcano flanks. The upward growth of the system above sea level leads to the island stage (D). The phreatomagmatic explosions decrease only when the vent area becomes isolated from the sea.

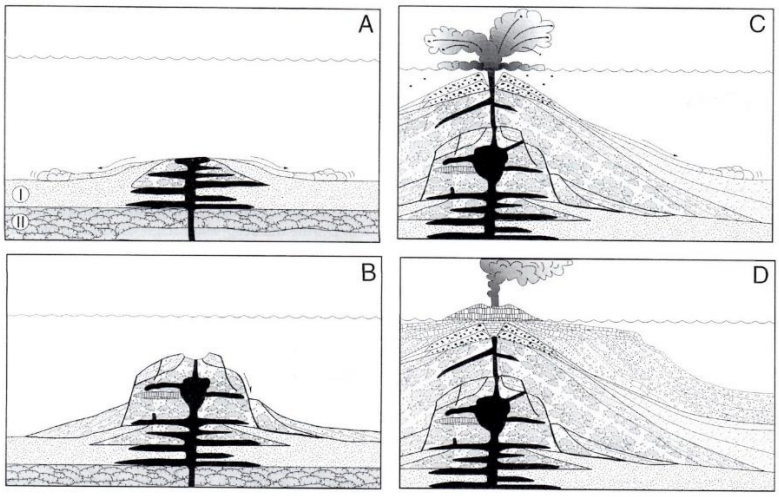

Figure 1.6 Typical growth stages of seamounts, based on La Palma (Canary island, Spain) evolution. The I and II layers are the oceanic crust sediments and the oceanic crust consisting of lava elements, respectively [Adapted from *Staudigel and Schmincke*, 1984].

1.6. The 1783 Scilla event

The Scilla (Calabria region, Italy) landslide is one of the main ground effects induced by the 1783 "Terremoto delle Calabrie" seismic sequence [*Boschi*, 2000] and represents one of the most damaging landslides in the Italian history. The earthquake sequence struck the southern part of the Calabria region between February 5th and March 28th, 1783, and was characterized by five main shocks, with a magnitude between 5.9 and 7. In Figure 1.7 the location of the main shock epicentres is shown. All these earthquakes resulted to be tsunamigenic, though the size of the generated tsunamis differed very

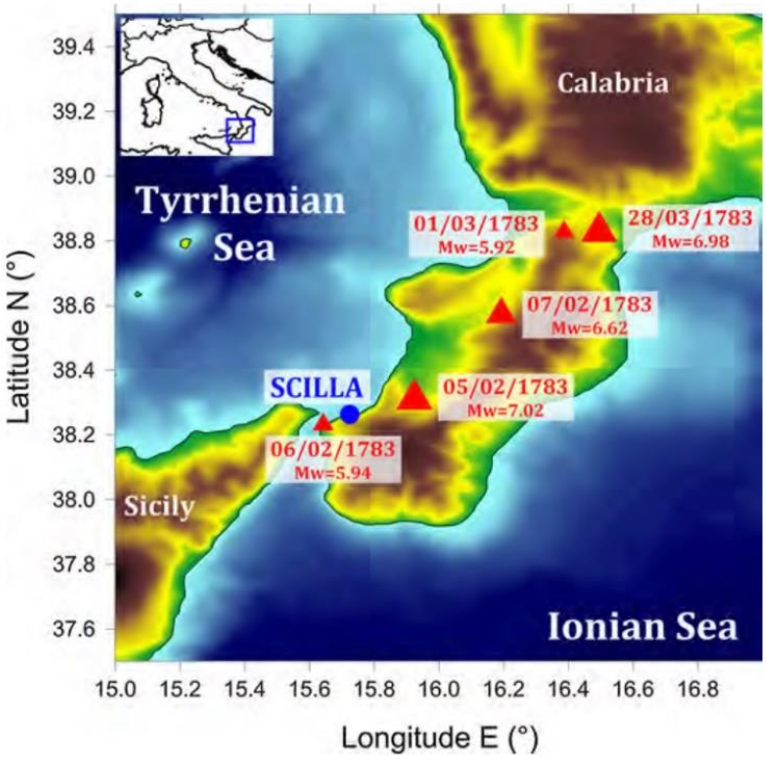

Figure 1.7 Location of the Scilla village and epicenters of the main shocks of the "Terremoto delle Calabrie" seismic sequence [Credit: *Zaniboni et al.*, 2016].

much from case to case. Furthermore, due to its relevant time scale and relatively small space scale, this series of earthquakes led to several cumulative effects, bringing great changes in the environment morphology. The Scilla slide occurred on 6th February 1783 at 1:45 a.m. in the Mt. Pacì coastal slope, located a few kilometres away from the Scilla village. The rock avalanche took place after an earthquake with an estimated magnitude of 5.8. The Mt. Pacì slope is quite steep (up to 45 degrees), and jointed gneiss rocks and breccias crop out extensively [*Mazzanti and Bozzano*, 2011; *Bozzano et al.*, 2011]. The landslide was bounded by two faults in the upper and lower part of the scar area and laterally confined (in the left part) by a major regional fault. This particular geological setting represented both a predisposing factor and a kinematic control for the 1783 event. In fact, it suggests that the rock avalanche was induced by the failure of a wedge of rock, due to the fragmentation of the jointed rock mass and to the slope morphology [*Mazzanti and Bozzano*, 2011; *Bozzano et al.*, 2011]. For this reason, we can consider this landslide as complex, in the *Varnes* [1978] classification system terminology. The subaerial volume of the displaced mass was calculated as the difference between a hypothetical pre–landslide morphology and the present one by reshaping the slope on the basis of geomorphological features and of coeval engravings by *Minasi* [see *Principe*, 1986]. Thanks to

submarine geophysical investigations [*Bosman et al.*, 2006], a large submarine depression close to the toe of the subaerial scar was recognized (Figure 1.8). Moreover, a huge depositional bulge with hummocky morphology was identified just at the toe of the submarine depression and interpreted as the landslide deposit. The maximum deposit thickness is of the order of $15\ m$. In a distance of $1.7\ km$ from the coastline, large blocks (volumes between 100 and $2 \cdot 10^5\ m^3$) randomly distributed can be found. Anyway, the landslide accumulation zone is widely spread over a relatively flat seafloor and covers an area of about $1\ km^2$. Hence, an estimated landslide volume of $9.4 \cdot 10^6\ m^3$ seems comparable with the total volume of the deposit. Analysis of the correlation between the subaerial and submarine depression could indicate that they occurred as two separate events [*Mazzanti and Bozzano*, 2011]. Furthermore, evidence from high-resolution multibeam bathymetry surveys in the underwater zone between the subaerial and the submarine scars suggested that the submarine landslide occurred before the 1783. In this work, we will consider only the 1783 subaerial landslide and its collapse into the water that led to the tsunami generation. In several studies [*Tinti and Piatanesi*, 1997; *Graziani et al.*, 2006; *Gerardi et al.*, 2008] it is shown that the 6th February tsunami at Scilla was induced by the Mt. Pacì rockslide. The time sequence of the earthquake, landslide and tsunami can be interpreted as the first clear evidence of a landslide source. As a matter of fact, according to historical reconstructions, the landslide occurred 30 minutes after the shock and the tsunami hit the close Marina Grande beach 30–60 seconds after the landslide. The rock mass fell into the sea, inducing a huge tsunami, as high as $16\ m$, that killed more than 1500 inhabitants along the Marina Grande beach [*Sarconi*, 1784; *Vivenzio*, 1788; *De Lorenzo*, 1873; *Principe*, 1986].

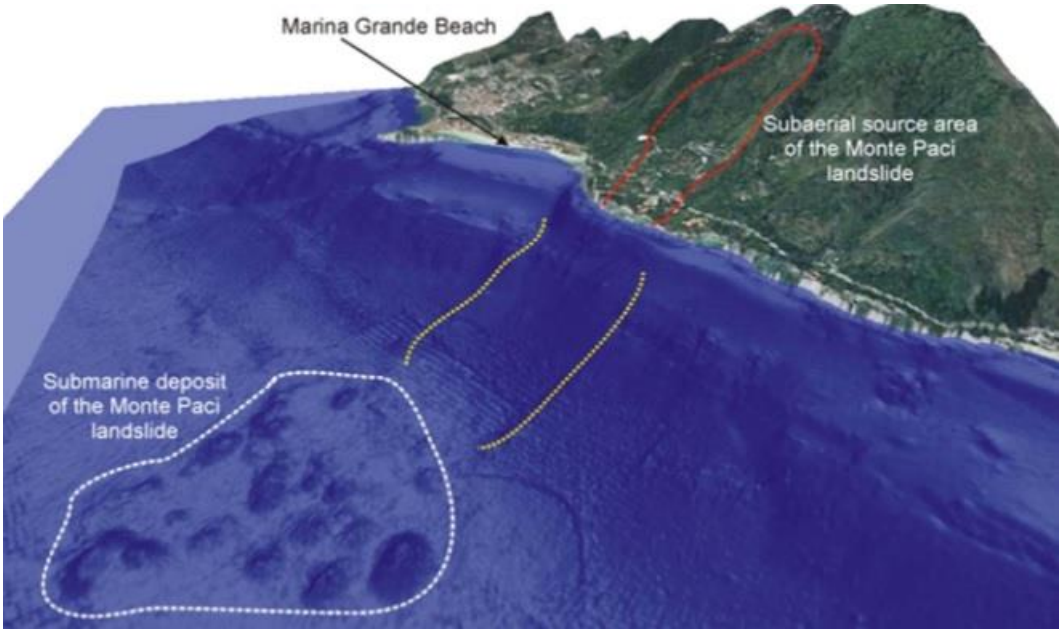

Figure 1.8 3D view of Mt. Pacì and Scilla coastal line. The dashed line bounds the 1783 landslide deposit. The red dashed line points out the subaerial landslide area. The yellow dotted lines mark the lateral boundaries of the submarine depression [Credit: *Zaniboni et al.*, 2016].

1.7. The Marsili Seamount

The Marsili Seamount (MS) is the biggest volcano structure in Europe, located in the axial portion of the Marsili Basin, in the southern part of the Tyrrhenian Sea (Figure 1.9). The basin area of $80x80$ km^2 has a maximum depth of $3700\ m$, a 5 to 12 km thick oceanic crust [*Pontevivo and Panza*, 2006] and a maximum heat flow of about $250\ mWm^{-2}$[*Zito et al*., 2003]. The MS is $70\ km$ long, $30\ km$ wide and about $3000\ m$ high, arising from the flat $-3500\ m$ sea floor to $-500\ m$ and is considered a *rift volcano.* The geological and morphological settings of the structure have been widely studied by means of different techniques [*Savelli and Schreider*, 1990; *Marani and Trua*, 2001; *Trua et al*., 2002; *Nicolosi et al*., 2006; *Cocchi et al*., 2009; *Caratori Tontini et al*., 2010; *Florio et al*., 2011; *D'Alessandro et al.*, 2012]. Overall, the MS has been studied through multibeam bathymetric surveys, magnetic and chronological evidences, seismic records and petrological analyses. Morphologically, the MS can be divided into four sectors. (1) The southern one has a pseudo-radial distribution of slopes. Its southwestern flank is characterized by a rough hummocky surface with crests and few cones. (2) In the central-southern sector, the slope increases until the top of MS. In the north, major crests and a steep scarp (slope $> 30^{\circ}$) delimit an almost flat area where cones have been detected. The eastern flank presents minor scarps parallel to the main ridge. (3) In the central-northern sector, where the summit ($-508\ m$) is located, very steep flanks (slope $> 40^{\circ}$) are evident in the upper part, while smooth slopes characterize the lower part. On the eastern flank, a clear amphitheater-shaped scarp between $-900\ m$ and $-700\ m$ is present. Below this depth, individual blocks of $250\ m$-size have been detected on the smoother slope between $-2300\ m$ and $-2400\ m$. Similarly, the western flank shows a scar and a fan-like depositional body below $-1200m$. Some cones and related flow-like morphologies characterize the top of this sector. (4) The northern section is defined by crests, shields and minor dike-like crests. These morphological zones reflect the general dynamics of the MS, generally modulated by lava flows and mass movements.

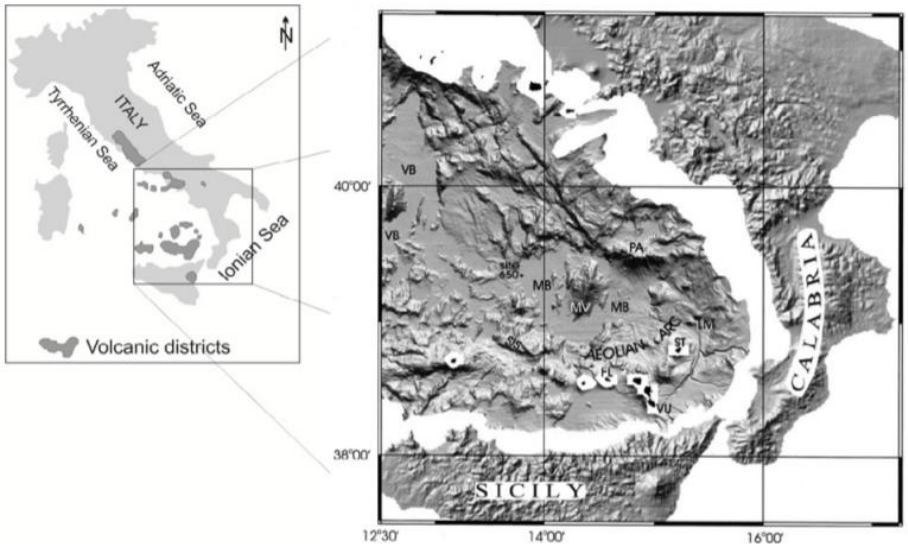

Figure 1.9 Locations of the Marsili Volcano (MV), and the Marsili Basin (MB). In the map are also shown the positions of neighbor seamounts/volcanoes. ST: Stromboli; VU: Vulcano; FL: Filicudi; SIS: Sisifo submarine Volcanoes; LM: Lametini Seamounts; PA: Palinuro Seamount; VB: Vavilov Basin [Credit: *Italiano et al.*, 2014].

Despite the numerous studies regarding the geological aspects of the volcano, the history and evolution of the MS are still debated, and a clear understanding of the past eruptions is still lacking. The MS is considered an active volcano. It was originally thought that the last eruptions occurred in geological times. The vertical accretion of the MS started at about $1\ Ma$, and continued between 0.78 and $0.1\ Ma$ in what is assumed to be the youngest MS volcanism age [*Peccerillo*, 1976; *Selli et al.*, 1977]. The data collected on the flanks and summit of the MS suggest a mainly effusive eruptive style. Nevertheless, a possible explosive activity based on two volcanoclastic levels in the Marsili Basin cannot be excluded [*Keller and Leiber*, 1974]. Furthermore, a recent study [*Iezzi et al.*, 2013] documented a submarine explosive eruption between $500\ m$ and $800\ m$ depth and revealed unexpected features of the eruptive style and volcanism age of the MS. At this stage, there is a strong need of a hazard assessment analysis, based on simulations regarding the possible eruptions and their effects. On such submarine structures, the main risk is related to possible tsunami waves originated by mass movements [e.g. *Hampton and Lee*, 1996; *Tinti et al.*, 1999, 2005; *Ward and Day*, 2005; *Shigihara et al.*, 2006; *Sassa et al.*, 2016]. In this thesis, we will show some landslide simulations over the MS flanks based on the morphological and geological settings. Past collapses of portions of the MS can be deduced from the transversal asymmetry of the volcano flanks and from the disequilibrium in the contour irregularity [*Grosse et al.*, 2009]. Another hint of possible remarkable past collapses can be found in the neighbor Vavilov volcano. This system is located about $200\ km$ northwest of the MS and was activated before the MS, but with similar evolution and rock composition. It thus represents a possible antecedent for MS future developments. Magnetic and gravity analysis have confirmed that Vavilov, just as the MS, contains low-density masses [*Morelli*, 1970]. Nowadays, the entire $40\ km$ western flank of the Vavilov appears as being completely removed in what seems a single huge collapse (volume > $50\ km^3$). It's worth pointing out that the steep gradient of approximately 18° on the eastern flank of the MS is compatible with a relevant collapse of this kind.

Chapter 2

2. An insight into landslide modelling

As was emphasised in the previous chapter, landslides are complex dynamic systems that cannot be formally described by a single kind of approach. Besides the various types of potential movements, the irregularity of the sliding surface and the difficulty of quantifying the body internal forces make the landslide modelling a hard task. For these reasons, exact analytical solutions for the equations describing the motion of a landslide are very rare and have little practical value for current applications in hazard analyses. To this goal, numerical approaches are the best option and are also helpful for a better physical understanding of such various and intricate motions.

The landslide mass is commonly portioned into a set of discrete elements whose dynamics is described at specific times. Clearly, the nature of these spatial and temporal discretizations reflect the aim of the specific model. The description of the motion is considered Eulerian when the spatial discretization is fixed in time, otherwise, when the set of elements 'follows' the slide motion, the description is said to be Lagrangian. Even if the former is the most used for the easier formulation, the latter can be useful in terms of computational effort. Landslide models are mainly divided into two categories: the ones that describe the motion of the center of mass (CoM) of the constituent elements and the ones based on the continuum mechanics approach. The first ones (e.g. lumped mass models) [*Perla et al*., 1980; *Hutchinson,* 1986] generally give a good description of the system dynamics. Originally, a single element was taken as representative of the entire landslide body. Later developments considered multi-element or multi-block representations with blocks interacting with each other while sliding [*Hungr et al*., 1995; *Tinti et al.,* 1997]. The model we present in this thesis work (called UBO-Inter) belongs to this category. In models based on the continuum mechanics description, the mass representation is related to variables that are continuous functions of space and time. Basically, each model presents specific features depending on the constitutive equations that describe the system rheology.

2.1. The continuum mechanics approach

Continuum mechanics is based on the principle that the object of study completely fills the space it occupies. In the landslides case, we are basically considering the sliding body as characterized by continuous field variables and numerical discretization is generally Eulerian. The equations of motion in a (x, y, z) Cartesian reference system are deduced from the mass and momentum conservation:

$$\begin{cases} \frac{\partial \rho}{\partial t} + \nabla \cdot (\rho\, \vec{v}) = 0 \\ \rho \left(\frac{\partial \vec{v}}{\partial t} + \vec{v} \cdot \nabla \vec{v} \right) = \rho \vec{g} + \nabla \cdot \boldsymbol{\sigma} \end{cases} \tag{2.1}$$

where $\rho(x,y,z,t)$ is the body density, $\boldsymbol{\sigma}(x,y,z,t)$ is the Cauchy stress tensor, $\vec{g}$ is the gravity acceleration and $\vec{v}(x,y,z,t)$ is the body velocity.

For landslides with fluid-like behaviour, the stress tensor can be expressed as follows:

$$\sigma_{ij} = -p\delta_{ij} + \tau_{ij}$$

where $\delta_{ij}$is the Kronecker delta, p is the pressure acting perpendicular to the fluid surface and $\boldsymbol{\tau}$ is the deviatoric stress, that basically controls the degree of body distortion. Tensile stresses are considered positive, while the compressive ones are negative. By substituting the previous condition in the equations of motion we get:

$$\begin{cases} \frac{\partial \rho}{\partial t} + \nabla \cdot (\rho\, \vec{v}) = 0 \\ \rho\left(\frac{\partial\, \vec{v}}{\partial t} + \vec{v} \cdot \nabla \vec{v}\right) = \rho \vec{g} - \nabla p + \nabla \cdot \boldsymbol{\tau} \end{cases} \tag{2.2}$$

This general set of equations can be drastically simplified under specific conditions. When the fluid is considered incompressible, i.e. when the density does not change over time, one can write:

$$\nabla \cdot \vec{v} = 0$$

Several hypotheses can be done over the stress conditions and consequently, various fluid behaviours can be described with different sets of equations, deducible from Eqs. (2.1).

In case of a *Newtonian fluid*, the deviatoric stress depends on the rate of the strain tensor e_{ij} following the relationship:

$$\tau_{ij} = -\frac{2}{3}\mu e_{kk}\delta_{ij} + 2\mu e_{ij} \tag{2.3}$$

where μ is the fluid viscosity. By substituting this last expression in Eqs. (2.2), we get the *Navier-Stokes* set of equations:

$$\begin{cases} \dfrac{\partial \rho}{\partial t} + \nabla \cdot (\rho\, \vec{v}) = 0 \\ \rho\left(\dfrac{\partial\, \vec{v}}{\partial t} + \vec{v} \cdot \nabla \vec{v}\right) = \rho \vec{g} - \nabla p + \dfrac{1}{3}\mu \nabla(\nabla \cdot \vec{v}) + \mu \nabla^2 \vec{v} \end{cases}$$

If we avoid the inviscid fluid in which the only internal force is the mean pressure acting on the fluid ($\sigma_{ij} = -p\delta_{ij}$), the law expressed in (2.3) allows us to determine a vast variety of fluids.

A more general expression for Eq. (2.3) can be written in terms of the parameter n:

$$\tau_{ij} = \mu e_{ij}^{n}$$

In the sketch of Figure 2.1, different rheologies are summarized, including also *non-Newtonian fluids* when the relationship between τ_{ij} and e_{ij} is not linear.

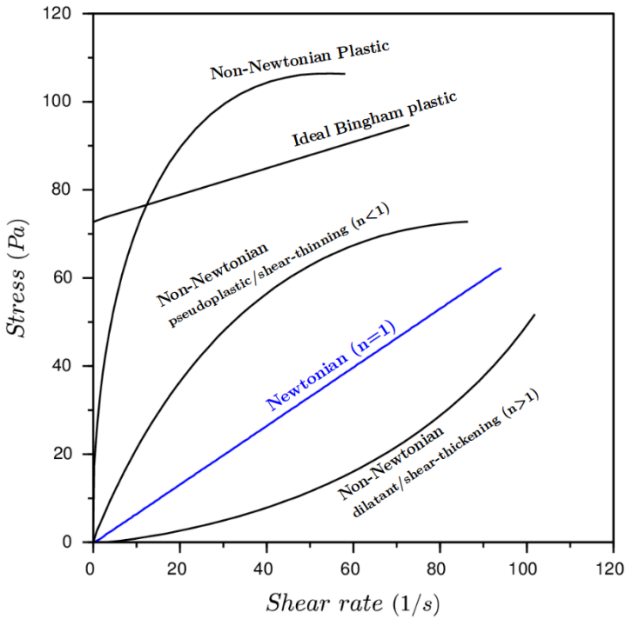

Figure 2.1 Classification of fluids based on the $\tau_{ij}\ vs.\ e_{ij}$ relationship. [Adapted from *www.simscale.com*]

Bingham fluids have been considered in some inhomogeneous or density-dependent landslide models [e.g. *Cristescu*, 2000]. An interesting approach can be found in [*Hild et al.*, 2002], where the authors describe the flow of an inhomogeneous Bingham fluid in 3D. It is worth noticing that in a Bingham viscoplastic model a rigid zone (where $e_{ij} = 0$) develops within the flow. Under peculiar circumstances, one can observe that the rigid zone growth leads to the stop of the flow, in what is called the *blocking property*. While in processes like oil drilling or metal forming this is a limitation, in the landslide case this phenomenon favours the stability of the slope. Without giving more details on the mathematical structure of the problem, the basic motion is represented in Figure 2.2, adapted from [*Hild et al.*, 2002].

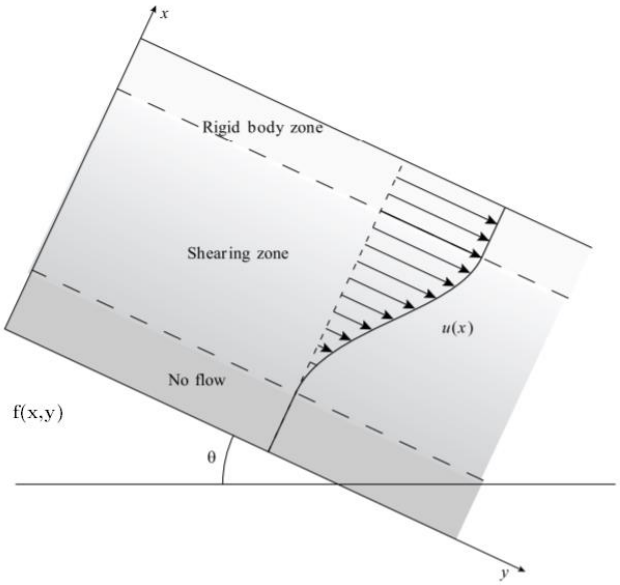

Figure 2.2 Basic landslide geometry on a slope described by an $f(x, y)$ function, based on the Bingham model [After Hild et al., *2002*].

2.2. Particle or Block models

A model based on interpreting the mass as formed by a number of individual elements (particles or blocks) was developed by [*Mc Dougall and Hungr,* 2004] to simulate the motion of rapid debris flows, avalanches or flow slides across three-dimensional terrains. The model uses an approach based on the *equivalent fluid* concept, defined for the first time by [*Hungr,* 1995]. The landslide body is considered in terms of a hypothetical material, which is ruled by a basic rheology, commonly involving a few resistance parameters that can be easily deduced by calibration. Where data are available, a calibration back-analysis is performed in terms of runout distance and velocity distribution. The resulting parameters are then considered as the apparent material parameters. This approach strongly reduces the dependence on parameters derived by laboratory experiments.

This model uses a Lagrangian approach to solve the depth-integrated Saint-Venant equations for shallow, unsteady, non-uniform, open channel flow that can be deduced from Eqs. (2.1). The depth integration is computed normally with respect to the sliding surface. The model considers the classical shallow-water assumptions:

- A small flow depth compared with the area of the landslide that varies gradually.
- Incompressibility.
- Stress-free flow surface.

As a result, the bed-normal stress is hydrostatic. Nevertheless, since the flow is moving over irregular 3D surfaces, it receives the effect of the centripetal acceleration due to the curvature of the flow path. Despite the constitutive equations, the typical Lagrangian approach involves a discretization in reference columns (or blocks), which are embedded in the flow. The local acceleration is evaluated by a numerical integration of such equations. At every time step, local velocities are hence updated, and the columns are moved to new positions. The model [*Mc Dougall and Hungr,* 2004] uses this approach and incorporates a meshless technique in which the mass conservation is satisfied by the interpolation itself, following the smoothed particle hydrodynamics method (SPH). The SPH technique was originally developed for astrophysical applications but was subsequently adapted to geophysical mass movements [e.g. *Wang and Shen,* 1999]. The SPH approach implies that the sliding mass is portioned in several elements, known as *smooth particles,* with a finite volume that remains centred in one of the moving reference columns. Since the density is constant, the flow depth of such column will be proportional to the volume of material, which is deduced by particles' proximity. Hence, by means of an interpolation, it is possible to estimate the flow depth in every reference column. The model has been tested using a closed-form solution, some controlled laboratory experiments, and one full-scale rock avalanche, with physically coherent results.

2.3. The UBO-Block models

We will now focus the attention on landslide models based on the dynamics of sliding blocks. Since the model developed in this thesis has been validated by means of a block-based model (namely UBO-Block), a clear understanding of this kind of approach is of crucial importance. To this goal let us first introduce the DAN model, developed by [*Hungr,* 1995]. It divides the sliding mass along the direction of motion in several different elements or blocks. The model considers $n-1$ constant-volume elements (mass-blocks) and n blocks with an infinitesimal ds edge (boundary blocks). The

Lagrangian 1D approach is used to solve the problem. The curvilinear reference system S is set on the sliding surface and the velocities v_i and positions s_i of the i-th boundary block are given by the simple numerical integration of the Newton law:

$$\begin{cases} v_i(t+dt) = v_i(t) + \frac{Fdt}{dm_i} \\ s_i(t+dt) = s_i(t) + \frac{dt}{2}(v_i(t+dt) + v_i(t)) \end{cases} \tag{2.4}$$

where dm_i is the infinitesimal mass of the i-th boundary block:

$$dm_i = \gamma H_i W_i ds/g$$

Here γ is the unit weight of the sliding mass, H_i and W_i are the height and width of the boundary block, respectively. To solve the iterative system (2.4) it is mandatory to evaluate the forces F acting on the system:

$$F_i = \gamma H_i W_i ds \sin\theta + P_i - T_i$$

where θ is the slope angle, P_i is the internal pressure and T_i is the basal friction. Once the s_i position has been evaluated, it is easy to compute the height h_j of the j-th mass-block with constant volume V_j, and the height H_i of the i-th boundary block:

$$\begin{cases} h_j = \frac{2V_j}{(s_{i+1}-s_i)(W_{i+1}+W_i)} \\ H_i = \frac{1}{2}(h_{j-1} + h_j) \end{cases} \tag{2.5}$$

By means of the relationships (2.4) and (2.5) the controlling variables of the system can be calculated at every time step, once the basal friction and the internal pressure are evaluated. The model can account for different fluid behaviors: plastic flow, Coulomb friction, Newtonian laminar flow, turbulent flow, Bingham flow and so on. Regarding the pressure term that acts parallel to the motion direction, it is assumed that it grows linearly with depth. The DAN model uses a simple integration method and standard fluid behaviors, but it clearly gives us an idea of the basic procedure behind a block-based model.

The UBO-Block model was developed by the Tsunami Research Team of the University of Bologna [*Tinti et al.*, 1997; *Bortolucci*, 2001] and validated in several works [e.g. *Tinti et al.*, 2002; *Zaniboni*, 2004, *Zaniboni et al.*, 2014, 2016]. The model was originally developed with a 1D description and subsequently extended to a two-dimensional system. Both versions will be used to test the UBO-Inter model in this thesis. Hence, it is crucial to understand the general assumptions of both models, that have similar structures but are based on different geometries.

The idea at the base of the UBO-Block 1D model is that the blocks forming the landslide body can interact during the motion, changing their shape, but maintaining their initial volume. We indicate with S the sliding surface and with C the landslide common CoM trajectory (see Figure 2.3). At the initial stage, the landslide has a basal surface S_0, that is a subset of S, has volume V_0 and is divided in N blocks through $N+1$ planes that cut S along the lines $D_{0,i}$ ($i = 1,2, \dots N+1$). Hence, S_0 results to be divided in N portions representing the basal surfaces of the blocks. We indicate the block positions with the curvilinear coordinates x_i, over the profile C. The CoM of the i-th block will be given by the

coordinate ξ_i, that lies between x_i and x_{i+1}. Hence, in the 1D version the position and length of the blocks, moving over the profile C, are given at any time by the coordinates x_i and ξ_i, as is shown in Figure 2.3. The profile C and the surface S must be given *a priori* to solve the landslide dynamics. This aspect is not as restricted as one could imagine. Indeed, most of the times, it is possible to estimate where and how a slide is going to move, and hence to predefine C and S, by simple geomorphological considerations.

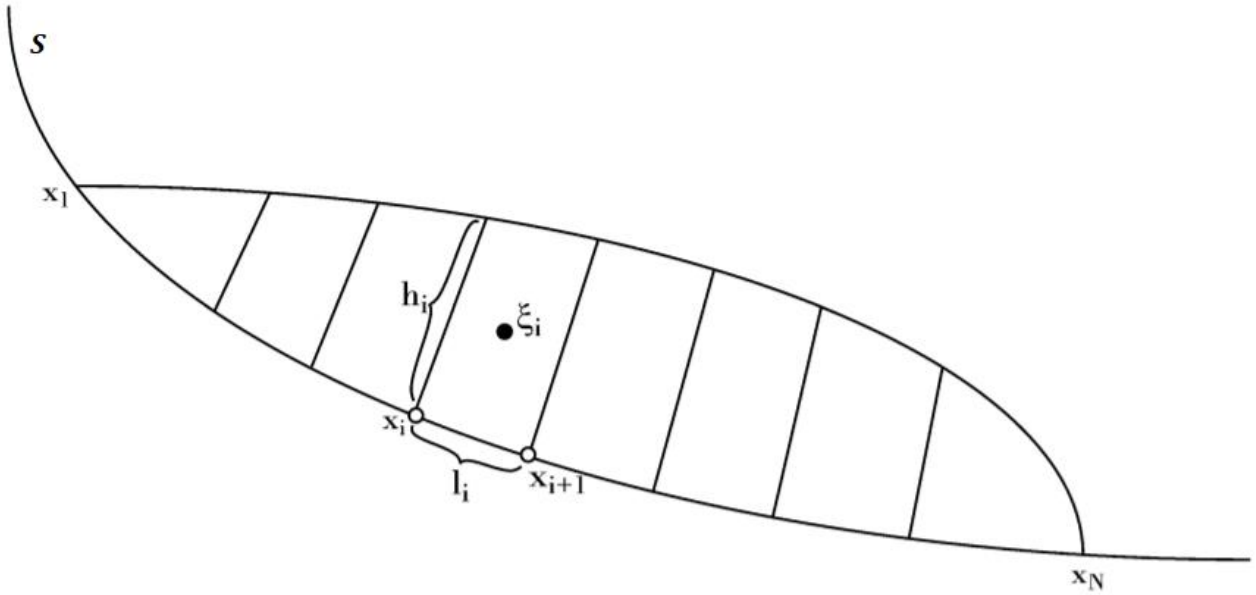

Figure 2.3 Landslide subdivision in a chain of blocks, over the sliding surface S. x_1 and x_N represent the body extremes up-hill and down-hill. ξ_i represents the CoM of the i-th block, with length l_i and height h_i.

The general dynamics at every time step is written in terms of selected geometrical and kinematic variables of the blocks: CoM position $\xi_i(t)$, velocity $v_i(t)$, acceleration $a_i(t)$, volume V_i, length along the profile $l_i(t)$, bottom surface $A_i(t)$, height $h_i(t)$ and width $w_i(t)$. By simple geometrical considerations, we can write:

$$\begin{cases} l_i = x_{i+1} - x_i \\ A_i = A(x_{i+1}) - A(x_i) \\ h_i = V_i/A_i \\ w_i = A_i/l_i \end{cases} \tag{2.6}$$

If we denote with i and k the indices of the spatial and temporal discretization, the acceleration of each block can be written as:

$$a_{ik} = G_{ik} - R_{ik} + F_{ik} \tag{2.7}$$

where G, R, F are the gravity, resistance and internal interaction terms, respectively. The gravity term is given by:

$$G_{ik} = \nu g[\sin\theta_{ik} - \mu(\cos\theta_{ik} + \tfrac{a_{c,ik}}{g})\,] \tag{2.8}$$

where g is the gravity acceleration, θ_{ik} is the local slope angle and $a_{c,ik}$ is the centripetal acceleration, μ is the basal friction coefficient and ν is a dimensionless coefficient that estimates the density reduction due to the buoyancy force acting on the mass in subaqueous motions. The resistance term R is given by the interaction of the sliding mass with the surrounding fluid. This term mainly depends

on the square of the sliding mass velocity. Since blocks interact with water through the front and top surfaces, these forces will be given by the sum of two different terms, the front drag however being usually more efficient than the tangential resistance:

$$R_{ik} = \frac{1}{2}\frac{\rho' C_t}{\rho h_{ik}} v_{ik}^2 + \frac{1}{2}\frac{\rho'}{\rho} C_d \frac{\Delta h_{ik} w_{ik}}{V_i} \; v_{i,k}'^2 \tag{2.9}$$

Here $\Delta h_{ik} = h_{i,k} - h_{i+1,k}$, C_d and C_t are the drag and top resistance coefficients, $v'_{i,k}$ is the velocity of the i-th block in the sliding direction and ρ' is the water density. Further, V_i is the volume of the i-th block, that is independent from the time. Finally, let us consider the interaction term F that needs some additional considerations. It is assumed that the interaction between blocks preserves the momentum and does not change the block mass. Furthermore, despite the temporal continuity of the whole process, internal interactions are assumed to take place as instantaneous processes occurring only at the end of each time step. By denoting with u_{ik} the block velocity before the interaction, we can write:

$$\begin{cases} \sum_{i=1}^{N} m_i v_{ik} = \sum_{i=1}^{N} m_i u_{ik} \\ v_{i+1,k} - v_{i,k} = e_{i,k}(u_{i+1,k} - u_{i,k}) \end{cases} \tag{2.10}$$

The first equation in (2.10) represents the momentum conservation, while the second one provides the kinetic energy variation of two neighbour blocks, calibrated through an interaction coefficient $e_{i,k}$. This latter coefficient basically represents the true nature of the interaction and takes all the values between 0 and 1. If $e_{i,k} = 1$ there is no interaction and blocks preserve their original velocity, while if $e_{i,k} = 0$ the interacting blocks gain the same velocity and basically become one single block after the interaction. The system (2.10) can be solved through an iterative process and the internal acceleration is finally given by:

$$F_{ik} = \frac{v_{ik} - u_{ik}}{dt} \tag{2.11}$$

Let us now focus on the coefficient $e_{i,k}$. Since, as will be seen later, the UBO-Inter model is based on the dynamics of the internal forces, it is important to describe in detail how UBO-Block estimates this aspect, in order to get a clear understanding of the differences between the two models. Basically, the coefficients $e_{i,k}$ tell us how the total mass behaves in terms of blocks interactions. If, for instance, $e_{i,k} = 0$, then all blocks move with the same velocity and keep the reciprocal distances fixed in time. The result is that, in this case, UBO-Block describes the behaviour of a semi-rigid body. In the opposite scenario, i.e. if $e_{i,k} = 1$, the blocks are free to move over the surface as they were alone. Some limitations must be posed over $e_{i,k}$ to avoid physically inconsistent behaviours. More specifically, if a block moves freely, it could *cross* another block, which however cannot occur. To avoid such occurrence, it is imposed that the reciprocal distances cannot exceed specific limits. Hence, $e_{i,k}$ is defined as:

$$\begin{cases} e_{ik} = f_{ik}\left(1 - \frac{1}{\sigma}\left|1 - \frac{\Delta\xi_{ik}}{\Delta\xi_{i,k-1}}\right|\right)^{\gamma_r} & if \quad \Delta\xi_{ik} \in I_{i,k}, \;\; r = 1,2 \\ e_{ik} = 0 & if \quad \Delta\xi_{ik} \notin I_{i,k} \end{cases} \tag{2.12}$$

where $\Delta\xi_{ik} = \xi_{i+1,k} - \xi_{i,k}$ and the function f_{ik} is given by:

$$\begin{cases} f_{ik} = \lambda & if \quad \Delta\xi_{ik} \geq \Delta\xi_{i,0} \\ f_{ik} = \lambda\left[1 - \frac{1}{\sigma_0}\left(1 - \frac{\Delta\xi_{ik}}{\Delta\xi_{i,0}}\right)\right] & if\ (1-\sigma_0)\Delta\xi_{i,0} < \Delta\xi_{ik} < \Delta\xi_{i,0} \\ f_{ik} = 0 & if\ \Delta\xi_{ik} \leq (1-\sigma_0)\Delta\xi_{i,0} \end{cases} \tag{2.13}$$

Hence, the f_{ik} function allows the block reciprocal distances to slightly change from the original value $\Delta\xi_{i,0}$ within a specific interval $I_{i,k}$. The amplitude of the interval depends on the σ parameter ($\sigma \in [0,1]$) that governs the system deformability:

$$I_{i,k} = |(1-\sigma)\Delta\xi_{i,k}\,, (1+\sigma)\Delta\xi_{i,k}|$$

Moreover, the value of λ represents the maximum value that the interaction coefficient can reach. When $\lambda \neq 0$ the values of $e_{i,k}$ are controlled by the $\gamma > 0$ shape parameter. Two specific values $\gamma_1$and γ_2 reflects expansion and compression status of the mass. The relationship between $e_{i,k}$ and γ are shown in Figure 2.4, for selected values of σ and λ. In the following chapter, we will show that this basic idea is partially reproduced also in the UBO-Inter model.

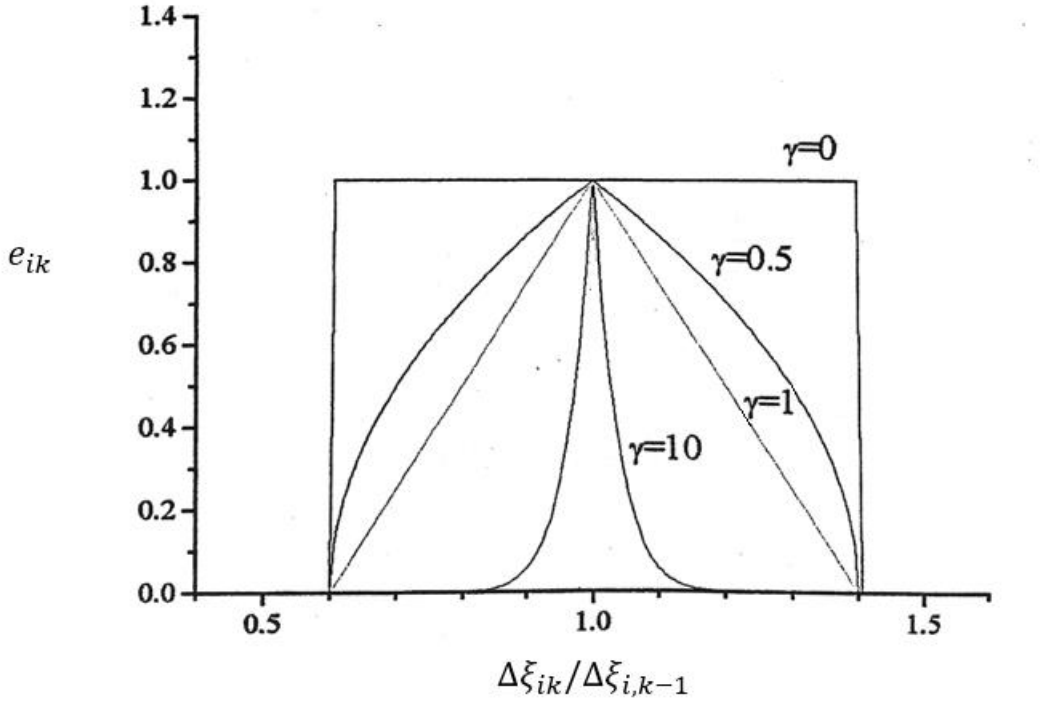

Figure 2.4 Relationship between e_{ik} and$\frac{\Delta\xi_{ik}}{\Delta\xi_{i,k-1}}$ for selected values of γ. Credit: [*Bortolucci*, 2001].

Once the dynamics is solved, we can numerically integrate the equations of motion to get positions and velocities of each block at every discrete time $t_k = (k-1)dt$. The explicit integration approach assumes that all the geometrical and physical variables at the time t_{k-1} are known when one computes them at the time t_k. By using Eq. (2.7) we can easily get the blocks CoM velocity as:

$$u_{ik} = v_{i,k-1} + \left(G_{i,k-1} - R_{i,k-1}\right)dt \tag{2.14}$$

By means of the Eqs. (2.10), we can get the CoM velocities after the interaction process and evaluate the velocities of the blocks' edges. To this purpose, it is supposed that the velocity of the i-edge is directly proportional to the relative position with respect to the CoM of the i and $i-1$ block at the

previous time step. Once the edge velocities are known, edge positions are easy to evaluate by a further numerical integration. Finally, the CoM positions are evaluated from these values. The temporal cycle is stopped if the block velocities are close to zero, or if the landslide runs beyond the boundary of the sliding surface S. Some modifications on this approach must be made when a changing time step is chosen, but the algorithm structure is not modified.

We have chosen to give the details of the procedure of the 1D model because its formal description is easier than the two-dimensional one, which allows the reader to get a clear understanding of the basic physical concepts used to simulate the slide motion. Furthermore, all the involved vector variables with the exception of the centripetal accelerations are tangential to the prescribed trajectory C, reducing the relationships to a scalar representation. Instead, in the 2D description, the controlling variables must be introduced as space vectors and the generic CoM trajectories are unknown (hence must be calculated dynamically). Given the sliding surface $S^* \in R^3$, the only constraint applied is that the CoM trajectories are bound to lie over this surface. Another different aspect is the landslide body representation. In the 1D case, the subdivision in blocks is done on the curve C, forming a chain of elements. In the 2D version, the sliding area is divided in quadrangles (regular or irregular) and the blocks are built considering the local height of the sliding body. The generalization to the 2D description will not be given in detail here and we refer the interested reader to [*Bortolucci*, 2001] for the full illustration of the procedure.

Chapter 3

3. The motion of a rigid body

3.1. The basic idea

The basic idea behind the UBO-Inter numerical model is to describe the motion of several particles or point-masses that can slide over a surface and interact with each other. As we have seen in the previous chapter, there are different ways in which we can introduce an interaction between sliding bodies, that is basically related to the kind of behaviour we want to simulate. Here we focus on rockslides and we use a semi-rigid-body approach. With this, we mean that we consider rockslides that can change shape during motion but where the change of volume can be neglected. Indeed, it is known that rocks can deform under the effect of high pressure or high temperature [e.g. *Paterson and Wong*, 2005]. But this kind of deformation plays no, or a minor, role during the motion of a rockslide. Nevertheless, we cannot avoid the fact that different parts of rocks interact with each other while sliding down. Such strong interactions are fundamental and can strongly influence the general motion. So, even if single rock elements are *de facto* a rigid body, the whole landslide body is not, but can be considered as an ensemble of rock pieces or blocks moving together: this may account for possible differential movements across bedding planes, faults, joints, and fissures, and for possible rock breaking down, rock fragmentation, etc. This complex behaviour in a rock slide is the key aspect we want to focus on in this thesis work: finding a way to describe the motion of single bodies that as a whole form a semi-rigid body. As the words suggest, this latter behaviour is located half-way between a purely rigid and a deformable body. So, the general structure of our model is based on rigid-body conditions, that can be released under specific circumstances. This crucial transition must be well defined to avoid unrealistic descriptions, as we will show later on. In order to formally describe this kind of motion, we will follow a step-by-step procedure, starting from the motion of few point-masses. In what follows, we will show this process in detail, with simple-geometry examples that are essential to understand the final semi-rigid body description. More considerations and simplifications will be done on the general motion, but the main aspect we need to focus on is this semi-rigid body approach. Pointedly, the way we introduce the rigid body conditions is totally brand new and it could lead to interesting developments also in other fields. We consider the rockslide as formed by a set of point masses. In the approach described in this chapter, the basic idea is to keep the point masses adherent to the sliding surface and to conserve the reciprocal 3D distance during the motion. Thus, even if we will use the term ‘rigid body’, we formally describe the motion of point masses that move on a surface and that altogether represent a rockslide that adapts its form to the shape of the surface it slides on. The fixed 3D-distance condition is obtained through the introduction of an interaction force. This latter is calculated through a constraint on the particle’s accelerations. Incidentally, we observe that the point-mass distances are considered in the 3D space and they are not geodetic lines over the sliding surface. This is a crucial aspect of the model where a physical characteristic is described through a geometrical constraint. Nevertheless, we will show that this assumption alone is

not sufficient to fully describe a rockslide motion but must be complemented by other considerations that will be addressed in the following chapter.

3.2. The rigid triangle model

Let us introduce the basic features of the model by means of a simple structure formed by three point masses P_i with $i = 1,2,3$. For the sake of completeness, the dynamics of a two-mass system is also presented and discussed in detail in Appendix B. We want to describe the motion of a rigid-body sliding down a generic analytical surface described by the function $z = f(x, y)$, in a Cartesian reference system. These point masses may be interpreted as representative of the CoM of three hypothetical blocks forming the rockslide. These masses are adherent to the surface and can interact with each other by means of internal interaction forces $\vec{h}$ that keep each pair of point masses at the same initial 3D distance. None of these forces perform work on the system and, as we will show later, are evaluated dynamically *while* solving the equations of motion. Furthermore, the assumption of the masses adhering to the surface allows us to describe the motion in two dimensions. For the sake of clarity, we will write the equations in vector formalism. Further, all the forces are written in terms of the surface derivatives f_i. More details can be found also in the Appendix A, where the equations for a single point mass are formally derived.

The points have coordinates $\vec{r}_1, \vec{r}_2, \vec{r}_3$ with $\vec{r}_i = (\vec{x}_i, z_i)$ $i = 1,2,3$. Here $\vec{x}_i$ is a horizontal vector and z_i the vertical coordinate. The general motion is mainly driven by gravity. The other external forces acting on the system are the reaction force of the surface and the basal friction, ruled by the friction coefficient μ. By denoting with $\vec{r}_{ij} = (\vec{r}_i - \vec{r}_j)/|\vec{r}_i - \vec{r}_j|$ the unit vector along the joining line between P_i and P_j $(i, j = 1,2,3)$ we can write for the interaction force:

$$\vec{h}_{ij} = h_i \vec{r}_{ij} \qquad \vec{h}_{ji} = -\vec{h}_{ij}$$

In other words, the interaction force exerted by the i-th mass on the j-th one is equal and opposite to the one exerted by the j-th mass on the i-th one. Since we want that these forces keep the masses at the same 3D distance, it is natural that $\vec{h}_{ij}$ is introduced as a force acting on the $\vec{r}_{ij}$ direction, as is shown in the sketch of Figure 3.1. Furthermore, since the masses move on the surface, the interaction force induces an associated reaction exerted by the sliding surface. Hence, if one takes also into account the bottom friction, the total force exerted on the mass P_i due to the interaction with the mass P_j can be written as:

$$\vec{H}_{ij} = \pm h_i \vec{r}_{ij} \mp \left(h_i \vec{r}_{ij} \circ \vec{n}_i\right)\left(\vec{n}_i - \mu \vec{t}_i\right)$$

where $\vec{n}_i$ is the unit vector normal to the surface in the point P_i and pointing upwards, and the symbol $\circ$ denotes the inner product (see Appendix B). In the following we assume $i < j$ and set the sign of

h_i consistently: if the force is applied to the i-th particle, the force is $h_i\vec{r}_{ij}$, while if it is applied to the j-th particle, the force is written as $-h_i\vec{r}_{ij}$.

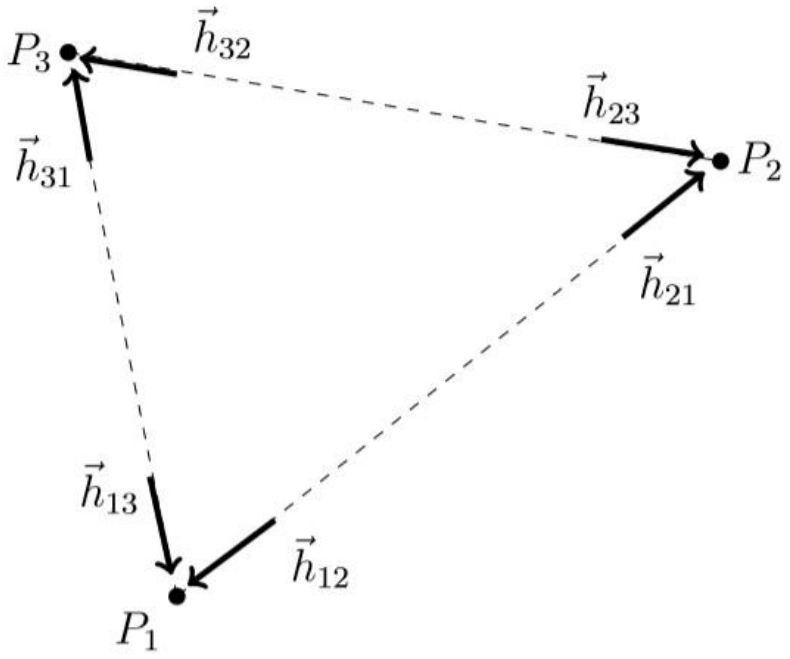

Figure 3.1 Basic geometry of the three-mass structure. The positions are given by the coordinates: $P_1 = \left(\vec{x}_1, f(\vec{x}_1)\right)$; $P_2 = \left(\vec{x}_2, f(\vec{x}_2)\right)$; $P_3 = \left(\vec{x}_3, f(\vec{x}_3)\right)$. The interaction forces lie on the line joining the masses.

Bearing in mind the previous considerations, the equations of motion for the three point masses can be written as:

$$
\begin{aligned}
m_1\ddot{\vec{r}}_1 &= \vec{F}_1 + h_1\vec{r}_{12} - (h_1\vec{r}_{12}\circ\vec{n}_1)\left(\vec{n}_1 - \mu\vec{t}_1\right) + h_3\vec{r}_{13} - (h_3\vec{r}_{13}\circ\vec{n}_1)\left(\vec{n}_1 - \mu\vec{t}_1\right)\\
m_2\ddot{\vec{r}}_2 &= \vec{F}_2 - h_1\vec{r}_{12} + (h_1\vec{r}_{12}\circ\vec{n}_2)\left(\vec{n}_2 - \mu\vec{t}_2\right) + h_2\vec{r}_{23} - (h_2\vec{r}_{23}\circ\vec{n}_2)\left(\vec{n}_2 - \mu\vec{t}_2\right)\\
m_3\ddot{\vec{r}}_3 &= \vec{F}_3 - h_2\vec{r}_{23} + (h_2\vec{r}_{23}\circ\vec{n}_3)\left(\vec{n}_3 - \mu\vec{t}_3\right) - h_3\vec{r}_{13} + (h_3\vec{r}_{13}\circ\vec{n}_3)\left(\vec{n}_3 - \mu\vec{t}_3\right)
\end{aligned}
\tag{3.1}
$$

Here m_i is the i-th mass; $\ddot{\vec{r}}_i$ is its acceleration; and $\vec{F}_i$ are the other forces acting on the system. In detail, they can be expressed as:

$$
\begin{aligned}
\vec{F}_1 &= m_1\vec{g} + m_1(\ddot{\vec{r}}_1 - \vec{g})\circ\vec{n}_1\left(\vec{n}_1 - \mu\vec{t}_1\right)\\
\vec{F}_2 &= m_2\vec{g} + m_2(\ddot{\vec{r}}_2 - \vec{g})\circ\vec{n}_2\left(\vec{n}_2 - \mu\vec{t}_2\right)\\
\vec{F}_3 &= m_3\vec{g} + m_3(\ddot{\vec{r}}_3 - \vec{g})\circ\vec{n}_3\left(\vec{n}_3 - \mu\vec{t}_3\right)
\end{aligned}
\tag{3.2}
$$

In the above eqautions, $\vec{g} = -g\vec{k}$ is the gravity acceleration vector ($\vec{k}$ is the unit vertical vector pointing upwards); μ is the basal friction coefficient and $\vec{t}_i = \dot{\vec{r}}_i/\left|\dot{\vec{r}}_i\right|$ is the unit vector parallel to the instantaneous velocity of the i-th mass, and therefore tangential to the surface. As we can see, the

friction force depends also on the interaction force terms. This is a relevant aspect of this force: we are basically introducing an internal force that is related to the general dynamics. We must also point out that in the point P_i, the centripetal acceleration can be written in terms of the mass velocity $\dot{\vec{r}}_i$ and of the radius of curvature R_i (for the extended formulation, see appendix A), that is:

$$\ddot{\vec{r}}_i \circ \vec{n}_i = (\dot{\vec{r}}_i \circ \dot{\vec{r}}_i)/R_i$$

The system of Eqs. (3.1) is a set of Ordinary Differential Equations (ODE), that cannot be solved without further considerations since the number of unknowns (mass positions $\vec{r}_i$ and internal forces h_i) is greater than the number of equations. To this goal, we use the fixed-distance conditions to evaluate the interaction forces *before* we actually solve the system (3.1). We impose that the Euclidian distance between any two point masses in the space is constant, i.e.:

$$d_{ij}^2 = (\vec{r}_i - \vec{r}_j) \circ (\vec{r}_i - \vec{r}_j) = (\vec{x}_i - \vec{x}_j) \circ (\vec{x}_i - \vec{x}_j) + (z_i - z_j)^2 = const. \qquad (3.3)$$

We will use this constraint in terms of mass accelerations, that can be easily evaluated from Eqs. (3.1). To this purpose, we derive Eq. (3.3) twice with respect to the time and get:

$$(\ddot{\vec{r}}_i - \ddot{\vec{r}}_j) \circ (\vec{r}_i - \vec{r}_j) = -(\dot{\vec{r}}_i - \dot{\vec{r}}_j) \circ (\dot{\vec{r}}_i - \dot{\vec{r}}_j) \qquad (3.4)$$

By substituting the acceleration $\ddot{\vec{r}}_i$ from Eqs. (3.1) into (3.4) we get three different expressions, one for each fixed edge of the triangle. For the edge connecting the masses P_1 and P_2, we get:

$$(\ddot{\vec{r}}_1 - \vec{g}) \circ \vec{n}_1(\vec{n}_1 - \mu\vec{t}_1) \circ \vec{r}_{12} - (\ddot{\vec{r}}_2 - \vec{g}) \circ \vec{n}_2(\vec{n}_2 - \mu\vec{t}_2) \circ \vec{r}_{12} -$$
$$-h_1[\frac{1}{m_1}(\vec{r}_{12} \circ \vec{n}_1)(\vec{n}_1 - \mu\vec{t}_1) \circ \vec{r}_{12} + \frac{1}{m_2}(\vec{r}_{12} \circ \vec{n}_2)(\vec{n}_2 - \mu\vec{t}_2) \circ \vec{r}_{12} - (\vec{r}_{12} \circ \vec{r}_{12})(\frac{1}{m_1} + \frac{1}{m_2})] +$$
$$+h_2[\frac{1}{m_2}(\vec{r}_{23} \circ \vec{n}_2)(\vec{n}_2 - \mu\vec{t}_2) \circ \vec{r}_{12} - \frac{1}{m_2}(\vec{r}_{23} \circ \vec{r}_{12})] +$$
$$-h_3[\frac{1}{m_1}(\vec{r}_{13} \circ \vec{n}_1)(\vec{n}_1 - \mu\vec{t}_1) \circ \vec{r}_{12} - \frac{1}{m_1}(\vec{r}_{13} \circ \vec{r}_{12})] = -(\dot{\vec{r}}_1 - \dot{\vec{r}}_2) \circ (\dot{\vec{r}}_1 - \dot{\vec{r}}_2)$$

In an analogous way, from the constraint along the connection between masses P_1 and P_3, we obtain:

$$(\ddot{\vec{r}}_1 - \vec{g}) \circ \vec{n}_1(\vec{n}_1 - \mu\vec{t}_1) \circ \vec{r}_{13} - (\ddot{\vec{r}}_3 - \vec{g}) \circ \vec{n}_3(\vec{n}_3 - \mu\vec{t}_3) \circ \vec{r}_{13} -$$
$$-h_1[\frac{1}{m_1}(\vec{r}_{12} \circ \vec{n}_1)(\vec{n}_1 - \mu\vec{t}_1) \circ \vec{r}_{13} + \frac{1}{m_1}(\vec{r}_{12} \circ \vec{r}_{13})] -$$

$$-h_2[\frac{1}{m_3}(\vec{r}_{23}\circ\vec{n}_3)\left(\vec{n}_3-\mu\vec{t}_3\right)\circ\vec{r}_{13}-\frac{1}{m_3}(\vec{r}_{23}\circ\vec{r}_{13})]+$$

$$-h_3[\frac{1}{m_1}\quad(\vec{r}_{13}\circ\vec{n}_1)\left(\vec{n}_1-\mu\vec{t}_1\right)\circ\vec{r}_{13}+\frac{1}{m_1}(\vec{r}_{13}\circ\vec{n}_3)\left(\vec{n}_3-\mu\vec{t}_3\right)\circ\vec{r}_{13}-(\vec{r}_{13}\circ\vec{r}_{13})(\frac{1}{m_1}+\frac{1}{m_3})]=$$
$$-\left(\dot{\vec{r}}_1-\dot{\vec{r}}_3\right)\circ\left(\dot{\vec{r}}_1-\dot{\vec{r}}_3\right)$$

Finally, for the interaction between masses P_2 and P_3, we get

$$(\ddot{\vec{r}}_2-\vec{g})\circ\vec{n}_2\left(\vec{n}_2-\mu\vec{t}_2\right)\circ\vec{r}_{23}-(\ddot{\vec{r}}_3-\vec{g})\circ\vec{n}_3\left(\vec{n}_3-\mu\vec{t}_3\right)\circ\vec{r}_{23}+$$

$$+h_1[\frac{1}{m_2}\ (\vec{r}_{12}\circ\vec{n}_2)\left(\vec{n}_2-\mu\vec{t}_2\right)\circ\vec{r}_{23}-\frac{1}{m_2}(\vec{r}_{12}\circ\vec{r}_{23})]-$$

$$-h_2[\frac{1}{m_2}\ (\vec{r}_{23}\circ\vec{n}_2)\left(\vec{n}_2-\mu\vec{t}_2\right)\circ\vec{r}_{23}+\frac{1}{m_3}(\vec{r}_{23}\circ\vec{n}_3)\left(\vec{n}_3-\mu\vec{t}_3\right)\circ\vec{r}_{23}-(\vec{r}_{23}\circ\vec{r}_{23})(\frac{1}{m_2}+\frac{1}{m_3})]-$$

$$-h_3[\frac{1}{m_3}(\vec{r}_{13}\circ\vec{n}_3)\left(\vec{n}_3-\mu\vec{t}_3\right)\circ\vec{r}_{23}-\frac{1}{m_3}(\vec{r}_{13}\circ\vec{r}_{23})]=\ -\left(\dot{\vec{r}}_2-\dot{\vec{r}}_3\right)\circ\left(\dot{\vec{r}}_2-\dot{\vec{r}}_3\right)$$

These three linear relationships can be written in the compact form:

$$\boldsymbol{\theta h}=\boldsymbol{a}$$

where $\boldsymbol{\theta}$ is the matrix of the coefficients, given by the terms in the squared brackets in the previous equations; $\boldsymbol{h}^T=[h_1,h_2,h_3]$ is the unknown vector of the magnitude of the interaction forces and $\boldsymbol{a}$ is the vector containing all the velocity- and position-dependent terms. Finally, the interaction forces can be evaluated by inverting the matrix $\boldsymbol{\theta}$:

$$\boldsymbol{h}=\boldsymbol{\theta}^{-1}\boldsymbol{a}$$

Once all the h_i, and consequently all the $\vec{h}_{ij}$ forces are calculated, the system of Eqs. (3.1) can be solved by means of numerical methods. In this study, we will solve all the equations of motion by means of the fourth-order Runge-Kutta numerical scheme, computed through MATLAB codes. For the sake of clarity, the Runge-Kutta discretization scheme is shown explicitly for the coupled masses case in Appendix C. The method uses a series of intermediate steps at each time step to compute temporary variables. As the number of point-masses and hence of equations of motion increases, the number of constraints on h_i increases even more quickly, and the above linear system becomes overdetermined. This aspect will be discussed carefully later on.

3.2.1. The rigid triangle examples

In this section, we will present some simple examples for the three-mass structure. The simple basic geometry allows us to have a clear understanding of the specific dynamics described by Eqs. (3.1). In structures formed by a larger number of masses, the dynamics of the internal forces can be quite intricate. Although even the two-mass case can be somehow helpful to understand the behavior of the

$\vec{h}_{ij}$ force, we believe that the three-mass structure is more appropriate to introduce the further generalization to a larger number of point masses.

Let us consider an elliptic paraboloid in a (x, y, z) Cartesian reference system, described by the function:

$$z = ax^2 + by^2$$

with $a = 2 \cdot 10^{-5}\, m^{-1}, b = 4 \cdot 10^{-5}\, m^{-1}$. This sliding surface is built over a $(4x4)\, km^2$ area centered in the system origin. In the next three examples, we will illustrate the motion of the same triangle-shaped structure sliding on the above surface with different sets of parameters. The simulation time, the mass values, and the basal friction coefficient are given in Table 3.1. In all simulations, the triangle area is $S = 1750\, m^2$ and its centroid is initially set in $P_c = (-1080;\ +1370;\ +100)\, m$. The equations of motion are numerically solved with the time step $dt = 0.1\, s$.

Cases	Simulation time $t\ (s)$	$m_1(kg)$	$m_2(kg)$	$m_3(kg)$	Friction coefficient μ
A1	300	100	100	100	0
B1	300	1	1000	1	0
C1	300	100	100	100	0.02

Table 3.1 Main parameters for simulations A1-C1.

For the sake of clarity, in the following figures where the results of the simulations are given we use colours to distinguish masses and to distinguish curves. We use red, green and blue for the first, second and third mass, and Table 3.2 helps the reader to associate the interaction force h_i with the respective mass pair as depicted in Figure 3.2. Furthermore, the association between the colour of the curves and the interaction forces, velocities and distances are given in Table 3.3.

Interaction forces	h_1	h_2	h_3
Involved masses	m_1*(Red)-* m_2*(Green)*	m_1*(Red)-*m_3*(Blue)*	m_2*(Green)-*m_3*(Blue)*

Table 3.2 Association of the interaction forces with the mass colours for simulations A1-C1.

Curve colour	*Blue*	*Red*	*Yellow*
Interaction forces	h_1	h_2	h_3
Velocities	v_1	v_2	v_3
Distances	$\lvert\vec{r}_{12}\rvert$	$\lvert\vec{r}_{13}\rvert$	$\lvert\vec{r}_{23}\rvert$

Table 3.3 Association between curve colours and problem variables used in Figures 3.3.

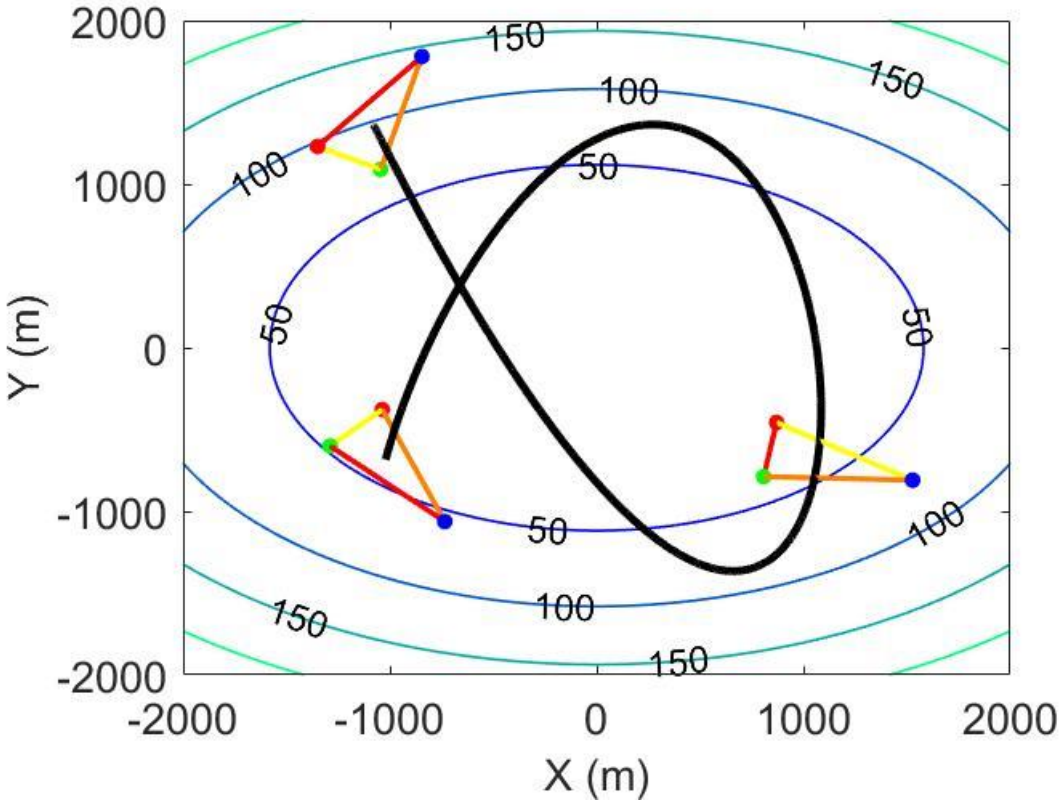

Figure 3.2 CoM trajectory (black line) for case A1 involving three equal masses sliding on the elliptic paraboloid portrayed through contour lines. The red, green and blue solid circles represent the first, second and third mass (see Table 3.2). The initial position of the system is on the left top. Mass positions are given in three instants, i.e. at $t = [0;\ 150;\ 300]$s. The magnitude of the interaction forces is ranked by colours from the largest (red) to the medium (orange) and the smallest one (yellow).

Case A1 represents a frictionless rigid-body motion. The masses are all equal and the CoM of the system coincides with the triangle's centroid. The triangle system, starting from a zero-velocity initial state, slides over the ellipsoid slopes reaching peak velocities in the order of $42\frac{m}{s}$ (upper left panel in Figure 3.3), showing an oscillatory behavior. Masses slide down the paraboloid and tend to rotate around the CoM. The 3D distances are very well preserved during the motion (upper right panel in Figure 3.3) and the absence of dissipative forces ensures the system energy conservation (bottom left panel in Figure 3.3). The time histories of the interaction forces, shown in the bottom right panel of Figure 3.3, present oscillations depending on mass positions and velocities. They are always positive, which means repulsive. As we can see, in the initial position h_2 is by far the strongest force since the red and blue masses tend to accelerate faster over the slope due to their higher positions. Initially, the effective gravity force acts differently on the masses and, as long as they do not reach high velocities, the only force to be balanced by the interaction forces is gravity. Conversely, during the motion, the situation is more intricate, since the masses gain velocities and also the centripetal forces must be balanced. Around 150 s, all interaction forces are small, and the largest one is h_1. Later, the predominant interaction force is h_3 attaining nearly the same value initially possessed by h_2. So we see that internal forces alternate. Basically, the interaction forces keep the system *compact* during the motion. Indeed, such forces, that reach only ≈ 2 % of the mean gravity force acting on the system in our example, hold the masses together as we do expect.

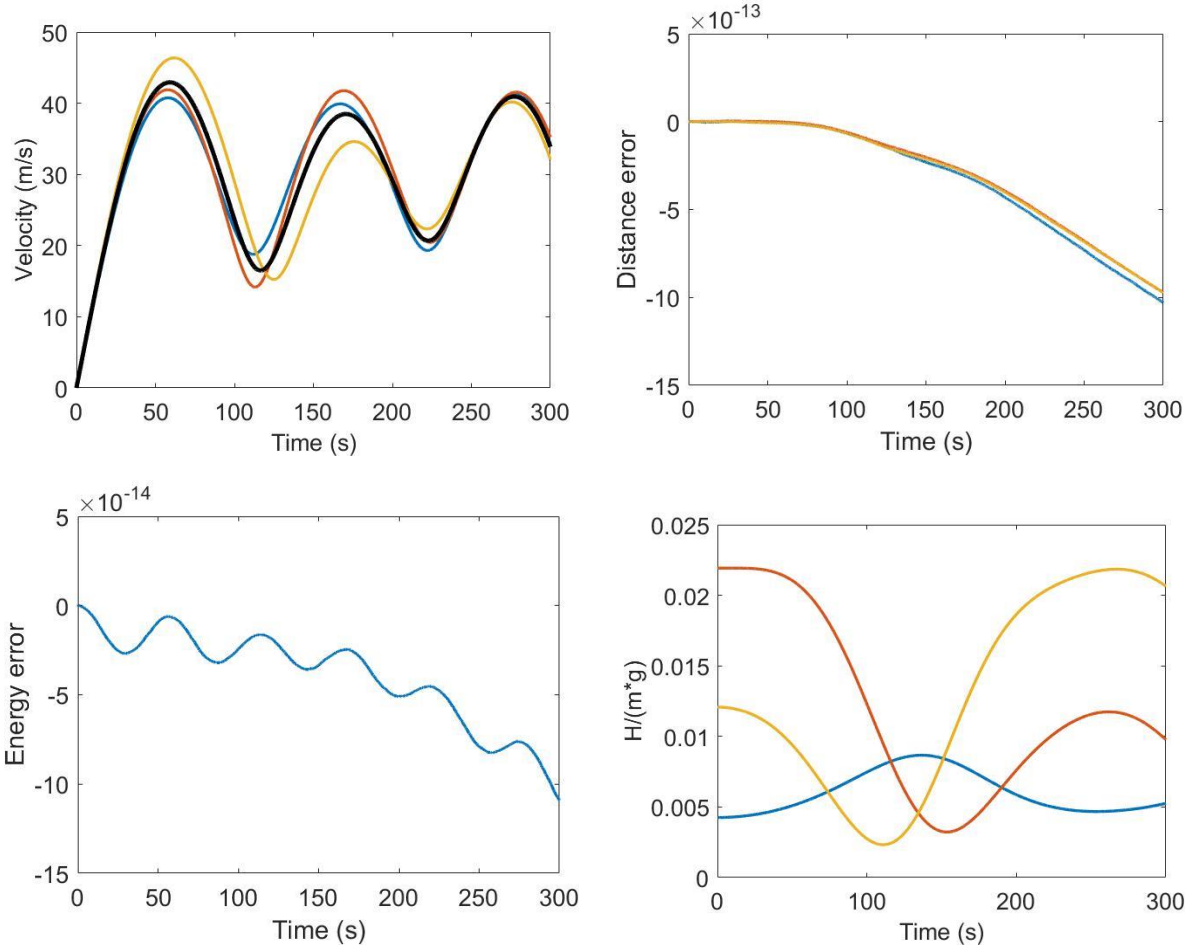

Figure 3.3 Results for simulation A1. Velocity (upper left), distances error (upper right), energy error (lower left) and normalized interaction forces (lower right) are shown. The CoM velocity is the black line. The numerical errors shown in the graph are normalized over the initial values. The total energy is computed with respect to the potential energy minimum, and the energy error is normalized over the initial total energy. The interaction forces are normalized over the average gravity force acting on the system.

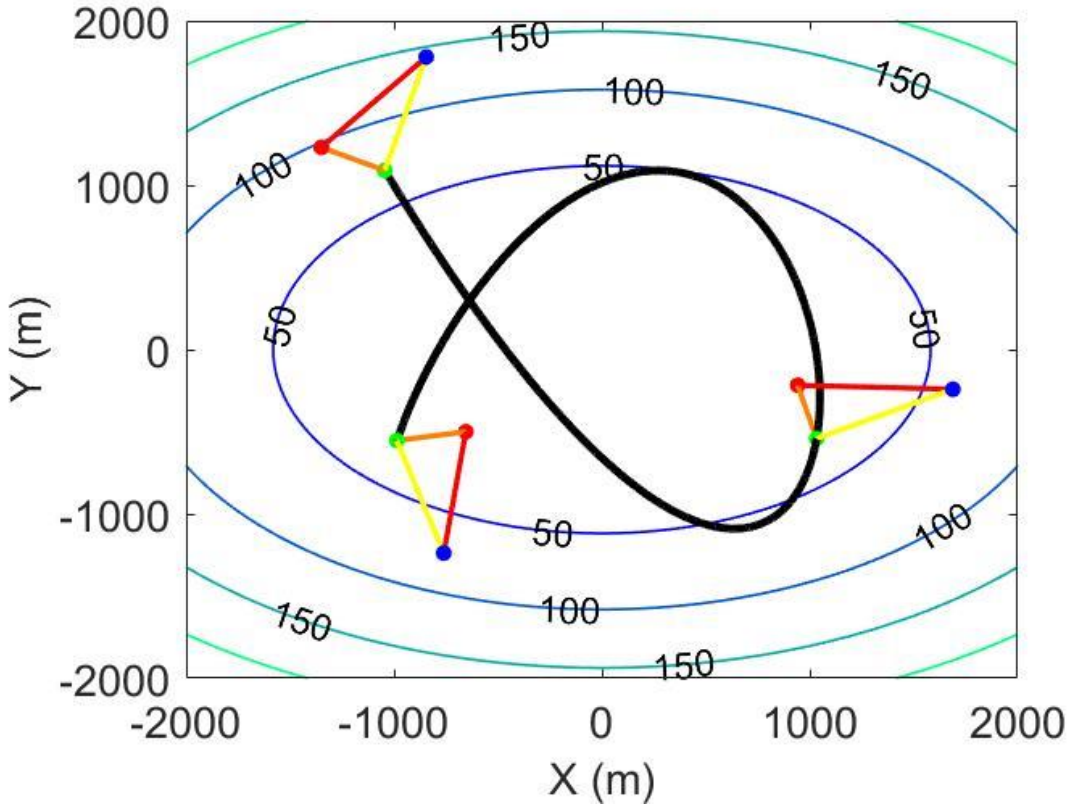

Figure 3.4 CoM trajectory (black line) for simulation B1 involving one mass (green) that is 1000 times greater than the others. See Figure 3.2 for the rest of the caption.

Case B1 shows the motion of a triangle-shaped structure with the mass concentrated in the green point mass, that is initially set down-hill with respect to the others. The system CoM is practically on the green mass, as we can see in Figure 3.4, where the CoM trajectory is shown to touch always the green mass. The motion shows smaller oscillations on the ellipsoid slopes with respect to the case A1. The motion is mainly driven by the green mass that reaches a velocity maximum that is lower than for the case A1, due to its lower initial position. In fact, as we can see in the upper left panel of Figure 3.5, the velocity peaks are in the order of 37 $\frac{m}{s}$. Despite the oscillating behavior similar to case A1, some differences can be seen in the velocity of the blue mass (yellow curve). Overall, the interaction forces are weaker than in case A1 (Figure 3.5, bottom right panel). They show a similar behavior during the motion, even if initially h_3 is attractive. Despite the oscillations, the largest force tends to be h_2. The system energy and the distances between the masses are very well preserved during the motion, as we can see in the bottom left and upper right panel in Figure 3.5, respectively.

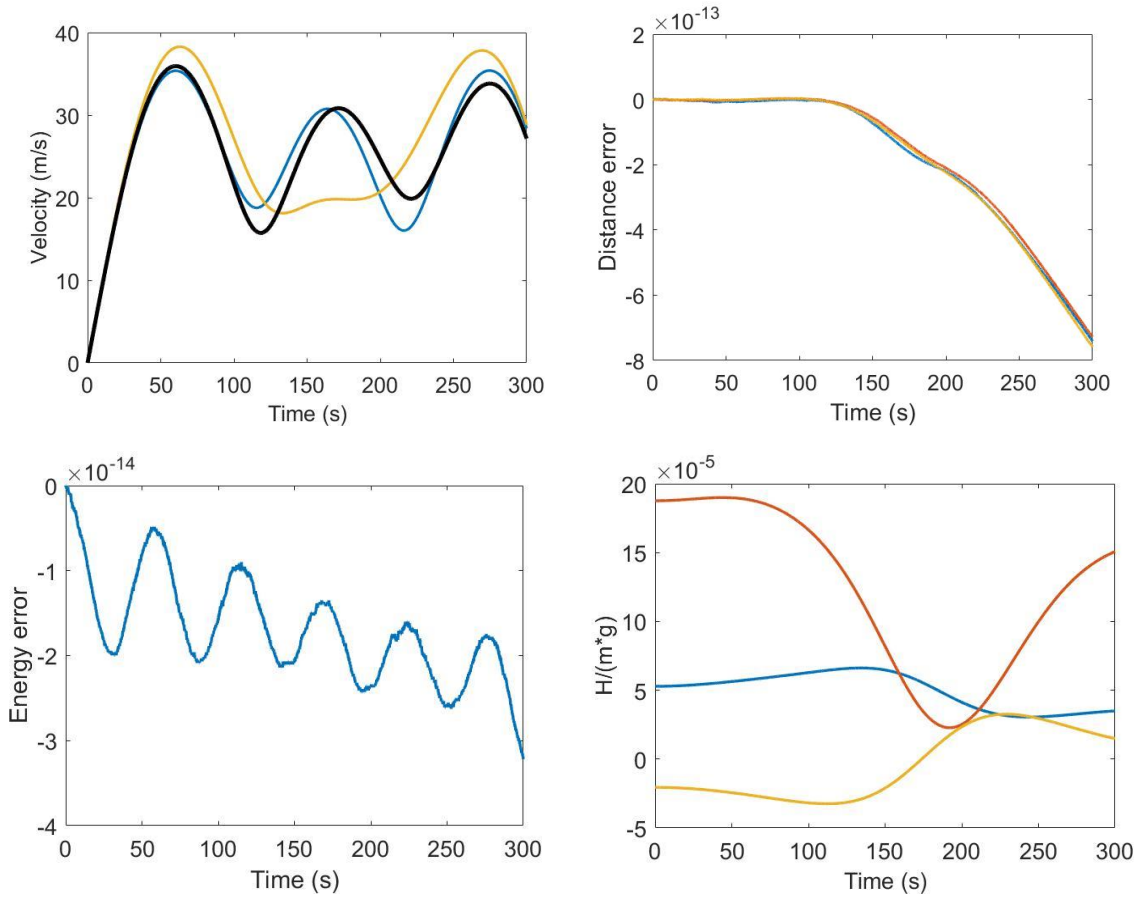

Figure 3.5 Results for simulation B1. See Figure 3.3 for the rest of the caption.

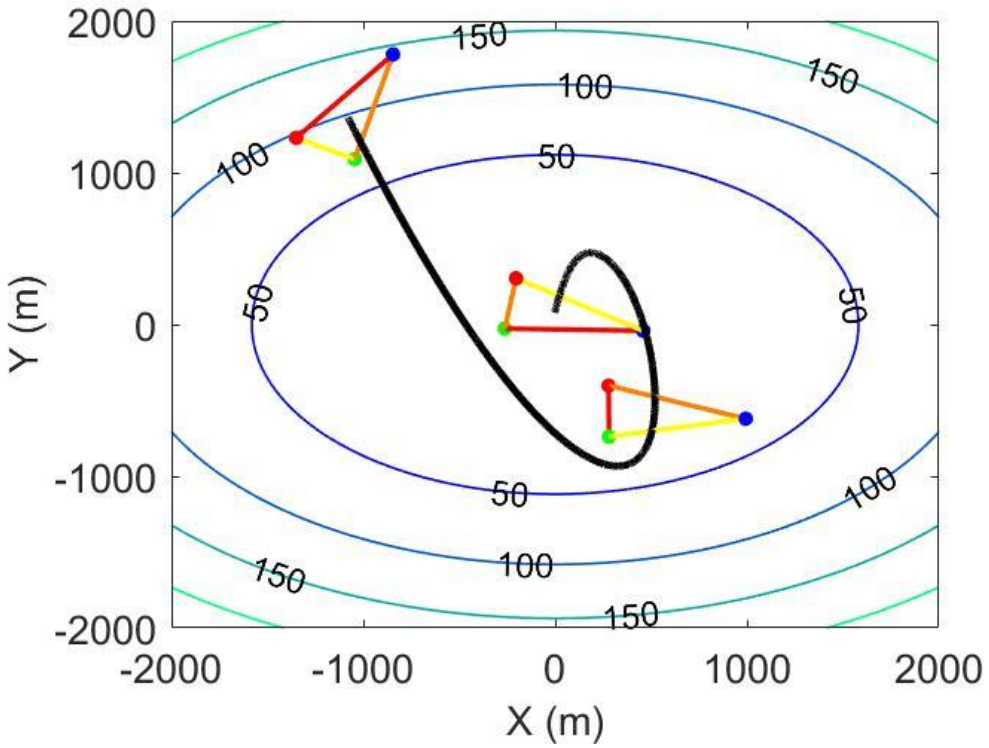

Figure 3.6 CoM trajectory for simulation C1. See Figure 3.2 for further details.

Simulation C1 presents the same mass distribution as the case A1, but the motion occurs under the effect of friction. As expected, the motion slows down with loss of energy (bottom left panel of Figure 3.7) depending on the specific value of the friction coefficient μ. It is relevant to point out that friction influences also the behavior of the interaction forces. The CoM trajectory (Figure 3.6) presents just a couple of oscillations on the ellipsoid slopes. The system slows down after an initial velocity maximum of about 35 $\frac{m}{s}$. The inter-mass distances are constant during the motion (upper right panel in Figure 3.7). The interaction forces are initially quite close to the ones of case A1, but during the motion, they present different behaviors (bottom right panel in Figure 3.7).

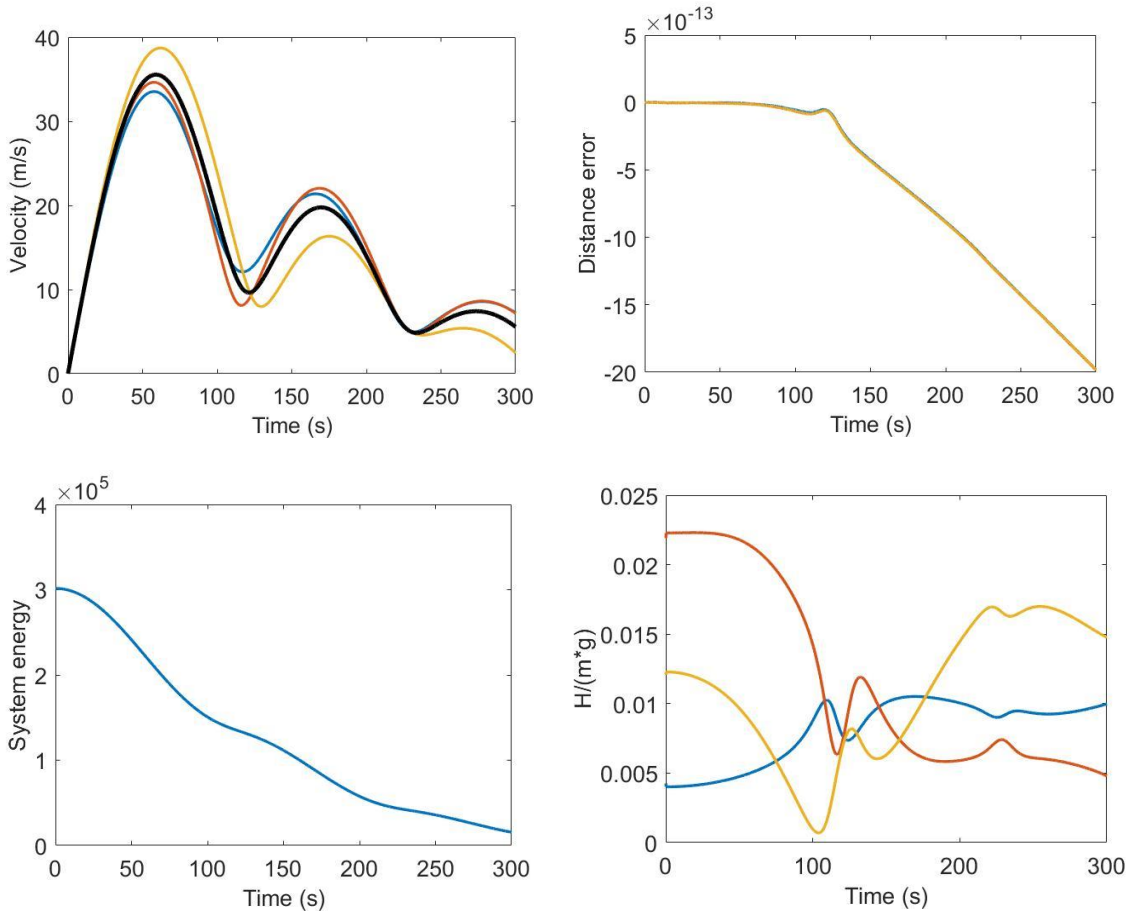

Figure 3.7 Results for simulation C1. The total energy is computed with respect to the potential energy minimum. It tends to decrease due to bottom dissipation. See Figure 3.3 for further details.

3.2.2. An analytical solution for the triangle

The simple cases treated in the previous section were introduced to provide a rough picture of the main model features, such as assumptions and potential applications. Let us now focus the attention on the nature of the interaction force $\vec{h}_{ij}$. To this purpose, we will illustrate a particular case where this force can be given an exact analytical solution.

Let's consider three equal masses set at the vertices of an equilateral triangle within a sphere cup of radius r, centered in the point $(0,0,r)$, so that the origin coincides with the bottom of the sphere. All masses are set at the same altitude $z = r(1 - cos\theta)$, as is shown in the sketch of Figure 3.8. The distance between the masses coincide with the sides of the triangle and is equal to $d = \sqrt{3}\, r \sin\theta$, where θ is the colatitude of the masses, i.e. the angle between the z axis and the line joining the sphere center with any mass. By considering an initial horizontal velocity $\vec{v}_0$ tangent to the sphere, the motion is forced to occur on the circumference of radius $r \sin\theta$.

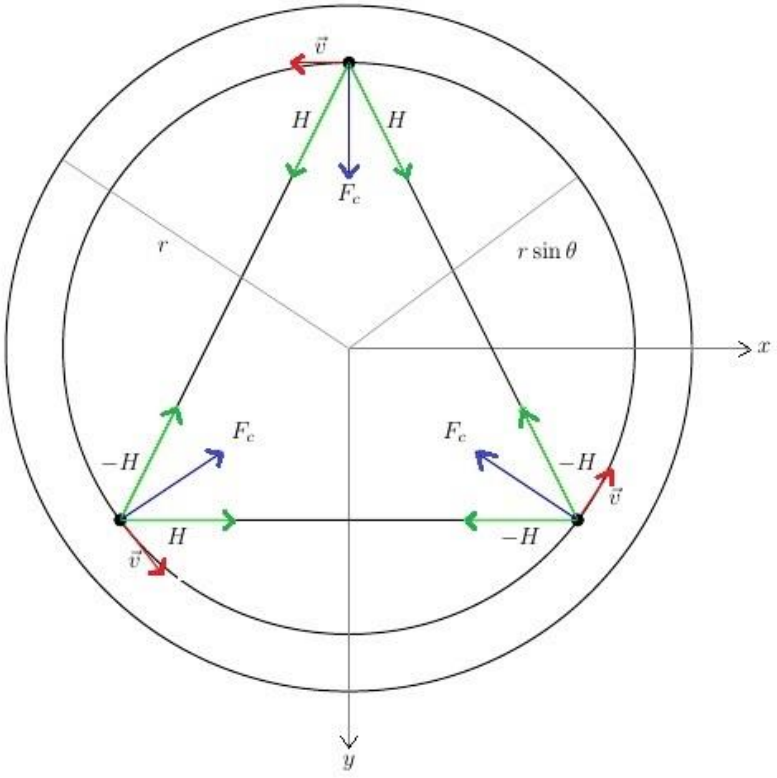

Figure 3.8 Sketch of the motion of a system of three equal masses set at the vertices of an equilateral triangle spinning horizontally on a sphere cup, seen from above. The equal interaction forces are denoted with green arrows. The initial velocity $\vec{v}_0$ of the masses is represented by red arrows.

Due to the peculiar geometry, all masses are subject to a reaction force with the same magnitude, and this equality holds also for the gravity force and the pair of interaction forces. If we take a specific mass, the reaction force R is directed along the sphere radius toward the center of the sphere, the gravity force is vertical downward, and the interaction forces are aligned with the two triangle sides that meet at the mass vertex. Let's consider the conditions under which the mass motion is circular and stationary. As said before, their trajectory is the horizontal circumference of radius $r \sin\theta$ where they move at uniform velocity v_0. In the direction of the radius of this circumference, the centripetal force has to balance the component of the reaction force $R \sin\theta$ as well as the components of the

interaction forces. Notice that in this balance, the gravity force plays no role. Considering that the interaction forces form an angle of $\frac{\pi}{6}$ with the radius, we can therefore write the following equation:

$$m\frac{v_0^2}{r\sin\theta} = R\sin\theta - \sqrt{3}\,h$$

where the centripetal acceleration term is on the left side member, h is the interaction force acting along a single edge, m is the particles mass and R is the reaction force exerted by the sliding surface. While running on the horizontal circumference, the mass runs also on the great circle of radius r passing through the instantaneous position of the mass. Even on this circumference the centripetal force, directed toward the center of the sphere, has to balance the sum of all active forces, including gravity. It is thus possible to write the following equation:

$$m\frac{v_0^2}{r} = R - mg\cos\theta - \sqrt{3}\,h\sin\theta$$

where g is the gravity acceleration.

The two equations together form a linear system of equations in the unknowns R and h, that has solutions

$$R = \frac{mg}{\cos\vartheta} \qquad 0 \le \vartheta \le \frac{\pi}{2}$$

$$h = \frac{mg}{\sqrt{3}}\left(\tan\vartheta - \frac{v_0^2}{rg\sin\vartheta}\right) \tag{3.5}$$

This basic formula can be easily extended to a generic number of equal particles set at the vertices of regular polygons spinning on the same horizontal circular plane in a sphere cup. The expressions for the interaction forces acting on the edges of polygons differ just by a numerical coefficient. This example is very useful to understand the repulsive/attractive nature of the interaction force. In fact, once the angle θ is set, the force h will be positive, and then repulsive, for low values of the initial velocities. Indeed, in this case, the particles would normally tend to fall toward the sphere cup center in absence of interaction and therefore would tend to reduce their mutual distances. On the contrary, for higher v_0 the force h is attractive (negative) because the masses would normally escape the sphere cup and would tend to increment their distances. Formally:

$$h \ge 0 \quad if \quad v_0^2 \le rg\sin\theta\tan\theta \tag{3.6}$$

In the special case where $v_0^2 = rg\sin\theta\tan\theta$, which can be designated as the escape velocity, the internal forces are all zero, and the masses move as they were totally independent from one another. Note that this last case has been treated explicitly for a two-mass system in the Appendix B.

In Figure 3.9 we show the results for a simulation of three equal $m = 100\ kg$ point masses over a sphere cup of radius $r = 200\ m$. The motion occurs on the $r\sin\theta = 180\ m$ circle inside the sphere cup, with an initial velocity $v_0 = 10\frac{m}{s}$. The simulation is computed for $t = 300\ s$, with a time step of $dt = 0.1\ s$. The mass velocities are all equal to v_0 during the entire motion, as we can see in the upper left panel of Figure 3.9 (yellow line). On the contrary, the CoM is not moving since it is located in the circle center (black line). Distance and energy are preserved during the motion with high accuracy. The interaction forces error computed by comparing the numerical results and the exact analytical expression (3.5) is shown in the bottom right panel.

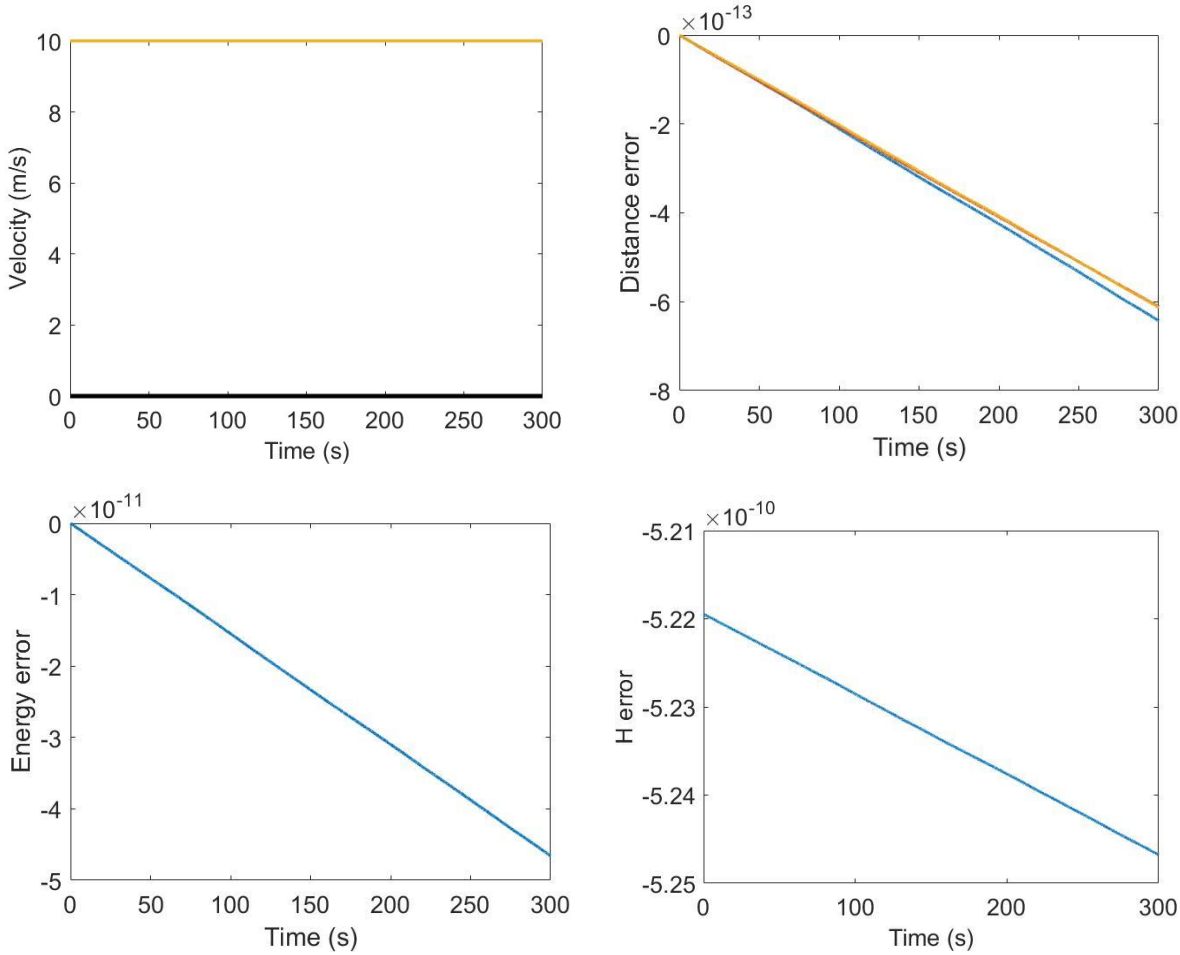

Figure 3.9 Results for a three mass system spinning with constant angular velocity inside the sphere cup as sketched in Figure 3.8. Velocity (upper left), normalized distances error (upper right), normalized energy error (lower left) and normalized error for the interaction forces (lower right) are shown. The interaction forces are normalized by means of the exact solutions (3.5).

3.3. The extension to N point-mass systems

In this section, we will extend the model to a larger number of masses interacting through internal forces h_{ij}, that are such to keep the 3D distances constant. This generalization is made here by means of a Delaunay planar triangulation: for a set of N points in a plane, the characterizing property of such a triangulation $DT(N)$ is that no point in N is inside the circumcircle of any triangle in $DT(N)$. Delaunay triangulations maximize the minimum angle of all the angles of the triangles in the triangulation, avoiding triangles with one or two extremely acute angles.

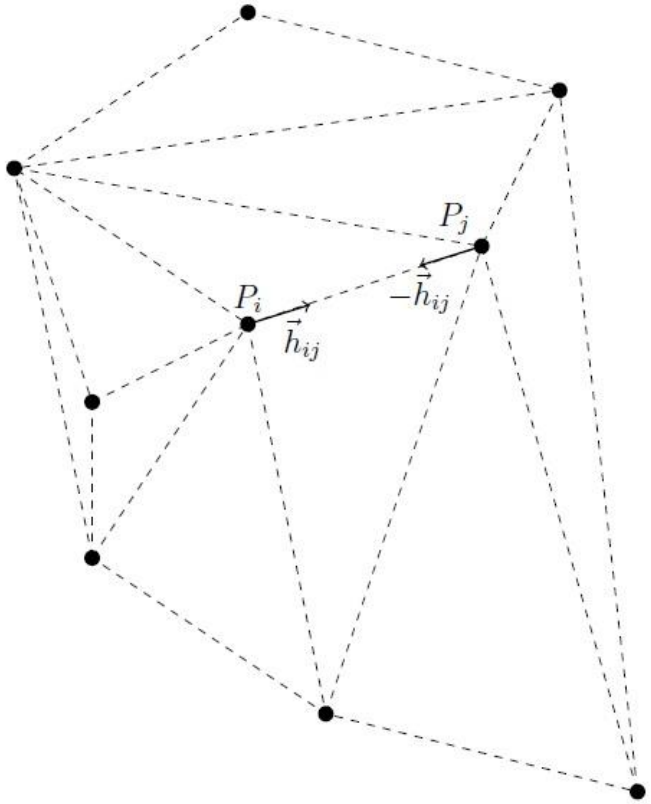

Figure 3.10 Example of a $N = 9$ point-mass grid. The particles are connected through a Delaunay triangulation. The interaction forces h_{ij} act on the edges of the triangles connecting the points.

We notice that for each set of N point masses one can establish the total number of interaction forces n and an index $s = 1,2, \dots, n$ in such a way that h_s uniquely identifies the pair of point masses i and j that interact, with i and j running over the set [1, N]. Bearing this in mind and following the considerations of Section 3.2, the equations of motion of the generic point P_i can be written in the compact form:

$$m_i \ddot{\vec{r}}_i = \vec{F}_i - \vec{G}_i \tag{3.7a}$$

$$\vec{G}_i = -\sum_p h_{s(p)} \vec{r}_{ij} + \sum_q h_{s(q)} \vec{r}_{ij} + \sum_p h_{s(p)} (\vec{r}_{ij} \circ \vec{n}_i) \vec{N}_i - \sum_q h_{s(q)} (\vec{r}_{ij} \circ \vec{n}_i) \vec{N}_i \tag{3.7b}$$

where $\vec{G}_i$ may be defined as the interaction vector since it contains the contributions of all the interaction forces acting on the i-th mass. In the Eq. (3.7b) the summation with index p extends over the subset of h_s ($s = 1,2, \dots, n$) including the pairs of masses (i, j) where j identifies the masses that interact with the i-th mass and such that $j < i$. Likewise, the summation with index q covers all the

interacting masses with $j > i$. The term $\vec{F}_i$ represents all the other forces acting on the *i*-th mass, and can be given the expression:

$$\vec{F}_i = m_i\,\vec{g} + m_i\,\vec{N}_i\left(\ddot{\vec{r}}_i - \vec{g}\right) \circ \vec{n}_i = -m_i g\vec{k} + m_i\,\vec{N}_i[(g\vec{k} + \vec{n}_i(\dot{\vec{r}}_i \circ \dot{\vec{r}}_i)/R_i) \circ \vec{n}_{i_i}]$$

Here $\ddot{\vec{r}}_i \circ \vec{n}_i$ and $\dot{\vec{r}}_i$ are the centripetal acceleration and velocity of the point P_i. Further, R_i is the local radius of curvature, $\vec{k}$ is the vertical unit vector pointing upwards, $\vec{N}_i$ represents the *correction* to $\vec{n}_i$ due to the basal friction force acting opposite to the velocity, that is:

$$\vec{N}_i = (\vec{n}_i - \mu\,\vec{t}_i)$$

In a way similar to what we did in the three-mass case, we can use the constraints on the 3D distances between each pair of point masses to evaluate the interaction forces. Considering these constraints in terms of acceleration differences, we can write the expression:

$$(\vec{F}_i - \vec{F}_j) \circ \left(\vec{r}_i - \vec{r}_j\right) + \left(\frac{\vec{G}_i}{m_i} - \frac{\vec{G}_j}{m_j}\right) \circ \left(\vec{r}_i - \vec{r}_j\right) = -\left(\dot{\vec{r}}_i - \dot{\vec{r}}_j\right) \circ \left(\dot{\vec{r}}_i - \dot{\vec{r}}_j\right) \qquad (3.8)$$

for any couple of masses P_i and P_j that interact with each other, along all the n edges of the Delaunay triangulation $DT(N)$.

Also in this case, the previous equations can be written in a compact form:

$$\boldsymbol{h} = \boldsymbol{\theta}^{-1}\boldsymbol{a}$$

where $\boldsymbol{h}^T = [h_1; h_2 \ldots; h_n]$, $\boldsymbol{\theta}$ is an $n\,x\,n$ coefficients matrix derived from Eq. (3.8), and $\boldsymbol{a}$ is the $n-$vector containing all the terms in Eq. (3.8) that depend on the velocities and positions of the point masses. The generic element *s* of the vector $\boldsymbol{a}$ is given by:

$$-(\vec{F}_i - \vec{F}_j) \circ \left(\vec{r}_i - \vec{r}_j\right) - \left(\dot{\vec{r}}_i - \dot{\vec{r}}_j\right) \circ \left(\dot{\vec{r}}_i - \dot{\vec{r}}_j\right)$$

where *i* and *j* are uniquely determined once *s* is given. Every element of this vector corresponds to a pair of masses in the system exerting a mutual interaction. The relationship between the index s and the indices *i* and *j* is one of the classical output items of any Delaunay triangulation code.

Notice that this first generalization of the model to a set of N point masses is based on the partition of the system of the inner forces in triangles: each edge of the triangles is associated with the interaction force between two point masses located at the vertices of the edge. We will show however that this is not the most convenient generalization. In the following, a number of examples will be discussed based on the Delaunay triangulation. The problem is that if, on an N-mass system sliding on a given surface, we impose that all the n distances along the edges of a $DT(N)$ remain constant, the number of constraints might be too large. We can say this by stating that we impose more constraints than the degrees of freedom of the system. The remedy can be found on reducing the number of constraints, in such a way however that the whole system behaves as a semi-rigid body: that is the 3D mass distances are conserved also along those edges where formally no constraint is imposed. However, finding the configuration of edges ensuring body rigidity is a tricky task, usually with no unique solution. In the next simple examples, we will discuss this difficulty and show that there is no general rule. This is the main reason why the Delaunay triangulation is not the best option, since we must remove some of the $DT(N)$ connections to describe a physically consistent system. In other words, even if the set of equations (3.7) – (3.8) is correct, they can lose physical meaning if we do not choose the proper subset of constant-edge conditions.

3.3.1. Examples of N-point systems

In this section, we will deal with the motion of systems formed of $N > 3$ point masses sliding down analytical surfaces and interacting with each other. Through a number of examples, we will prove that, once N is given, the configurations (or patterns) of the n edges connecting the masses have to be chosen properly in order to get a well-conditioned problem. In Table 3.3 we summarize the main features of the simulations we use as illustrative cases. To permit a straightforward comparison, the sliding surface is the same elliptic paraboloid selected in Section 3.2.1. In what follows, we set the point masses in such a way that they form two regular shapes. In the former, they lie on the boundary of an elliptical figure with area $S_E = 4.9\ 10^5\ m^2$, while in the latter they lie on the boundary and inside a rectangle with area $S_R = 4.8\ 10^5 m^2$. Both systems are centered in the same point along the slope, i.e. the point $P_c = (-1000;\ +1200;\ +85)\ m$ (see Fig. 3.11).

Simulation	Mass grid shape	Number of point masses N	Number of inner forces n	$m\ (kg)$	Simulation time $t(s)$	Friction coefficient μ	Results
A2	Ellipse	15	27	100	800	0	
B2	Ellipse	45	87	100	800	0	
C2	Ellipse	15	27	2-500	300	0.02	
D2	Rectangle	21	44	100	-	0	Singular
E2	Rectangle	21	38	100	300	0	Singular
F2	Rectangle	21	39	100	800	0	

Table 3.3 Main data for the simulations A2-F2.

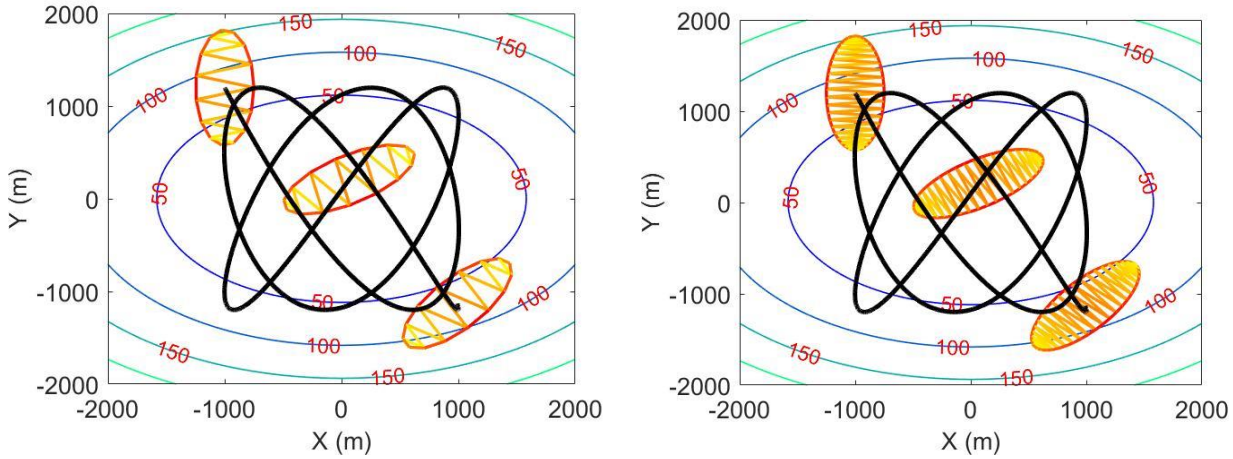

Figure 3.11 CoM trajectory for simulations A2 (left panel) and B2 (right panel). The magnitude of the interaction forces is represented with a colour code, ranging from yellow (smaller values) to red larger values, at the instants $t = [0;\ 400;\ 800]$ s. Notice that the strongest connections are the ones along the perimeter of the elliptical polygon P_{CH} (see below) in all the selected positions, for both simulations.

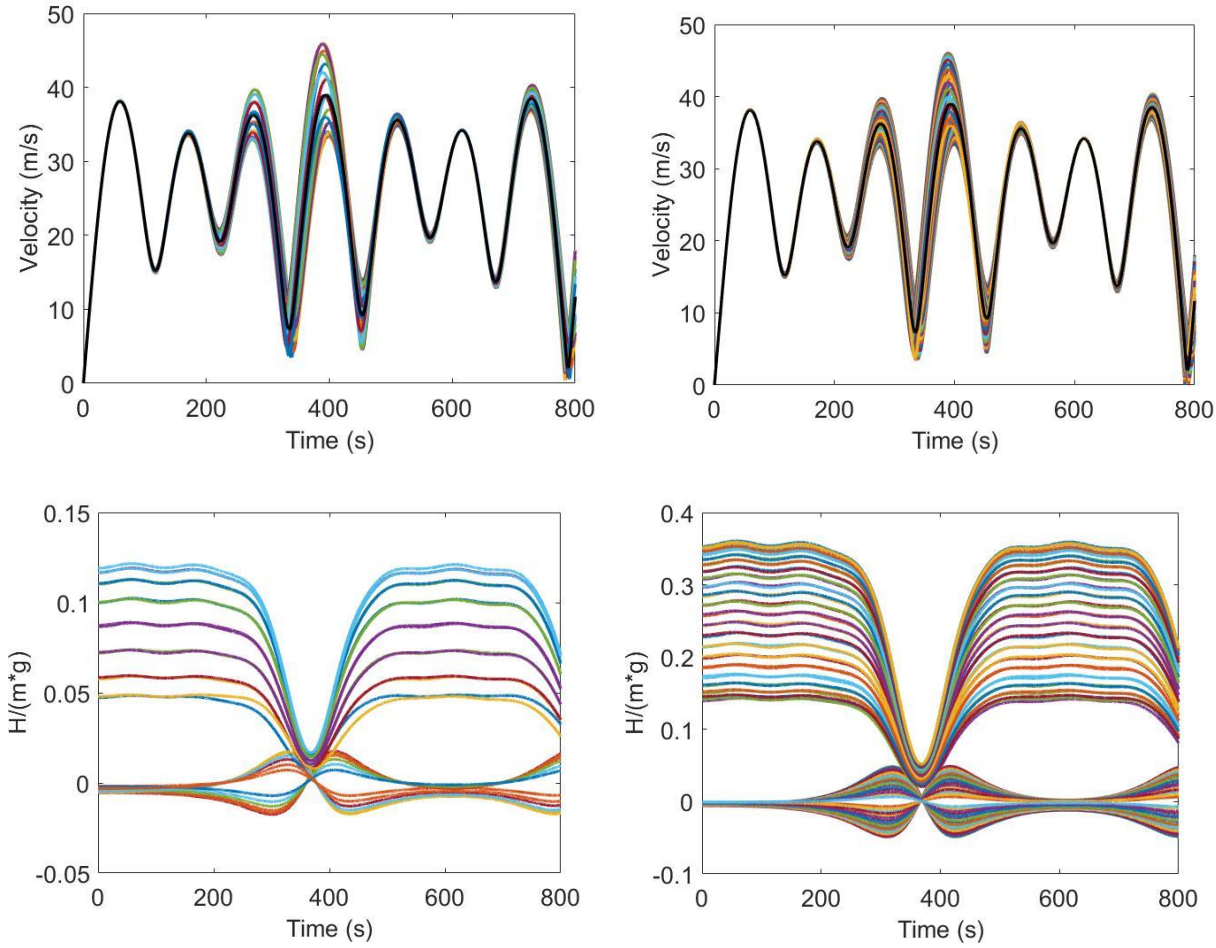

Figure 3.12 Mass velocities for simulations A2 and B2 (upper left and right panels, respectively). The CoM velocity is denoted with the black line. In the bottom panels, the interaction forces are portrayed. Notice that the B2 case presents stronger forces. Internal forces and velocities show a quasi-periodic behaviour and nearly repeat every ~ 550 s. Consider that around 380 s all the forces go to zero for the selected geometry. In this specific condition, all masses stay at the same Cartesian distances without the need of internal forces.

The simulations A2 and B2 are useful to understand how the number of point masses can change the magnitude of the internal forces. Cases A2 and B2 indeed share the same geometry. But the number of masses in B2 is three times larger than in A2. Since the individual masses are the same, it means that the total mass of the system B2 is larger than the one of A2 by a factor of 3. This, however, as expected, does not influence the general sliding dynamics. More specifically, the CoM trajectories are equal (Figure 3.11) and the masses move over the slope at the same velocity in both cases (upper panels in Figure 3.12). Notice that any $DT(N)$ in a plane defines a polygon that is the convex hull, say the polygon P_{CH}, of the system. All triangles of the $DT(N)$ have one vertex on one side (along the perimeter of P_{CH}) and the two other vertices on the other side (i.e. they are diagonals of P_{CH}). In both simulations, it is found that the internal forces along the ellipse boundary (P_{CH} perimeter) are much stronger than the forces along the P_{CH} diagonals. The interaction forces plots (bottom panels in Figure 3.12) present similar behaviors, but in case B2 they reach values as high as 35 % of the mean gravity force. It is interesting to observe that all forces become negligibly small at t =380 s, the instant at which the forces along the P_{CH} diagonals change signs. In this instant, the masses are at the same Cartesian distances without the need of interaction forces. This is due to the peculiar geometry selected.

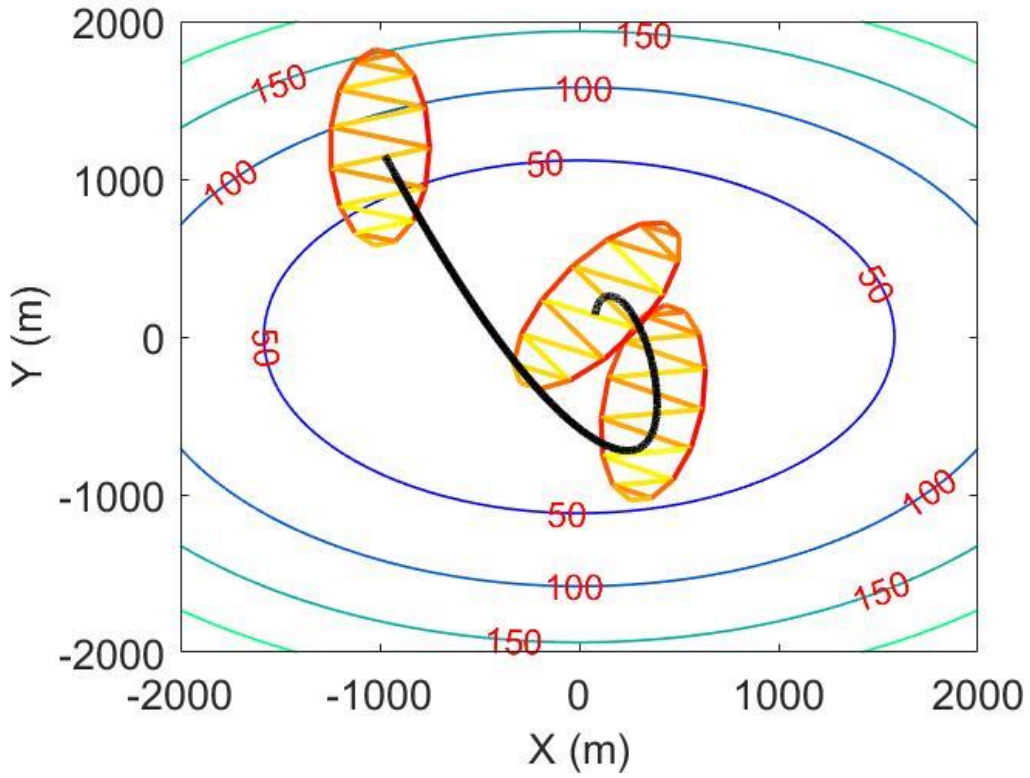

Figure 3.13 CoM trajectory for simulation C2. The friction force clearly affects the general behaviour of the system. Masses slow down while turning down the ellipsoid flanks. Notice that the general motion is similar to the motion of the 3-mass system in simulation C1 (see Figure 3.6).

Velocities show peaks in the order of 30 m/s (left panel in Figure 3.14). In the final spin (around 225 s), some masses stop, which interestingly has the effect of changing abruptly the interaction forces (right panel in Figure 3.14).

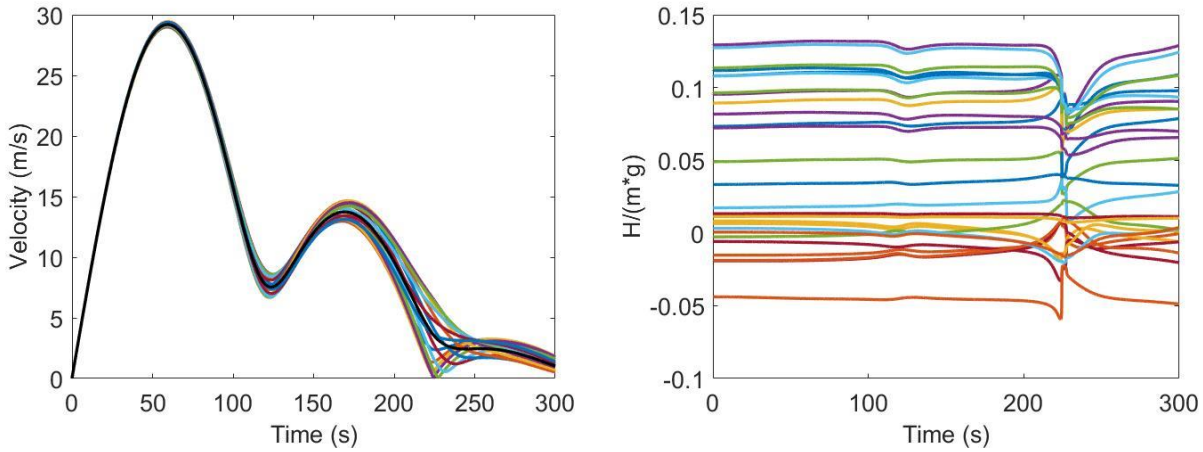

Figure 3.14 Results for simulation C2: mass velocities on the left panel and interaction forces on the right one. The CoM velocity is the black line.

Let us now discuss further simulations where masses are set along a regular rectangular grid and interactions occur on the edges of a regular Delaunay triangulation (see Figure 3.15). Masses are equally spaced in the $x$and y directions at a mutual distance of 200 m.

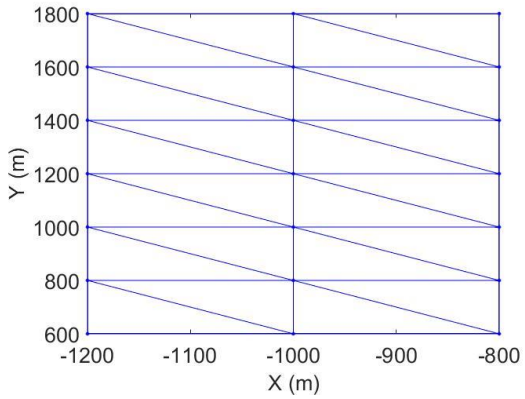

Figure 3.15 Basic mass grid for simulation D2. The point masses are equally spaced by $200\ m$ in both x and y directions and occupy the vertices of the triangles. The simulation cannot run since the coefficients' matrix $\boldsymbol{\theta}$ is singular and cannot be inverted.

If we impose constraints on all the edges of the triangulation the structure is over-constrained, i.e. the number of constraints is too large. To understand this better, let's consider that the degrees of freedom of a set of non-rotating non-interacting N point masses moving on a surface is *2N*. Since a rigid body moving on a surface has 3 degrees of freedom (2 associated with the motion of its CoM and 1 associated with the rotation of the system around an axis passing through the CoM) one cannot impose more than $N_R=2N-3$ constraints. Unfortunately, the number of edges n of a *DT(N)* may exceed N_R, which leads to what we call here hyper-rigidity. For instance, for a set of $N=N_x\,x\,N_y$ points like in Figure 3.15 (N_x=7, N_y=3, N=21), it may be easily shown that the total number of edges n of a DT($N_x x N_y$) is given by $n = 3N - 2(N_x + N_y) + 1$. For the case illustrated in Figure 3.15, n turns out to be equal to 44, that happens to be larger than the total admissible constraints (N_R= 39) for a rigid body. From a numerical point of view, the excess of constraints has the effect that the coefficients matrix $\boldsymbol{\theta}$ becomes singular and cannot be inverted. So, the problem of computing the internal forces vector $\boldsymbol{h}$ cannot be solved. The immediate remedy for this seems to be the removal of as many as $n - N_R$ constraints, which geometrically means removing some edges from the triangulation. Going back to the example of Figure 3.15, if one removes as many as 5 edges, thus the 21 masses, altogether, would have exactly the same degrees of freedom as a rigid body. However, if we remove more than 5 edges, the masses have more degrees of freedom and the system can deform. In the example illustrated in Figure 3.16, we have removed all the 6 diagonal edges on the left side of the structure of Figure 3.15. The related simulation is denoted as simulation E2. As may be seen, the masses on the two columns on the right side move as constrained in a rigid structure with interaction forces acting along the edges of triangles, while the masses belonging to the column on the left side have less bounds: the quadrilaterals which they belong to are allowed to deform during the motion.

It is worth stressing here that, while the N-mass system is sliding, the sides of the quadrilaterals where the diagonal elements have been removed can get closer to each other and even *cross* each other, since there are not enough bounds to keep them at a given distance. When edges overlapping occurs, the problem becomes unstable and simulation provides meaningless results. In other words, if the deformation becomes too large, this can lead to some numerical difficulties, but what is worst, this undermines the interpretation of the N-mass system as an acceptable representation of a sliding continuous body. How to pass from a quasi-rigid body model to a deformable body model, is a generalization that will be addressed in the next chapter.

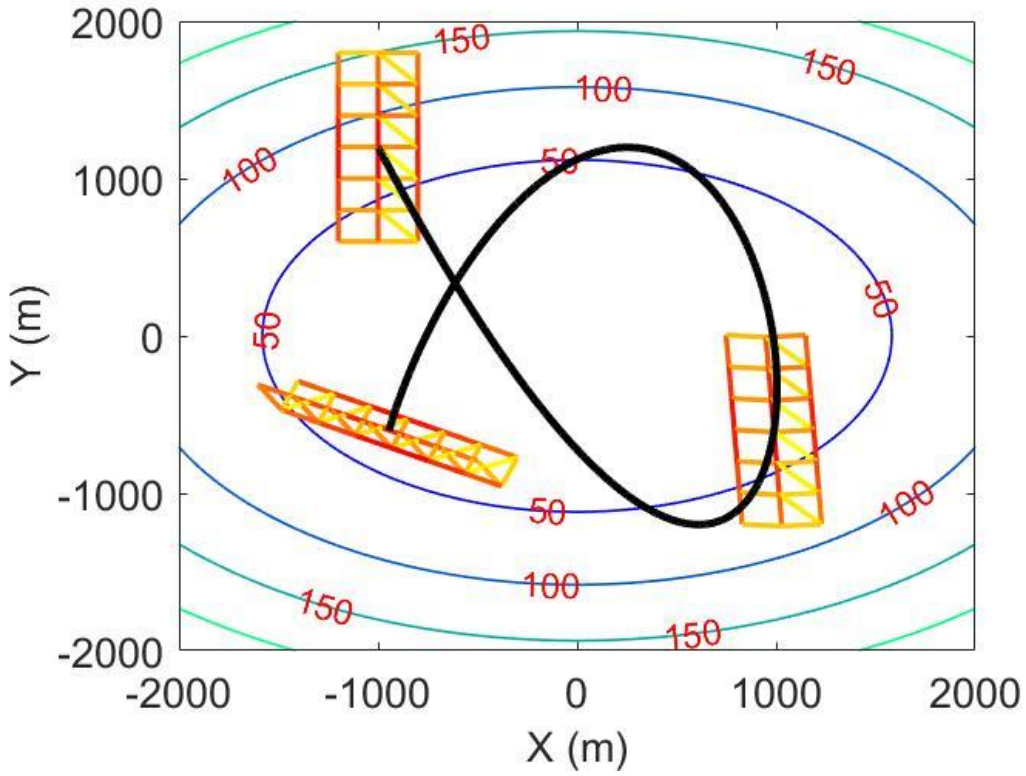

Figure 3.16 CoM trajectory for the simulation E2. The magnitude of the interaction forces is represented with a colour code, ranging from yellow (smaller values) to red (larger values), at the instants $t = [0;\ 150;\ 300]$s. Notice that in the final stages, some of the edges tend to overlap. The simulation could not be run beyond 300 s.

Simulation F2 handles the case where the number of removed edges (5) is such that the total number of degrees of freedom of the N-mass system equals the one of a rigid body. As we can see from Figures 3.17 and 3.18, F2 provides physically meaningful results. The body trajectory and velocity are similar to the A2 simulation since the basic setting is equal. The only clear difference in this last case lies in the behavior of the interaction forces, that present wider variations with respect to the case A2. Nevertheless, an instant where all interaction forces happen to be negligibly small can be found also here. One more analogy is that the forces acting along the external edges tend to have the largest magnitude during the motion.

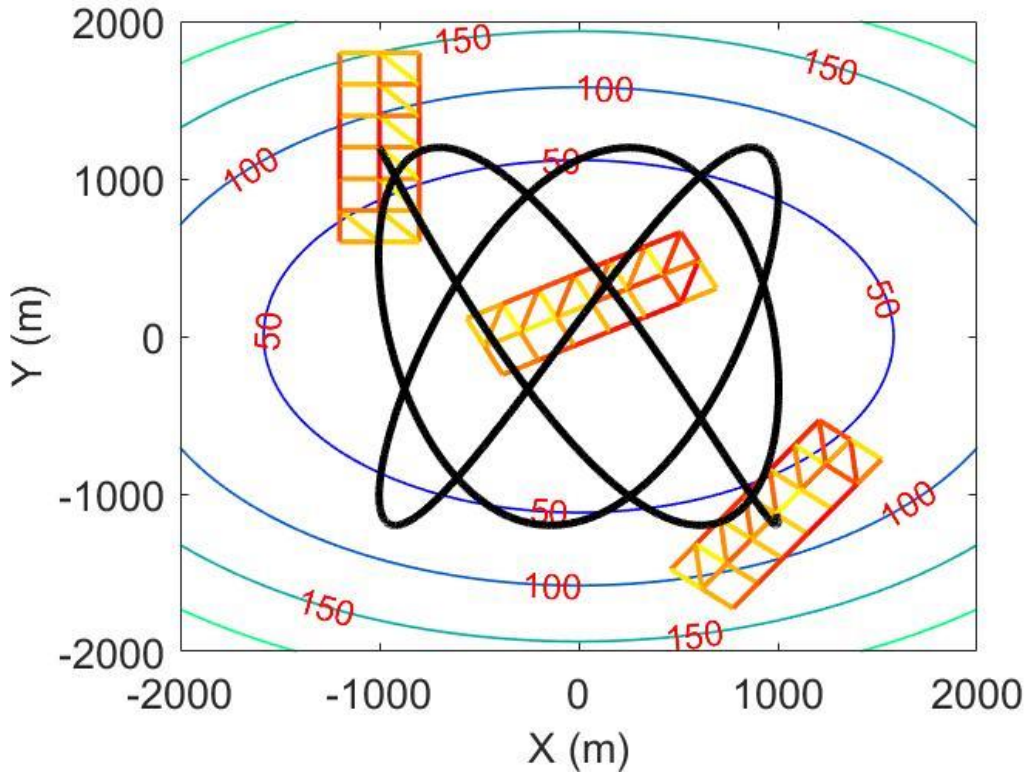

Figure 3.17 CoM trajectory for the simulation F2. The interaction forces magnitude is represented through colours, ranging from yellow to red, at $t = [0;\ 400;\ 800]$ s.

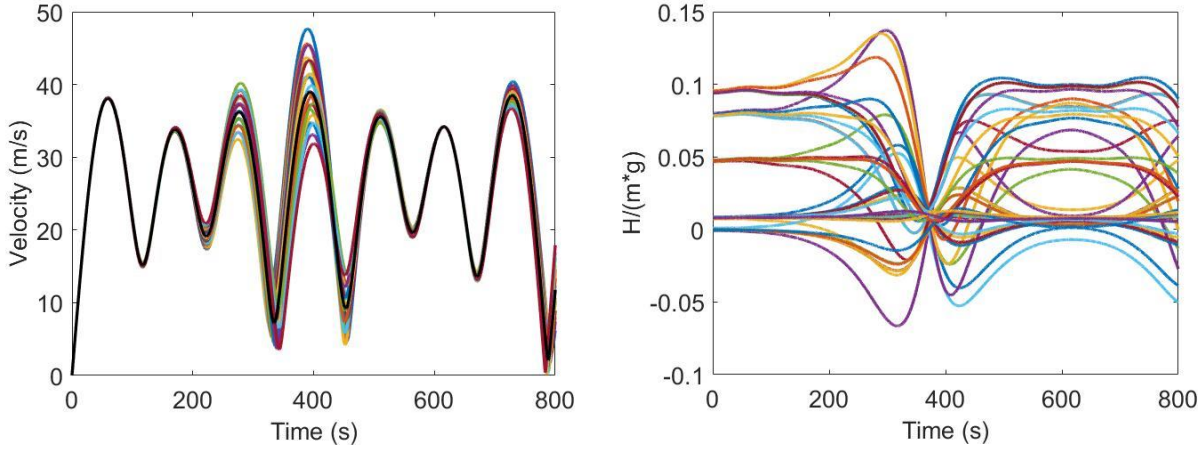

Figure 3.18 Velocities (left panel) and interaction forces (right panel) for simulation F2. The CoM velocity is shown with the black curve. Results are similar to the case A2, as we expect. Some differences can be found in the plot of the interaction forces. Noticeably, an instant with no interaction forces can be found also here around 380 s.

Chapter 4

4. The numerical model UBO-Inter

4.1. Introducing the deformable body approach

In the previous chapter, we have discussed the influence of the selection of the pattern of the inner bounds on the dynamics of the N-mass system. The simulations A2-F2 in Chapter 3 suggest us that this choice cannot be arbitrary, since over-determining or under-determining the system can lead to different results, i.e. one can pass from problems that are ill-conditioned and do not admit any solutions for the interaction forces (case D2), to quasi-rigid body problems (case F2) and to deformable body problems that can even degenerate to impossible problems (case E2).

Mathematically, this translates to the singularity or quasi-singularity of the coefficients matrix $\boldsymbol{\theta}$ that in our formulation has to be inverted at any time step to get the vector of the interaction forces $\boldsymbol{h}$**.** If the configuration of the bonds is such that, as a whole, the N-mass system has the same degrees of freedom of a rigid body, then the constant-distance systems moves on the gliding surface as it were a rigid body or a semi-rigid body. If the bonds are more, and then the degrees of freedom are less, the problem does not admit any solutions. If the links are less, then part of the system may move as a rigid body and the rest as a deformable body. In the previous chapter, we have considered links geometrically associated with triangulations, and we have concluded that the number of such links is usually too large in a generic N-point system, and, therefore, some of the edges have to be removed.

In this chapter, we explore the potential of constraints set along quadrangular patterns. If we consider systems with point-mass distributions such as the one given in Figure 3.16, but without the diagonal links, i.e. if we consider a set of $N=N_x\,x\,N_y$ point masses and we impose that the distances between the particles along the x-lines and y-lines are constant, then the total number of bonds results to be $2N-\left(N_x+N_y\right)$ that is smaller than N_R. Thus, the system results to be deformable, but it could deform to such extent that from a certain instant onward the mathematical problem cannot be solved anymore. To prevent this to occur, an additional force can be added along the diagonal of the quadrilaterals with the goal of limiting the extent to which the distance between the masses lying at the end of the diagonal can vary by shortening or lengthening. In other words, the geometrical pattern of the interaction forces, that is the geometrical mesh linking the masses (that we can denominate mass grid), forms a structure that is deformable and the level of deformation can be governed by an interaction law depending on the distance between the masses. This force is introduced in this thesis by means of the following law:

$$P_{ij}=\frac{m_i m_j}{m_i+m_j}\,g*k(w)$$

where m_i and m_j are the interacting masses, g is gravity, and $k(w)$ is a function depending on the instantaneous value of the relative lengthening of the inter-mass distance with respect to the initial value, i.e. $w = (l - l_0)/\, l_0$. More precisely, l is the distance computed at every time step and l_0 is its initial value. The function $k(w)$, shown in Figure 4.1 and adopted here, represents a simplified rheological behavior of the system material. It takes the form of a 6-parameter simple law:

$$k(w) = \max\left(\frac{\alpha w}{w - w_1}; k_{max}\right) \qquad if \qquad w \le w_1$$

$$k(w) = \frac{\alpha w}{w - w_1} \qquad if \qquad w_1 \le w < 0$$

$$k(w) = -\frac{k_{min}}{w_2} w \qquad if \qquad 0 \le w < w_2$$

$$k(w) = -\frac{k_{min}}{w_3 - w_2}(w - w_3) \qquad if \qquad w_2 \le w < w_3$$

$$k(w) = 0 \qquad if \qquad w_3 \le w$$

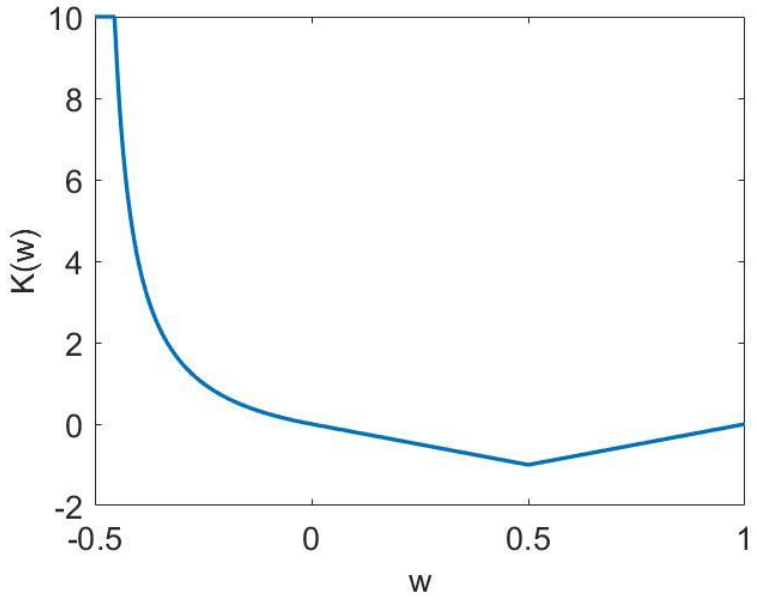

Figure 4.1 Function $k(w)$ for the parameters: $w_1 = -0.5, w_2 = +0.5\ w_3 = 1, k_{max} = 10, k_{min} = 1$. The function represents a simplified rheological behavior of the system material.

The force is positive, that is repulsive, when the distance tends to be shorter than l_0, and negative, that is attractive, otherwise. The function $k(w)$ is not linear. If it were linear, then it would act as a pure elastic force between the masses at the end of each diagonal. In case of shortening, it increases quickly up to a high level in the example of Figure 4.1. On the other hand, when lengthening exceeds the threshold w_2, then the force starts to diminish and beyond w_3 it becomes zero. This choice ensures that, basically, two masses subject to this kind of interaction are strongly prevented to come too close to one another, and further, that when they exceed certain distances the inner contrasting force becomes very week until it disappears. Basically, this describes a plastic behavior. We will apply these forces on masses that are separated by diagonal edges in the mass grid, while forces on the other

edges will be constant-distance forces, as the ones analyzed in Chapter 3. If distance changes along the diagonals are small, the behavior of the system is close to the one of an elastic body with shortening (compression) and lengthening (dilation) determined by elastic constants that may be however different from one another (see Figure 4.1). With this simple tool, mass grid quadrangles can deform along the diagonals. Impose that all sides of the quadrangles have length constant in time, then quadrangles behave in such a way that if a diagonal shortens, the other tends to increase its length. As a whole, this mechanism prevents extreme deformation of the quadrilateral elements of the force pattern and furthermore it ensures that the system is not overdetermined, ruling out any kind of hyper-rigidity conditions because the number of side edges (coinciding with the number of the constraints) is always lower than N_R.

In conclusion, in systems where point masses are set over a rectangular $N=N_x\, x\, N_y$ mesh, we will impose constant-distance constraints along the $N_E = 2N - (N_x + N_y)$ side edges and we will impose distance-dependent forces along the $N_D = 2(N - (N_x + N_y) + 1)$ diagonals.

In the next sections, we will formally introduce the diagonal forces in the system of equations and show some examples that prove the good performance of this approach.

4.2. The semi-rigid body description

The system of Equations (3.1) describes the motion of N point masses sliding over a surface and interacting with each other. We have discussed that interactions induced by imposing the invariance of the inter-mass distance can lead to two kinds of critical conditions, both mathematically expressed by the singularity or quasi-singularity of the coefficients matrix $\boldsymbol{\theta}$. Either the system is overdetermined (hyper-rigidity) or it changes its shape too much. In these cases, the results cannot be computed, or the solution becomes numerically unstable. The additional distance-dependent force acting along the diagonals in quadrilateral-based mass grids ensures mathematical stability and at the same time describes a behavior of rocks that can deform during sliding. The 6-parameter law we adopted can be adapted to describe elastic and plastic behaviors.

By considering the i-th generic point mass in the grid, one may distinguish two kinds of forces acting on it: the side-edge forces induced by the distance invariance, say $\vec{h}$, and the elastoplastic forces, say $\vec{p}$. Adopting a simplified notation, we can write:

$$\sum \vec{h} = -\sum h_P \vec{r}_{iP} + \sum h_N \vec{r}_{iN} + \sum h_P (\vec{r}_{iP} \circ \vec{n}_i)\vec{N}_i - \sum h_N (\vec{r}_{iN} \circ \vec{n}_i)\vec{N}_i \tag{4.1}$$

$$\sum \vec{p} = +\sum p_D \vec{r}_{iD} - \sum p_d \vec{r}_{id} - \sum p_D (\vec{r}_{iD} \circ \vec{n}_i)\vec{N}_i + \sum p_d (\vec{r}_{id} \circ \vec{n}_i)\vec{N}_i \tag{4.2}$$

where in (4.1) we denote with $\vec{r}_{iP}$ and $\vec{r}_{iN}$ the unit vectors along the previous (index smaller than i) and subsequent (index larger than i) side edges connected to the i-th mass, following the quadrangulation order. Thus, h_P and h_N are the interaction forces acting on these edges. Similarly, $\vec{r}_{iD}$ and $\hat{r}_{id}$ denote the unit vectors along the primary and secondary diagonals, related to the i-th

mass. The unit vector $\vec{n}_i$ is normal to the sliding surface, pointing upwards, while $\vec{N}_i = (\vec{n}_i - \mu\, \vec{t}_i)$ is the unit vector $\vec{n}_i$ corrected by the effect of the basal friction (coefficient μ) acting against the velocity $\dot{\vec{r}}_i$. We recall that we denote the number of interaction forces acting along the edges by N_E, and the number of diagonal forces by N_D. Notice that the basal friction has an effect on both classes of forces through the last two terms of Eqs. (4.1) - (4.2). Overall, the force exerted by the mass i on the mass j is equal and opposite to the one exerted by the mass j on the mass i. We can finally write the equations of motion in the compact form:

$$m_i \ddot{\vec{r}}_i = \vec{F}_i + \sum \vec{h} + \sum \vec{p} \tag{4.3}$$

where $\ddot{\vec{r}}_i$ is the mass acceleration vector. $\vec{F}_i$ are the external forces acting on the system, not depending on the 3D distance between the masses. Typically, they are related to the driving gravity force and are, if present, influenced by the basal friction. More specifically, we can write:

$$\vec{F}_i = m_i\, \vec{g} + m_i\, \vec{N}_i\left(\ddot{\vec{r}}_i - \vec{g}\right) \circ \vec{n}_i \quad = -m_i g\vec{k} + m_i \vec{N}_i[(g\vec{k} + \vec{n}_i(\dot{\vec{r}}_i \circ \dot{\vec{r}}_i)/R_i) \circ \vec{n}_i]$$

where $\vec{k}$ is the vertical unit vector and R_i is the local radius of curvature, as already presented in the previous chapters. Even with the addition of the elastoplastic forces in the system, the solving process is preserved. By using the fixed-edge conditions in term of accelerations:

$$(\ddot{\vec{r}}_i - \ddot{\vec{r}}_j) \circ \left(\vec{r}_i - \vec{r}_j\right) = -\left(\dot{\vec{r}}_i - \dot{\vec{r}}_j\right) \circ \left(\dot{\vec{r}}_i - \dot{\vec{r}}_j\right)$$

one gets similar expressions as seen for the quasi-rigid grid:

$$(\vec{F}_i - \vec{F}_j) \circ \left(\vec{r}_i - \vec{r}_j\right) + \frac{1}{m_i}(\sum \vec{h} + \sum \vec{p}) \circ \left(\vec{r}_i - \vec{r}_j\right) = -\left(\dot{\vec{r}}_i - \dot{\vec{r}}_j\right) \circ \left(\dot{\vec{r}}_i - \dot{\vec{r}}_j\right) \tag{4.4}$$

Also, in this case, the previous equations can be written in a compact form to calculate the system side-edge forces:

$$\boldsymbol{h} = \boldsymbol{\Theta}^{-1}\boldsymbol{a}$$

where $\boldsymbol{h}^T = [h_1; h_2 \ldots; h_{N_E}]$, $\boldsymbol{\Theta}$ is an $N_E\ x\ N_E$ coefficients matrix derived from Eq. (4.4), and $\boldsymbol{a}$ is the N_E −vector containing all the terms in Eq. (4.4) that depend on the velocities and positions of the point masses, including the elastoplastic forces.

4.3. Semi-rigid body examples

In this section, we will show some simple-geometry examples to highlight the main characteristics of the semi-rigid body description. Let us consider again an elliptic paraboloid in a (x, y, z) Cartesian reference system, described by the function:

$$z = ax^2 + by^2$$

with $a = 2 \cdot 10^{-5} m^{-1}, b = 4 \cdot 10^{-5} m^{-1}$. The surface is built over a $(4x4)\ km^2$ area centered in the axis origin. In all the examples, the system CoM is set in $P_c = (-1000;\ +1200;\ +82)m$. Notice that we use the same basic geometry to highlight differences and similarities among the various models

It is relevant to observe that in the following examples the energy of the system is not fully conserved. Indeed, the elastoplastic forces do work on the system. Formally they play the role of additional forces adding their contribution to the external forces. For the sake of brevity, we will omit all graphs concerning the distance errors for the side edges since distances are all well conserved. Also, energy plots will be omitted. Table 4.1 summarizes the main features of the 5 cases treated in this section.

Case	Number of point masses N	Number of quadrilaterals N_Q	Number of side edges N_E	Number of diagonal forces N_D	$m(kg)$	Simulation time $t(s)$	Friction coefficient μ
A3	4	1	4	2	100	800	0
B3	5	4	12	8	100	800	0
C3	21	12	32	24	100	800	0
D3	121	100	220	200	2-500 symmetric	300	0.02
E3	121	100	220	200	2-500 random	150	0.08

Table 4.1 Characteristics of simulations A3-E3 performed with the model UBO-Inter. All symbols in the Table heading are given in the text, with the exception of N_Q, that denotes the number of quadrilaterals.

In the simulation A3, we set 4 point masses on a $500\ m$-side rectangle. In the case B3, we add one internal mass in the system CoM, dividing the same structure in 4 equal quadrangles. In Figure 4.1 we show the computed trajectories of the CoM of the 4-mass (A3) and 5-mass (B3) systems. As we may expect, they are quite similar to the other frictionless cases illustrated before. These examples are useful as a reference since we will show that further subdivisions of the same basic structure do not affect the general system dynamics.

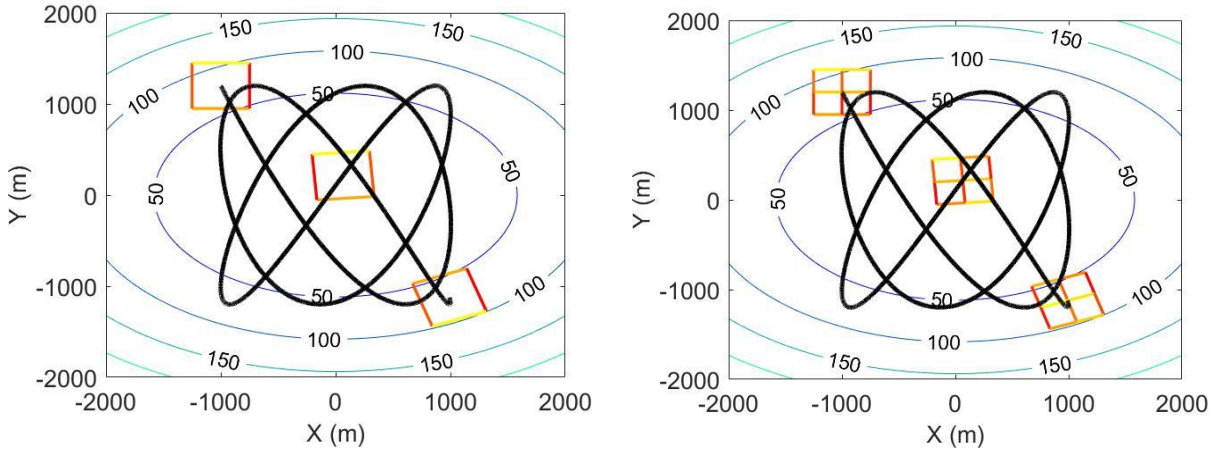

Figure 4.1 CoM trajectories for simulations A3 (left panel) and B3 (right panel). The magnitude of the side-edge forces is denoted by colours ranging from yellow to red, at $t = [0;\ 400;\ 800]$ s. Notice that the general dynamics is the same, despite the different pattern of the internal forces and the different total mass of the systems.

The general behaviour of the side-edge forces (upper right and left panels in Figure 4.2) is quite similar for the two cases. Notice that these forces basically split into two classes of magnitude (one twice larger than the other), both with a slightly oscillating pattern. Oscillations are induced by the

elastoplastic forces (see the bottom panels in Figure 4.2). These forces are an order of magnitude smaller than the side-edge forces and clearly increase during the motion. Notice further that the largest side-edge forces tend to weaken. It is worth observing that in case B3 the forces along the external edges are not the strongest ones as we have seen in the previous rigid-grid examples.

The velocity plots for both simulations are the same, and all the masses move as the system CoM (Figure 4.3). This means that deformation of the A3 and B3 structures is negligible and that the elastoplastic forces act in a regime where the relative lengthening (w) of the diagonals is close to zero.

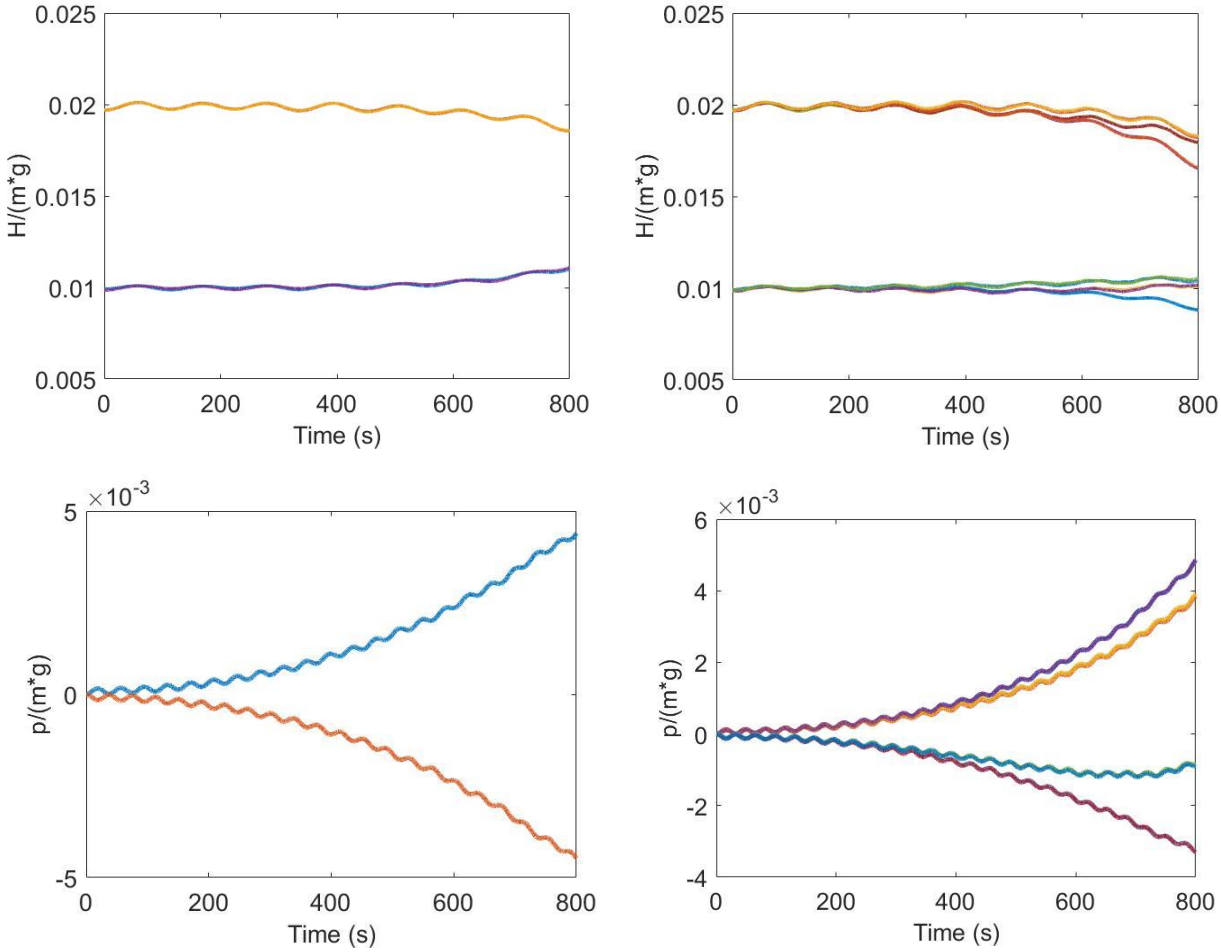

Figure 4.2 Internal forces for simulations A3 (left side) and B3 (right side). The interaction forces along the side edges are shown in the upper panels, the elastoplastic forces (along the diagonals) in the bottom ones. Notice that the oscillating nature of the elastoplastic forces affects the behaviours of the along-edge forces. Notice further that the latter tend to predominate over the former ones.

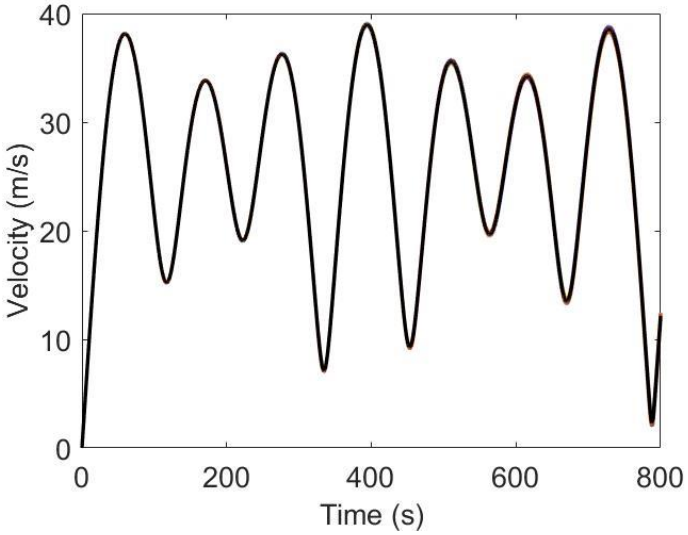

Figure 4.3 Velocities of the point masses and CoM for cases A3 and B3. Notice that all masses move together with the CoM and the related curves overlap perfectly.

Let us now introduce a more interesting case where the elastoplastic forces play a more important role. In the case C3 we present the same basic structure described in the simulations D2-F2, but with the elastoplastic forces acting on each internal diagonal edge. The CoM trajectory and the velocity plots are very similar to the previous cases (Figure 4.4). The individual mass velocities differ from the one of the CoM in the central part of the simulation, reflecting the effect of the distance-dependent forces on the system. Like in the case F2, the side-edge forces and, here, also the elastoplastic forces, go to zero around $t = 380\ s$ (Figure 4.5). In this particular instant, the elastoplastic forces change sign reciprocally (right panel of Figure 4.5). We observe that the interaction forces are much stronger than the elastoplastic ones. This reflects in the fact that deformation is allowed, but it is not the dominant feature. In other words, the particular parameter setting of the elastoplastic function *k(w)* we have adopted in these examples ensures some level of deformation. What is relevant is that the introduction of such forces handled by the UBO-Inter model removes both kinds of singularities seen in the examples D2 and E2 the previoofus chapter.

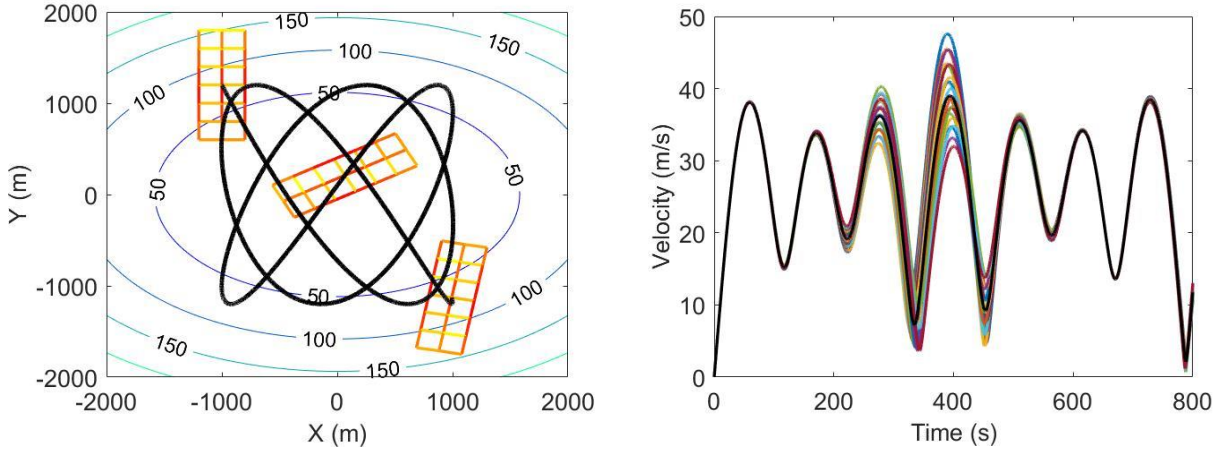

Figure 4.4 Left panel: CoM trajectory for simulation C3. The magnitude of the side-edge forces is denoted with a color code, ranging from yellow to red, at $t = [0;\ 400;\ 800]$ s. Right panel: Point mass velocities and CoM velocity (black line).

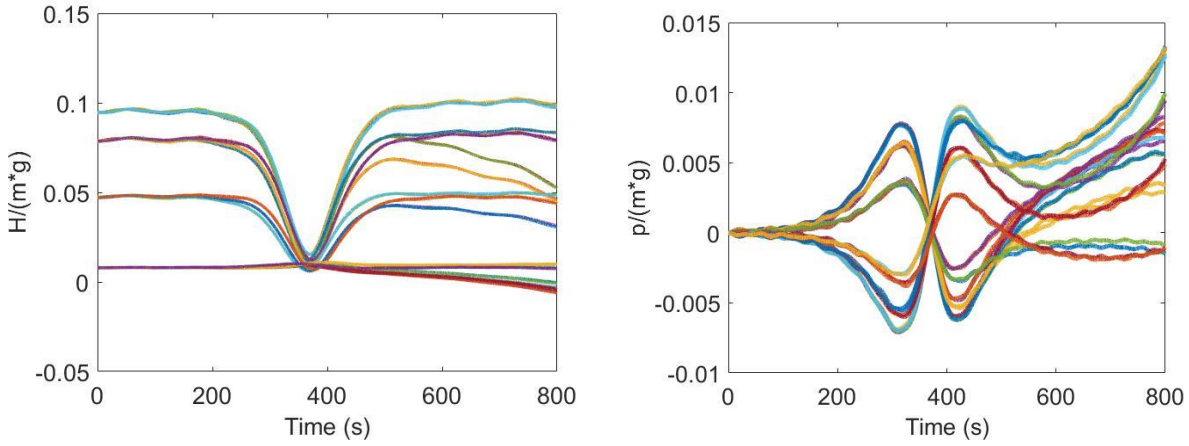

Figure 4.5 Plots of the inner forces in simulation C3. Side-edge forces (left panel) and elastoplastic forces (right panel) are normalized over the mean gravity force acting on the system. Notice that elastoplastic forces are one order of magnitude less than the others.

The last examples we will treat in this section show the application of the code UBO-Inter to systems with a larger number of masses sliding down analytical surfaces. This is done because before proceeding to real-topography cases, it is essential to test the model UBO-Inter on larger grids with irregular mass distributions and under the effect of the friction forces. To this purpose, let us consider an $11x11$ 75 m-spaced mass grid. The masses are symmetrically distributed around the CoM of the system (that remains in the geometrical center of the configuration), with values ranging between 2 and 500 kg. As we can see in Figure 4.6 (left panel) the system trajectory is equal to that computed for the case C2, since expectedly the general dynamics is preserved if the CoM of the systems are set in the same initial position with the same (zero) initial velocity. The velocity plots as well (right panel in Figure 4.6) show a behavior similar to that of the case C2, with a maximum in the order of 30 m/s. The side-edge forces (left panel of Figure 4.7) are distributed between 1 and 13 % of the mean gravity force, while the elastoplastic forces (right panel of Figure 4.7) present a quite complicated oscillatory pattern and are spread over a $\pm$ 3% $\bar{m}g$ range. Hence, even in this case, they tend to be smaller than the former ones. Practically, the whole motion of the system can be reduced to that of the CoM due to the selected distribution of the point masses. In the next example, we will see that this is not the case when we consider randomly distributed masses.

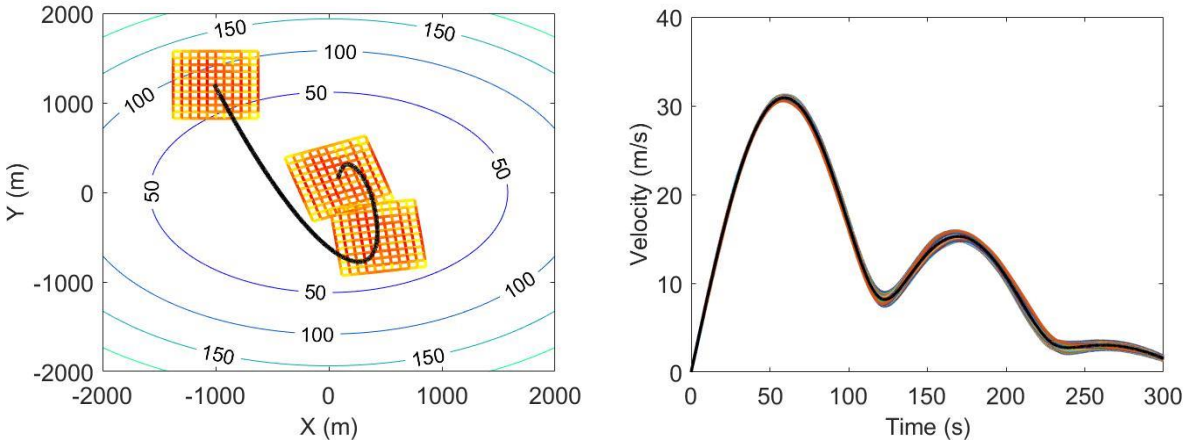

Figure 4.6 CoM trajectory for simulation D3 (left panel). The magnitude of the side-edge forces is denoted with a color code, ranging from yellow to red, at the instants $t = [0; 150; 300]$ s. In the right panel, the velocities of all point masses and of the CoM (black line) are shown together. All velocities tend to zero due to the effect of friction.

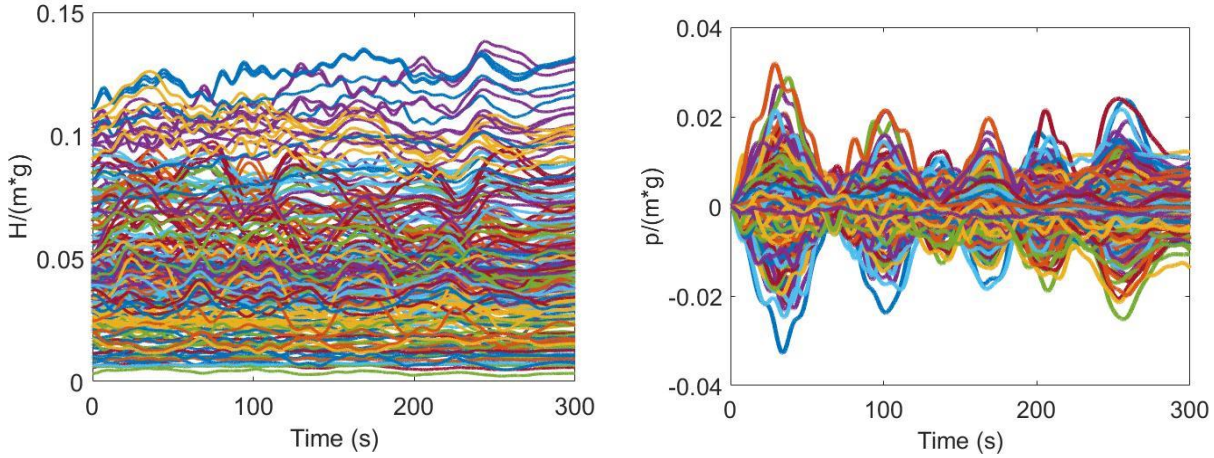

Figure 4.7 Internal forces in simulation D3. Side-edge forces (left panel) and elastoplastic forces (right panel) are normalized over the mean gravity force acting on the system. Notice that the behavior of these forces is more complicated here than in cases of grids with a low number of point masses.

For the last example of this section, let us consider a different sliding surface, represented by an inclined paraboloid in the $y-$ direction, that can be seen as a valley:

$$z = cx^2 + dy$$

with $c = 10^{-4}\ m^{-1}$ and $d = 0.05$. Let us consider the same mesh as in the last simulation but with a different mass distribution. We set the larger masses (between $100\ kg$ and $500\ kg$) in the y-direction in the uphill half of the structure. In the downhill part, the masses are set between $1\ kg$ and $50\ kg$. In this case, the body slides along the axis of the valley (y-direction) while oscillating transversally along the x-axis. The motion is slowed down by friction. As we can see in Figure 4.9, the plot of the side-edge forces is different from the previous cases and reflects the different slope topography and the different mass distribution. The strongest forces are the ones closest to the CoM of the system (see Figure 4.8, left panel). The CoM reaches a velocity peak in the order of $28\ m/s$. In this case, the velocities of the individual point masses differ from one another quite a lot, especially in the last phase of the motion (see right panel in Figure 4.8), which means that the system deforms considerably. Further, the elastoplastic forces tend to differ from one another especially in the second half of the motion, with some irregular increasing trends (Figure 4.9). Notice that all these forces are stronger than in the other cases. More precisely, the elastoplastic forces are comparable in magnitude with the side-edge forces. Despite the simple geometry, this is the example that represents best the motion of a real slide. As we will show in the next Chapter in real cases the elastoplastic forces reach considerable values, comparable with the gravity force. When the mass distribution and the bathymetry are irregular, the elastoplastic forces have to be strong since they permit the body to deform, but they inhibit extreme deformations allowing the body to remain intact. The examples presented in these sections are useful to understand the basic features of the model UBO-Inter, but other features will become apparent only when we will handle point-mass systems moving on real irregular topographies.

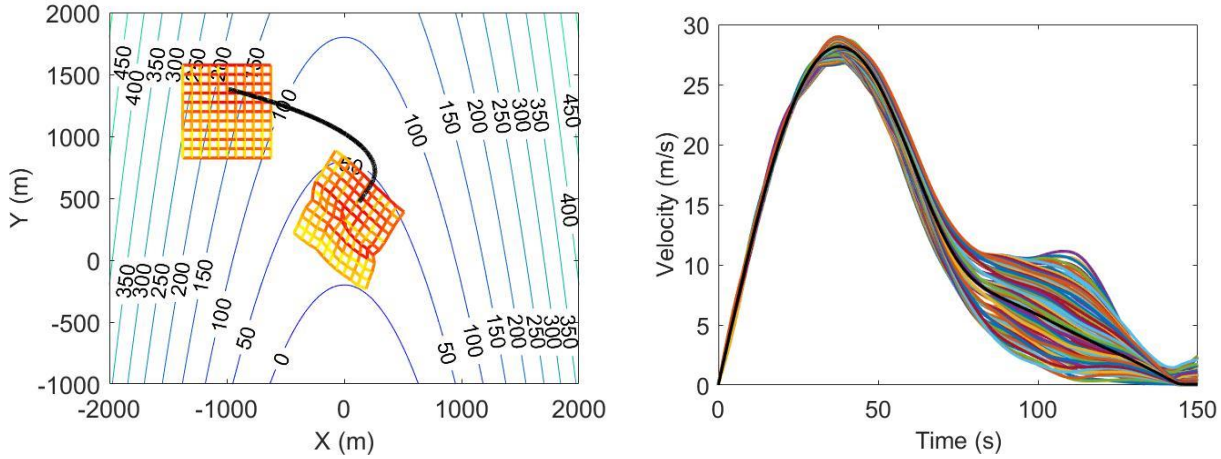

Figure 4.8 CoM trajectory for simulation E3 (left panel). The side-edge forces magnitude is denoted with a color code, ranging from yellow to red, at the initial and final instants, i.e. $t = [0;\ 150]$ s. In the right panel, the velocities of the point masses are shown. The black line denotes the CoM velocity.

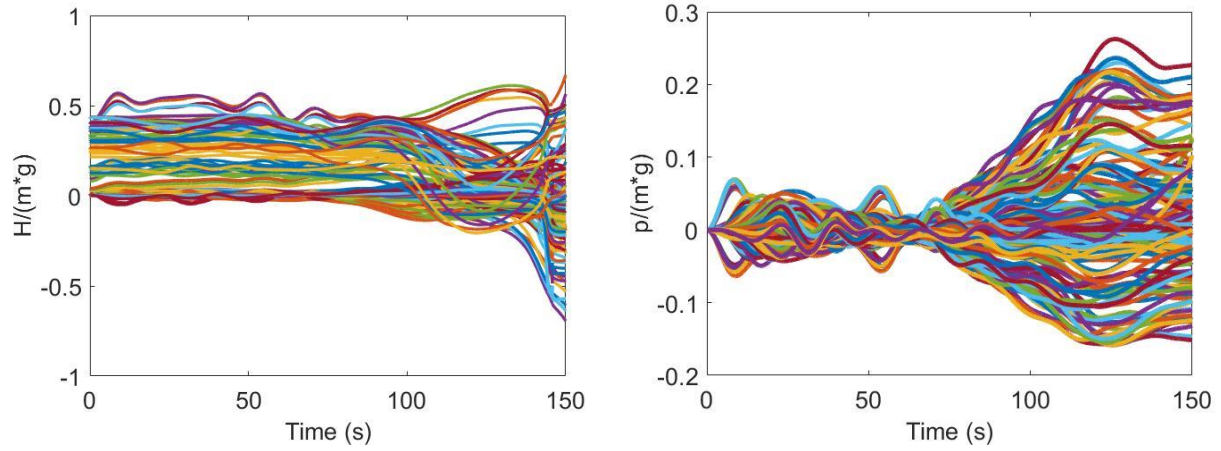

Figure 4.9 Internal forces in simulation E3. Side-edge forces (left panel) and elastoplastic forces (right panel) are normalized over the mean gravity force acting on the system. Notice that the magnitudes of these forces are stronger than in the previous cases, due to the irregularity of the mass distribution. Notice further that the two classes of forces are of the same order of magnitude.

Chapter 5

5. Real topographies

5.1. Interpolation process

In the previous chapters, we have shown a series of simple-geometry cases where the body was assumed to slide on an analytical surface, and thus the values of all the surface derivatives determining the external and inner forces were exactly known in every point of the surface grid. In what follows, we will extend the simulations to real topographies, since this will allow us to apply the model to realistic scenarios. Thus, it is necessary to address the problem of how we can describe real topographies and how we can formally solve the equations of motion over these surfaces.

Generally speaking, usually real topographies are given by means of discretized grids where each node represents a specific altitude. Examples are the so-called DEMs (Digital Elevation Models) that provide useful representations of a terrain's surface. In order to solve the equations of motion for a landslide, we need the first- and second-order derivatives of the surface. Such derivatives must be evaluated through discrete operators like the following ones:

$$\delta_+ z_{m,n} = \frac{z_{m+1,n} - z_{m,n}}{\Delta x} \qquad \delta^+ z_{m,n} = \frac{z_{m,n+1} - z_{m,n}}{\Delta y}$$

$$\delta_- z_{m,n} = \frac{z_{m,n} - z_{m-1,n}}{\Delta x} \qquad \delta^- z_{m,n} = \frac{z_{m,n} - z_{m,n-1}}{\Delta y}$$

$$f_x(x_m, y_n) = \frac{1}{2}(\delta_+ + \delta_-) z_{m,n} \qquad f_y(x_m, y_n) = \frac{1}{2}(\delta^+ + \delta^-) z_{m,n}$$

$$f_{xx}(x_m, y_n) = \delta_+ \delta_- z_{m,n} \qquad f_{yy}(x_m, y_n) = \delta^+ \delta^- z_{m,n}$$

$$f_{xy}(x_m, y_n) = \frac{1}{4}(\delta^+ \delta_+ + \delta^+ \delta_- + \delta^- \delta_+ + \delta^- \delta_-) z_{m,n}$$

Here $z_{m,n} = f(x_m, y_n)$ represents the altitude of the specific node (m,n) of the grid, and Δx and Δy are the space steps in the x and y directions. The above discrete operators allow us to compute all the required derivatives in the grid nodes. But point-mass trajectories do not pass necessarily over grid nodes, which implies that an interpolation algorithm has to be implemented to recover the derivatives at a generic point of a point-mass trajectory. The interpolation process must be selected with attention. The Runge-Kutta numerical schemes compute the solutions of a generic ODE by means of temporal sub-steps, where the values are evaluated but not saved. This means that the space derivatives of

every point-mass must be known not only at any time step, but also at each sub-step. However, performing the interpolation process over an entire grid for every point-mass, and at anyone of the time sub-steps, requires a lot of computational effort. The first tests on the code running-time proved that this solution was computationally too heavy, even for cases of less than 10 point masses.

To understand the algorithm we used to solve this aspect, let us consider a generic position over the surface $f(x_m, y_n)$, as is shown in Figure 5.1. The grid space steps are denoted as Δx and Δy. As we can see from the sketch, the generic positions assumed by the mass does not necessarily coincide with the grid nodes, that in the figure are the intersections of the dashed black lines.

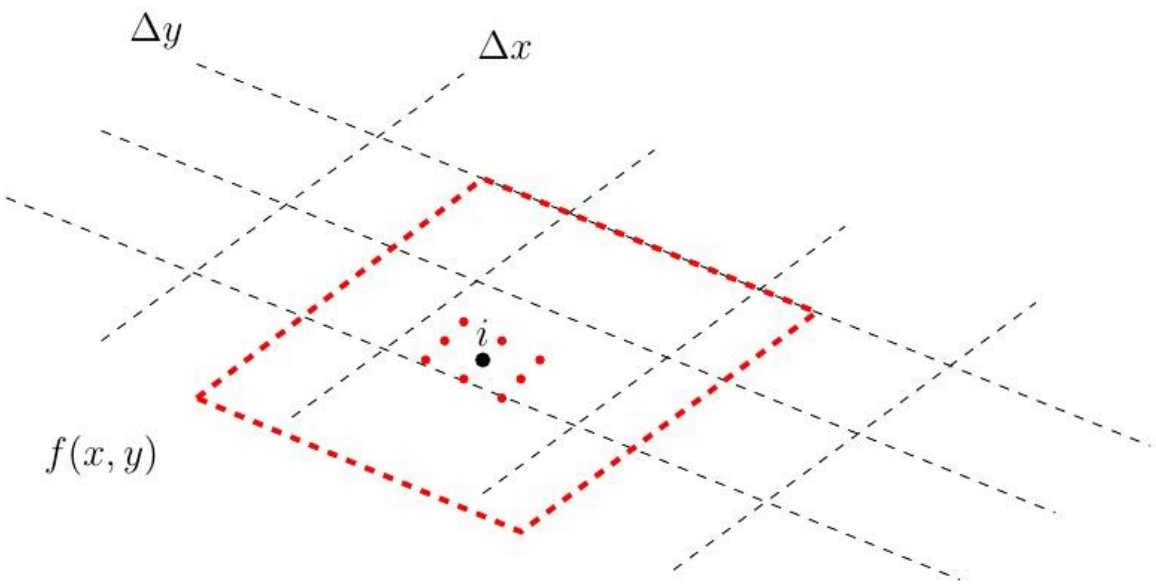

Figure 5.1 The generic position of the mass i over the discrete surface $z_{m,n} = f(x_m, y_n)$ is shown with the black circle. The local zoomed surface (enclosed by the red dashed line) is dynamically defined and used to compute the horizontal position (x_i, y_i) as well as the corresponding altitude z_i and all the needed derivatives, i.e. $f_x(x_i, y_i)$, $f_y(x_i, y_i)$, $f_{xx}(x_i, y_i)$, $f_{yy}(x_i, y_i)$ and $f_{xy}(x_i, y_i)$ by means of a spline interpolation algorithm.

The basic idea is to compute interpolations over a local sub-grid covering an area around the instantaneous position of the mass *i*, as is shown in Figure 5.1 (area bounded by the red dashed line). This zoomed surface must have a size that is adequate to capture the main features of the real topography considered. The size of the space sub-grid, that is the amount of grid nodes around the query point is properly evaluated and can be changed anytime during the simulation. Once the sub-grid is defined, a spline interpolator is used to compute the elevation of the surface $z_i$in the position *i* (black solid circle in Figure 5.1), as well as in 8 more neighbour points lying on the edges of a rectangle centered on the position *i* with size in the order of $\Delta x/10^4$ and $\Delta y/10^4$(red solid circles in Figure 5.1). This is equivalent to build a very high-resolution 9-node grid in the neighbourhood of the position of interest. The application of the discrete operators defined above on such a grid provides the values of the needed derivatives. Thus, by calling a single interpolation process, we are able to compute all the derivatives in a consistent way.

5.2. The Scilla 1783 landslide

Let us now introduce the first real-like case. The 1783 Scilla rock avalanche detached from Mt. Pacì after the occurrence of one of the main shocks of the "Terremoto delle Calabrie" seismic sequence. Some 20 minutes after the earthquake, the landslide triggered tsunami waves that hit the close beach of Marina Grande. As was mentioned in the first Chapter of this thesis (Section 1.6), this slide has been the object of previous studies, and one of the results of them is the identification of the initial detachment niche and of the final deposit [*Bosman et al*., 2006; *Mazzanti and Bozzano*, 2011; *Bozzano et al.*, 2011]. Hence, this case represents a useful example to validate the model UBO-Inter. For the sake of completeness, we will compare the UBO-Inter results not only with the observations but also with the results obtained by means of the model UBO-Block (1D version), that is a model validated through laboratory data and applications to several cases in the literature (for a description see Section 2.3 and references therein). It was noted that the 1D version of the model UBO-Block needs the trajectory of the blocks CoM to be specified in the input data. This means that the landslide body follows a predefined trajectory that is established mainly by means of considerations based on the geomorphology of the area. On the contrary, this is not the case for the model UBO-Inter since it computes the trajectory of all the point masses and of the CoM of the entire landslide.

For both simulations, the Mt. Pacì flank and the surrounding area are represented by a $10\ m\ x\ 10\ m$ grid, covering an area of $4.5\ x\ 4.5\ km^2$ (Figure 5.2). In the UBO-Inter simulation, the original surface is smoothed with a moving average filter, to avoid local strong topography gradients that could affect the model results. Indeed, when the average distance between the interacting mass pairs is of the same space scale of the main topography features, then the model may run into inaccuracies, that smoothing is able to avoid or to mitigate. The original topo-bathymetric grid is obtained through interpolation to get the required resolution, from the SRTM database for land morphology, and from the GEBCO database and selected charts published by the IIM (Istituto Idrografico Militare, the Italian Navy hydrographic institute) for the coastal and offshore bathymetry. As underlined in Section 1.6, the final deposit is smaller than the total reconstructed landslide volume, suggesting that the missing mass was removed by different erosion processes. In the UBO-Block simulation, the landslide thickness ranges from 2 to $100\ m$ (Figure 5.3). In the model UBO-Inter where masses are considered dimensionless points, the thickness of the slide body is accounted for in terms of mass distribution: larger masses correspond to areas where the slide is thicker, provided that the constraint of the total slide mass is respected. We assume that the rock density is uniform, more precisely $\rho_r = 2000 \frac{kg}{m^3}$, and that the total volume is $V = 6.4 * 10^6\ m^3$. In the UBO-Block simulation, the sliding body is portioned into 10 blocks. In Figure 5.3 the landslide trajectory is shown, together with the initial and final deposit area and related thickness. Notice that the slide widely spreads in the underwater part of the motion, resulting in a thinner deposit. We do not expect this kind of spreading in the UBO-Inter results since the mass grid does not have the ability for large deformations. The UBO-Block velocity graphs for the blocks and for the slide's CoM are shown in Figure 5.4. The blocks interact with water after $15\ s$ reaching velocity peaks about $32\ m/s$. Subsequently, the drag forces rule the motion, sliding down the blocks considerably. In the model UBO-Block, the drag forces are applied on the blocks faces that impact the water directly.

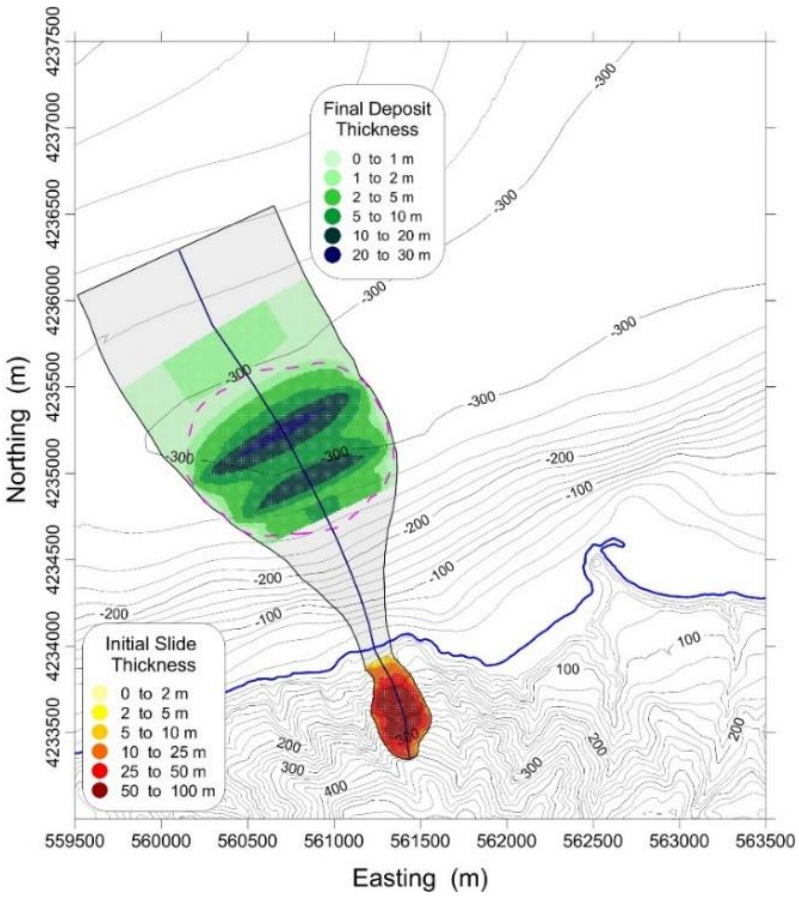

Figure 5.2 Trajectory of the Scilla slide used by the model UBO-Block. The initial sliding area is colored in red. The green area is the final deposit. Darker colours denote thicker layers. The coastline is denoted with the blue line. The CoM trajectory (black line) is a model input. Altitudes range from 400 m a.s.l. to 350 m b.s.l.

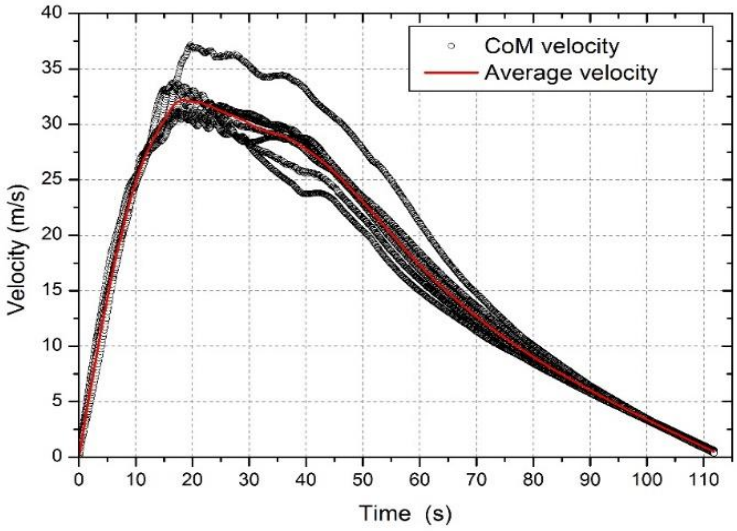

Figure 5.3 Velocity curves from the model UBO-Block. The blocks interact with water between 15 and 20 s, reaching the velocity peaks. In the underwater part of the motion, they slow down under the effect of the drag forces.

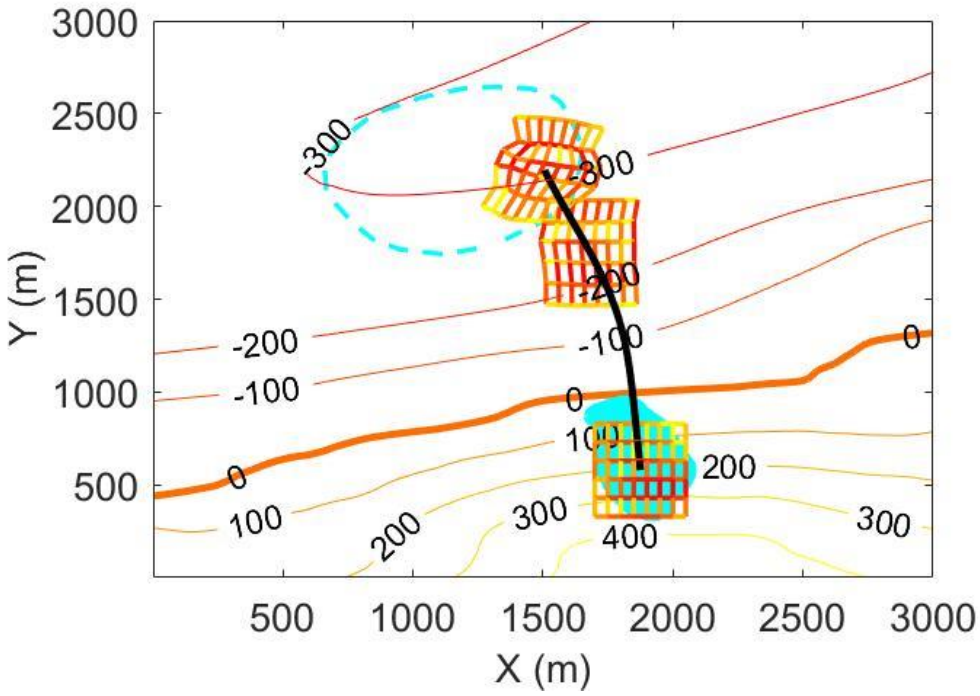

Figure 5.4 Smoothed topo-bathymetry of the Scilla area. Altitude values are given in meters. The landslide CoM trajectory computed through the code UBO-Inter is shown with the black line. The initial area is colored in cyan, while the cyan dashed line delimits the observed final deposit. The 48 point mass system has a CoM coinciding with the CoM of the landslide as assumed at the initial time in the model UBO-Block.

In the model UBO-Inter, the landslide body is represented by N point masses at the vertices of quadrilaterals. The masses of such points are determined in function of the initial slide thickness, that range from 2 m in the lower part, to 100 m in the central part. With the present version of the model UBO-Inter, the effect of the drag exerted by the water can be considered only in terms of an effective basal friction coefficient. To this purpose, when the masses associated with a thickness exceeding 5 m are underwater we consider the following friction coefficient:

$$\mu_{eff} = \mu_w + 0.5 \frac{\rho_r}{\rho_w} \frac{C_d}{g\, l_v} v^2$$

where $\mu_w = 0.09$ is the basal friction coefficient in wet conditions, $\rho_r = 2000 \frac{kg}{m^3}$ is the rock density, $\rho_w = 1030 \frac{kg}{m^3}$ is the sea water density, $C_d = 1.05$ is the drag coefficient related to a hypothetical cubic block, l_v is the length of the block edge in the motion direction and v is the relative velocity of the water with respect to the block. This latter, assuming that the slide moves in a still water sea, practically equals the velocity of the block. Notice that in the above formula l_v is not the length of the edges connecting the point masses, but it is the side length of the hypothetical blocks whose CoMs are represented by the point masses and is a parameter that can be adapted to fit observational or reference-case data, when available. For all simulations we ran for the Scilla rockslide we assumed the value $l_v = 50\, m$. When the point masses slide on the onshore slope (i.e. when their altitude $z > 0$) we set $\mu_{eff} = \mu_r = 0.23$, that represents the friction coefficient in dry conditions. This approach allows us to estimate the effect of the drag forces in terms of a correction of the friction coefficient,

and we adopt it since it proves to give satisfactory results. Nevertheless, further studies are required to explore the limits and general applications of this correction.

We will set regular mass-grids covering the initial sliding area, centred over the slide CoM. Pointedly, we will prove that the number of point masses N considered to represent the landslide body does not change the dynamics of the system, while it slightly affects the pattern of the inner forces. We first present a larger grid formed by $N = 48$ masses and covering an initial area of $1.75\ 10^5 m^2$. Secondly, we select a series of grids centered over the thicker part of the slide. In these cases, the grids are formed by: $N = 4, 9, 16, 35, 56$. In Figure 5.4 we show the trajectory computed for the system consisting of $N = 48$ point masses, set in a 8 x 6 matrix: 8 rows in the x direction, that is approximately transverse to the slope, and 6 columns in the y direction (that is approximately downslope), equally spaced by $50\ m$ and $100\ m$, respectively. In this case, one counts $N_E = 82$ side edges and $N_D = 70$ diagonal edges. The $N = 48$ grid is run until $t = 100\ s$ with a time step $dt = 0.075\ s$. The body structure is shown at $t = [0, 50, 100]\ s$. Notice that the initial shape is partially lost during the motion, resulting in a final shortening in the y-direction. Initially, the distribution of the side-edge forces is mainly related to the different altitude of the masses. In the final position, the masses located close to the CoM are characterized by stronger interactions. Looking at Figure 5.4, a small eastward drift and a slight clockwise rotation can be observed to occur during the motion. This peculiar movement results from the different local slope gradients and from the heterogeneous effect of the drag forces. The system final position is located in the eastern part of the observed deposit. However, the UBO-Block pre-imposed trajectory and the path computed through the model UBO-Inter do match reasonably, if one considers that the slide motions are calculated over slightly different basal surfaces (more smoothed for UBO-Inter), which may have some effect on the outputs. Velocity and internal force curves for the 48-mass system are shown in the left and right panel of Figure 5.5, respectively. The elastoplastic forces are shown by thicker lines. The front part of the sliding body enters the sea water after $15\ s$ from the slide initiation, and in correspondence of this time, one observes a strong decrease of the mass speeds. Observe further that the point masses move coherently like in a compact body, so the velocity plots for all masses are similar to the one of the slide CoM. Moreover, notice that this behavior is clear in all the other simulations where the grid is set on the slide's thicker part (see Figure 5.7), no matter the number of masses that form the sliding body, with one exception. The point-mass velocities differ noticeably from the one of the CoM when the number of masses is very small (N=4). In this case, indeed, the masses can easily move one with respect to the other. This mutual motion is more inhibited when the number of masses increases. In all the cases, the effect of the drag forces strongly decelerates the masses.

The internal forces (right panel in Figure 5.5) show the first maximum at $t = 15\ s$, denoting the interaction with water. At this stage, the internal forces reach values comparable with the gravity force. We do expect such high values since inner forces have to contrast the action of the drag and of the basal friction forces that would normally tend to cause the system to shrink in the direction of motion.

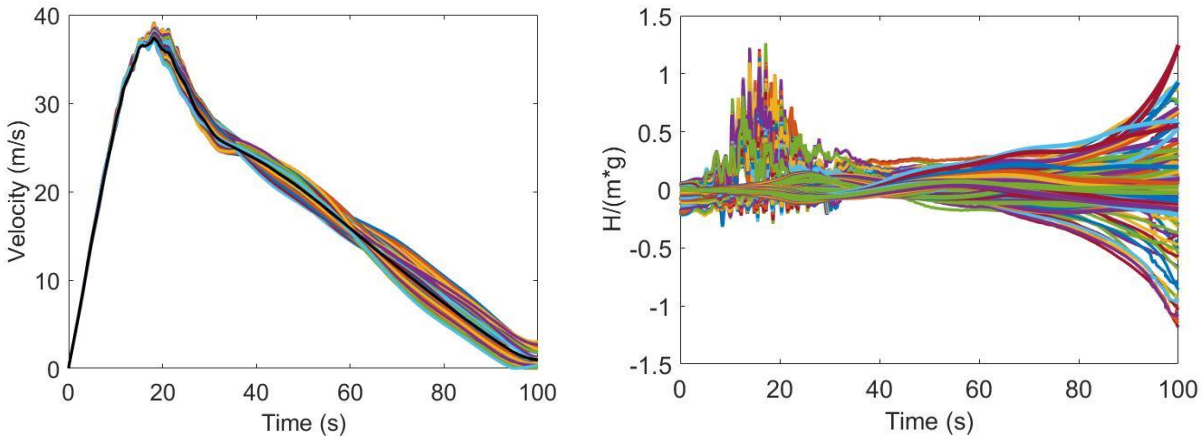

Figure 5.5 Results for the $N = 48$ point-mass system. On the left, velocity curves are shown. The velocity of the CoM is denoted with the black line. On the right, inner forces are plotted. Thicker lines represent elastoplastic forces acting on the diagonal edges. Thinner lines represent the forces acting on the side edges. Notice the strong bumps around $t = 15\ s$, when masses enter the sea water.

Such effect is similar in all the simulations, where the slide stops some $10\ s$ later with respect to the previous case. The trajectory of the $N = 35$ point masses is shown in Figure 5.6, where the structure is shown at $t = [0, 55, 110]\ s$. In this case, the grid is smaller and equally spaced by $50\ m$ in the x- and y-direction. Nevertheless, we can notice that the direction of motion and final deposit do not change considerably. The other systems formed by $N = 4, 9, 16, 56$ point-masses cover the same initial area but with different mass positions. We do not show all the single trajectory results since they are all similar. Velocities and internal forces for all the selected systems are shown in Figures 5.7 and 5.8, respectively. It is worth observing that in the 35- and 56-mass systems, the inner forces tend to increase in magnitude as the body advances in the water, which does not occur in the other cases. Such behavior could be related to the enhanced need of strong bounds to keep the structure semi-rigid. Indeed, the masses would normally tend to spread and to deposit in the final stage while their velocities are going to zero. The internal forces contrast such a spreading and some of them tend to increase. More simulations have been tested with N up to 200, confirming the increase of the inner force magnitude close to the end of the slide motion, and all the other features illustrated before.

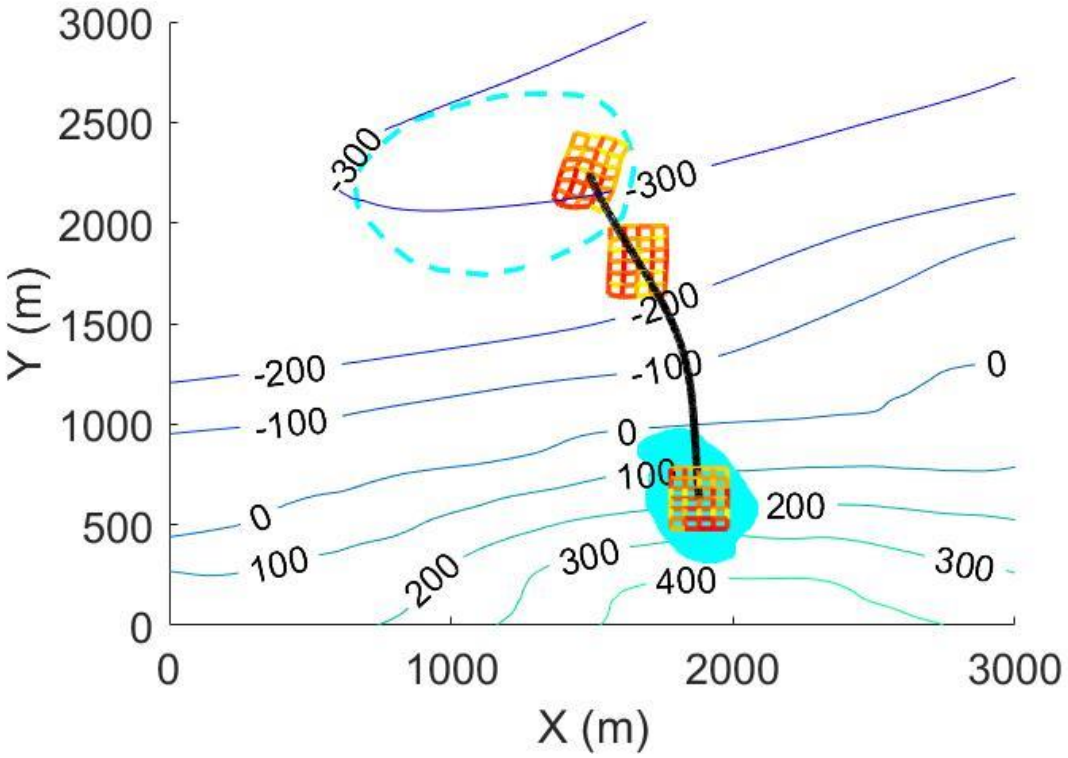

Figure 5.6 Case with N=35. Smoothed topo-bathymetry of the Scilla area. Altitude values are given in meters. The landslide CoM trajectory computed through the model UBO-Inter is shown with the black line. The initial area is colored in cyan, while the cyan dashed line delimits the observed final deposit. The 35 point-masses are set in the thicker part of the initial sliding area.

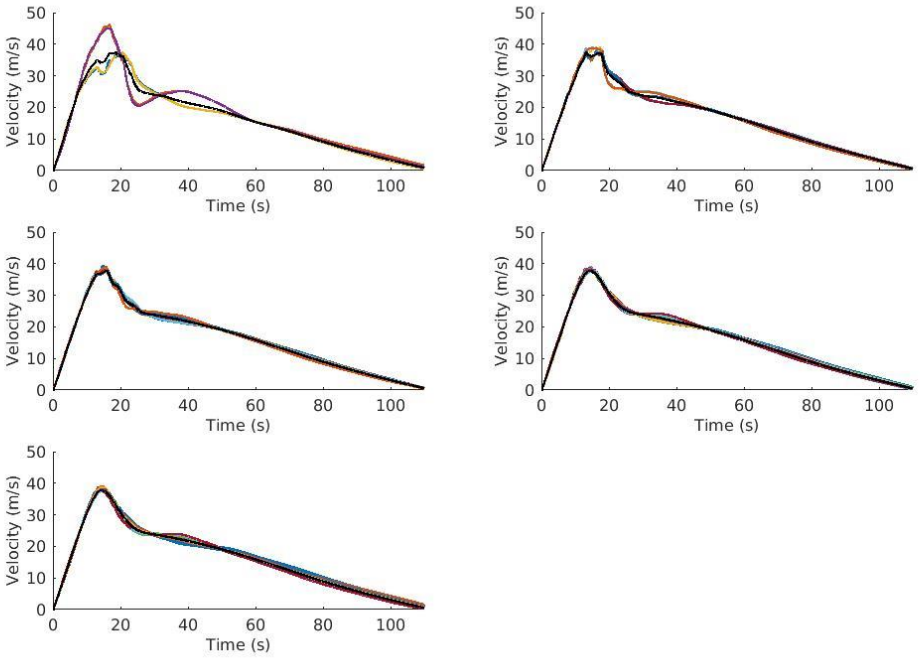

Figure 5.7 Point-mass velocities for different systems formed of N = 4 (upper left), 9 (upper right), 16 (central left), 35 (central right) and 56 (bottom) point masses. Notice that in these cases the mass grid is smaller and set on the thicker part of the slide. In each graph, the black thick line represents the system CoM.

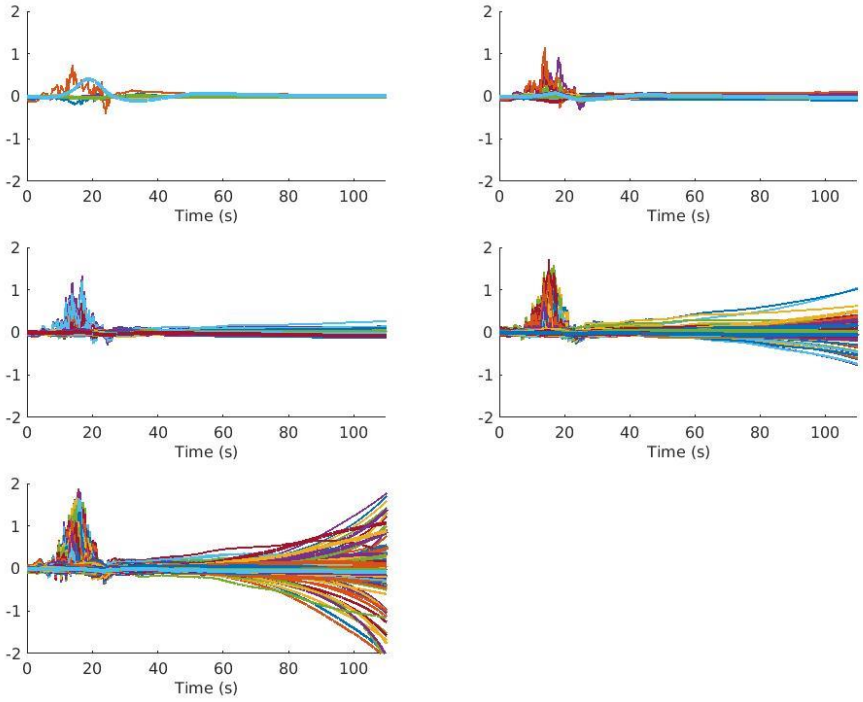

Figure 5.9 Inner forces normalized over the mean gravity force. The graphs refer to systems with *N*= 4 (upper left), 9 (upper right), 16 (central left), 35 (central right) and 56 (bottom) point masses. The thicker lines represent the elastoplastic forces acting on the diagonal edges. The thinner lines denote the forces acting on the side edges.

5.3. Scenarios of Marsili Volcano collapses

In this section, we will present a series of mass failures occurring over the flank of the submarine volcano Marsili. The volcano is located in the southern part of the Tyrrhenian Sea, about 120 km north of Sicily and 370 km west of Calabria. The dome is 70 km long, 30 km wide and reaches a peak of 3 km corresponding to a depth of only 450 m b.s.l. (Figure 5.9). As was introduced in Section 1.7, recent studies have proven that the volcano is still active and has erupted in historical times. Marsili eruptions may represent a direct threat, though the volcanic vents are deep and far from the coastlines. What is of interest here, however, is that a strong eruption or seismic activity in connection with volcanic eruptions could trigger mass movements that could in turn induce tsunami waves. The lack of evidences and deposits do not allow us to clearly depict the magnitude and characteristics of such slides. The structure is located over a basin as deep as 3500 m. Thus, it is expected that deposits of relatively small slides are hard to detect due to erosion processes. Furthermore, one should notice that deep underwater movements require huge sliding volumes to trigger noticeable tsunami waves. The purpose of this study is not focused on tsunami generation or propagation, but only on mass movements, though we will depict potential scenarios that have also an interest in terms of natural hazards. In what follows we will hypothesize a number of slides, on the basis of the general geological setting and the seamount topographical features. The slides will differ as regards volumes and positions in the volcano flanks and will be simulated by means of both models UBO-Block (2D version) and UBO-Inter. These simulations can be seen also as a test for the model UBO-Inter and can be relevant for potential tsunami generation that can be addressed in future studies. It is worth

pointing out that this is the first study that depicts different collapses over the Marsili volcano, so comparisons with results obtained by other authors cannot be made. For every simulation, we reconstruct the potential sliding volume, and use first the model UBO-Block and then the model UBO-Inter. Eventually, we make comparisons in terms of slide velocity and trajectories and show and discuss the internal forces computed by the model UBO-Inter.

As is clear from Figure 5.9, the volcano structure presents an elongated shape in the S-N direction. Thus, the most relevant, and in this case also the steepest, flanks are the ones facing east and west. We will focus our attention on the eastern flank, that shows some, though poor, evidences of past movements. Furthermore, it is the closest to the Italian coastline and collapses in this sector are potentially more dangerous. More precisely, slope angles in these areas range from $15°$ in the deeper parts, to $40°$ in the summit areas. Further, the density of the upper structures is lower. Here one may find cones and low-density unstable rocks, fed by the underlying shallow magma chamber. This aspect suggests us that very-small-volume movements that have an origin in the summit part of the volcano have little chance to reach significant distances. For very small volumes we mean here volumes less than 0.01 % of the actual size of the eastern sector of the volcano. This latter volume cannot be defined uniquely, but morphological considerations help us estimate a value of about $1000\ km^3$, taking into account the medium height of the dome and excluding the low-density part, located in the summit area. The only deposit detected so far is probably related to a small-size movement and can be found in the northeastern sector of the volcano, about $2700\ m$ b.s.l.. Some $200\ m$-side blocks have been seen in this sector at a depth of $1200 - 1800\ m$. Thus, we select this area to be the proper location of a small-size slide (see the black area on the left panel and the upper cross-section in the left panel of Figure 5.10). This is the only simulation that is related to an evidence that suggests a past movement occurrence. The selected slide volume in this case is about $40\ Mm^3$ and this slide belongs to the rock avalanche type.

The second simulated slide represents a different kind of movement and is located in the northernmost part of the volcano (see the blue area on the left panel and the second cross-section in the left panel of Figure 5.10). Morphology suggests us that a past slump could not be excluded, even if no deposit could be detected in the front of the slope. Indeed, the slope profile exhibits a $1000\ m$ depth change in just $2\ km$ and could be related to a shift mass movement, but it can also be explained in terms of differential erosional processes. For this case, we reconstruct the sliding surface and part of the missing mass for a $7\ km$-length sector. We suppose that a part of this volume was eroded after the slide movement. Since we are far from the volcano vents, the slump could have been possible only over an inclined slope. The total volume is in the order of $1.8\ km^3$.

In the third case, we simulate the collapse of a considerable portion of the eastern flank of Marsili. The red area shown in the contour graph in Figure 5.10 delimits the $104\ km^2$ initial sliding area. The reconstructed sliding volume is in the order of $19\ km^3$, considering an average thickness of $180\ m$. Collapses of this magnitude cannot be excluded over this kind of structures. As was already noted in Section 1.7, the present-day morphology of the Vavilov volcano indicates a past huge mass failure of this type. This volcano, located in the central part of the Tyrrhenian Sea, shows a peculiar morphology, as is shown in the contour map of Figure 5.11. The western part of the dome is clearly missing, suggesting a past noticeable flank collapse. Even if the Marsili seamount is younger than Vavilov, they share a similar geological origin and setting, and a similar *supposed* eruptive style. As a matter of fact, the nature of the past eruptions of these volcanoes and their effects are still uncertain. The lack of direct and systematic measurements on the volcano's dome does not allow us to predict the timing or the nature of potential eruptions.

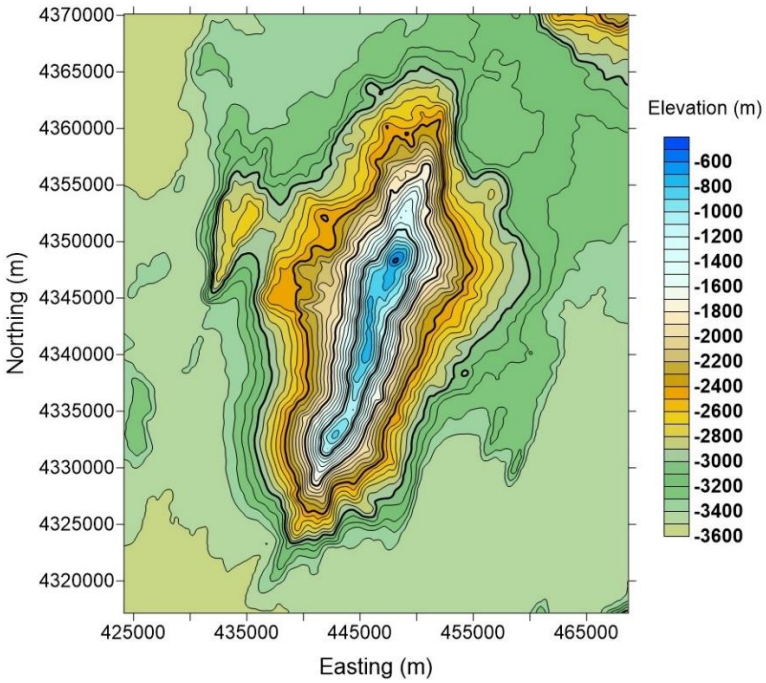

Figure 5.9 Contour map of the Marsili volcano structure and surrounding area. Bathymetric isolines are shown every 100 m. Notice that the elongated structure exhibits steep slopes mainly on the W-E direction.

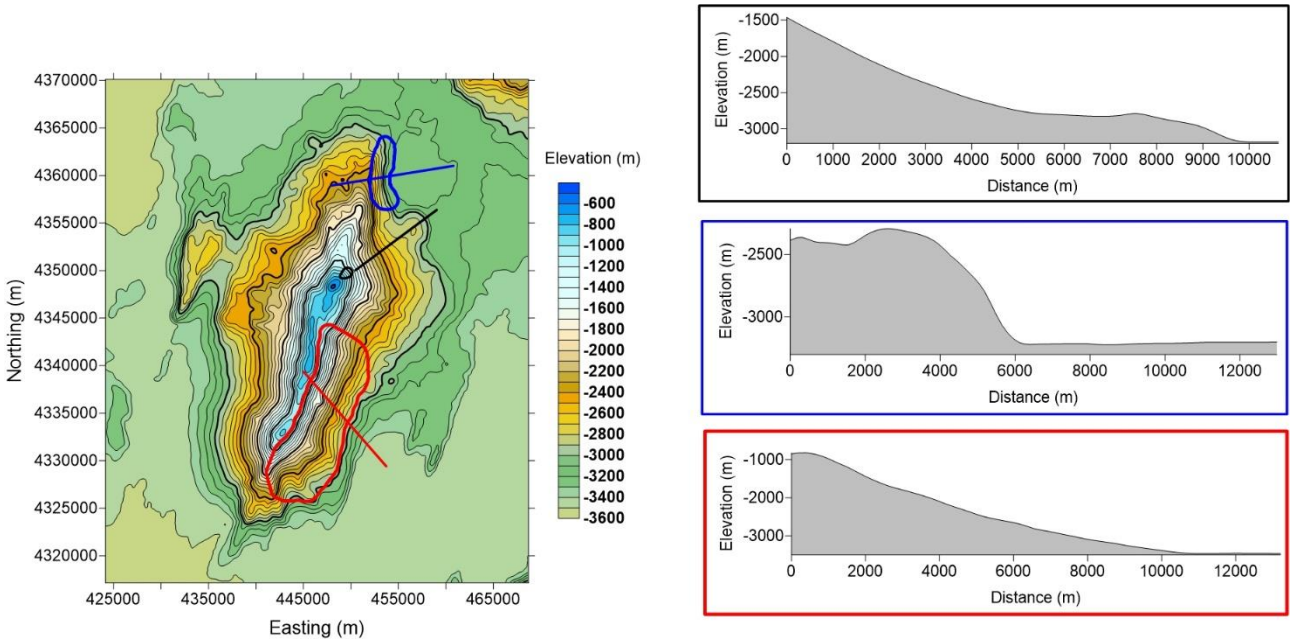

Figure 5.10 Left map: Locations of the initial sliding area for the three cases analyzed in this section. The black one is the small-size rock avalanche. The blue one represents a medium-size slump. The red one is a partial collapse of the eastern flank. Right panels: For each slide, a cross-section along the transects shown on the left map is plotted. This is the present-day morphology. In the next sections, the hypothesized reconstructed sliding masses will be shown in detail.

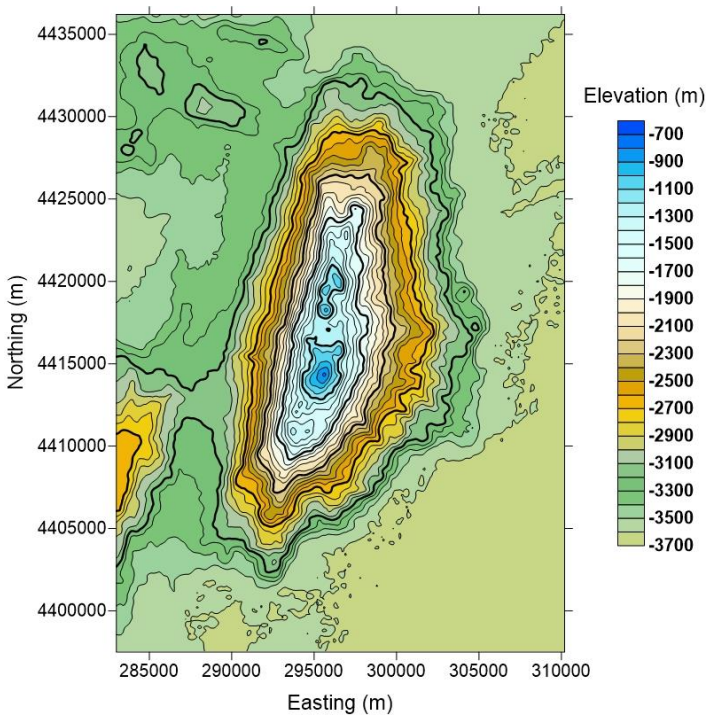

Figure 5.11 Contour map of the Vavilov seamount and the surrounding area. Bathymetric isolines are shown every 100 m. Notice that the western part of the dome is partially missing, suggesting past huge collapses. A similar flank failure is supposed to occur over the Marsili volcano (red area in Figure 5.10).

The slides' initial features are summarized in Table 5.1. Like for the Scilla case, for each simulation, we will show the results from the models UBO-Block and UBO-Inter. For both models we consider a rock density of $\rho_r = 2200\ kg/m^3$ and a sea water density of $\rho_w = 1030\ kg/m^3$.

Simulation	Volume	Average thickness
Small-size	40.3 Mm^3	28 m
Medium-size	1.8 km^3	114.5 m
Big-size	19 km^3	180 m

Table 5.1 Initial characteristics of the three reconstructed sliding masses over the Marsili volcano flanks.

5.3.1. The small-size rock avalanche

In what follows, we will first show the results from the model UBO-Block 2D and then the scenario computed by the model UBO-Inter. The detachment niche is located between 800 m and 1400 m depth. The sliding mass possesses an average thickness of 28 m, and a maximum thickness of 70 m. The cross-section over the initial sliding area is shown in Figure 5.12.

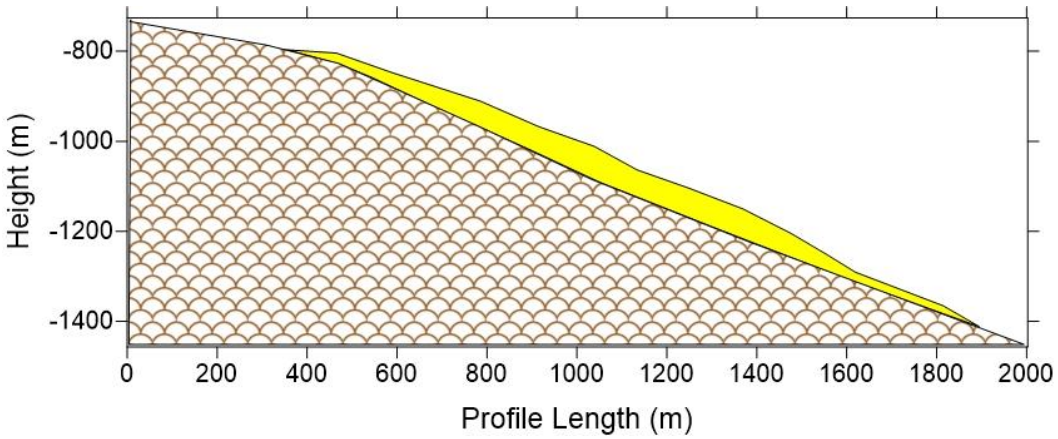

Figure 5.12 Cross-section of the initial small-size slide. The stable bedrock is coloured in brown. The sliding mass is shown in yellow. The initial average thickness is 28 m, with peaks of 70 m.

The set of parameters chosen for the model UBO-Block and its main results are summarized in Table 5.2. The slide trajectory is shown in Figure 5.13 on a contour plot. The landslide is portioned in 4 equal 550 m-edge blocks, covering the initial area, that is of approximately 1 km^2. The velocity plots are shown in Figure 5.14.

Stop time (s)	Number of blocks	Friction coefficient μ	Final average thickness (m)	Deposit area (km^2)	Velocity peak (m/s)	Movement type
245	4	0.09	15	2.1 km^2	57	Rock-avalanche

Table 5.2 Parameters and results for the small-size slide, for the UBO-Block 2D model.

The slide follows a SW-NE trajectory, covering a 9km-long path in 4 min. In the final position, just above the only deposit observed on this flank, the slide footprint is broader than the initial one, reaching a value of 2.1 km^2. Thus, its average thickness is lower, in the order of 15 m. The velocity peak of 57 m/s is reached after 70 s.

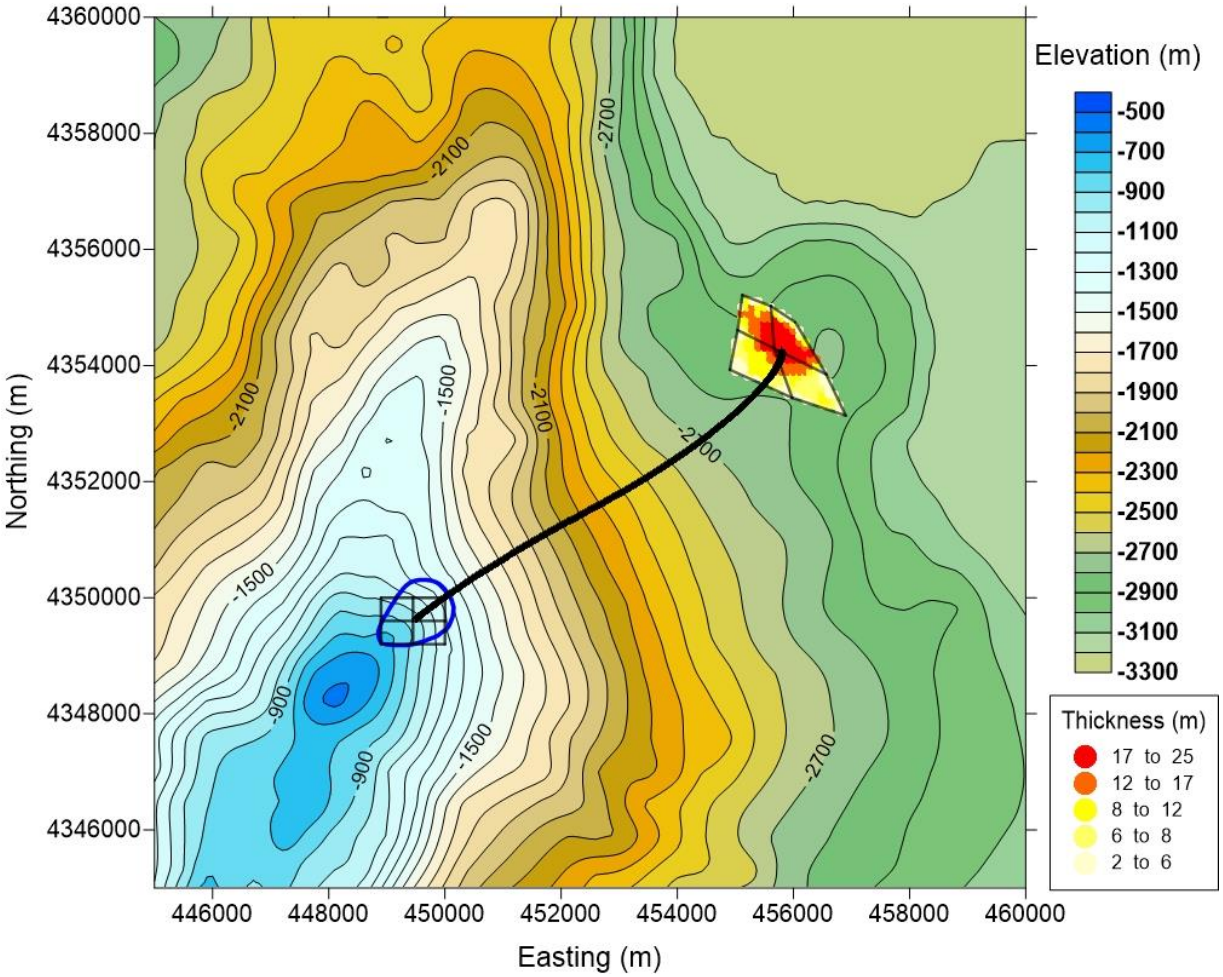

Figure 5.13 Trajectory of the small-size slide CoM over a contour map of the reconstructed bathymetry. The blue line delimits the detachment niche. The slide is portioned in 4 blocks, shown in light black. The final slide thickness is depicted through a yellow-red palette. Notice that in the final position the blocks are deformed covering a broader area.

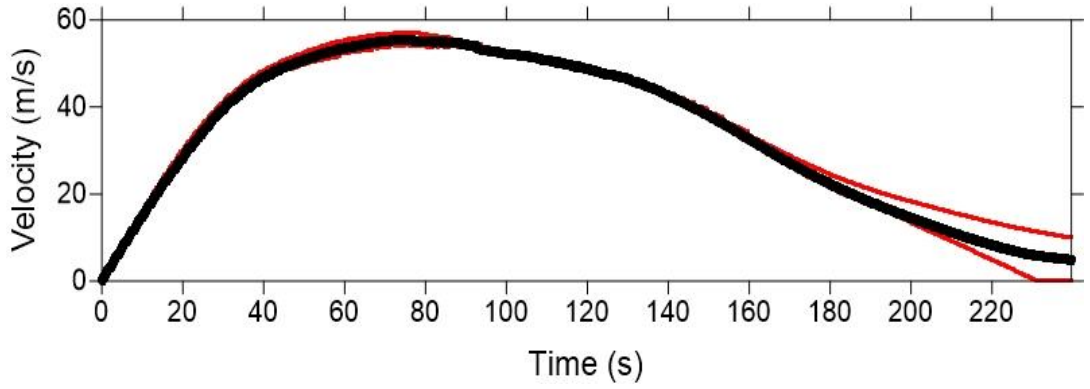

Figure 5.14 Results from the model UBO-Block 2D. The CoM velocity is shown with the black line. The red curves represent the block speeds.

The selected parameters and main results of the model UBO-Inter are summarized in Table 5.3. The mass distribution is designed considering the initial thickness introduced before. The slide CoM trajectory is shown in Figure 5.15 over a contour map, showing a path similar to the UBO-Block result. Velocity curves for each point mass and for the slide CoM are plotted in Figure 5.16. Notice that the slide stops at $230\ s$, some $10\ s$ before the model UBO-Block. The slight difference is

probably related to the different ways the models calculate the drag force. Like in the Scilla case, the drag force is here accounted for in terms of a corrected friction coefficient and it is applied only to the point masses directly facing the water in the direction of motion. The internal forces, normalized over the mean gravity force, are shown in Figure 5.17. The stronger values are reached by the elastoplastic forces in the first part of the simulation, and are about $20\%\ \bar{m}g$. Notice that in this simulation these forces are considered only on one diagonal for each quadrangle of the mass grid. The side-edge forces show weaker values but similar behavior in time. While the point masses slow down all the internal forces exhibit a more regular behavior and present values close to zero.

N	N_Q	N_E	N_D	$m(kg)$	Friction coefficient μ	Stop time (s)	Velocity peak (m/s)
9	4	12	4	$(3.6-15)10^9$	0.09	230	54

Table 5.3 Selected parameters and main results of the UBO-Inter model for the small-size slide.

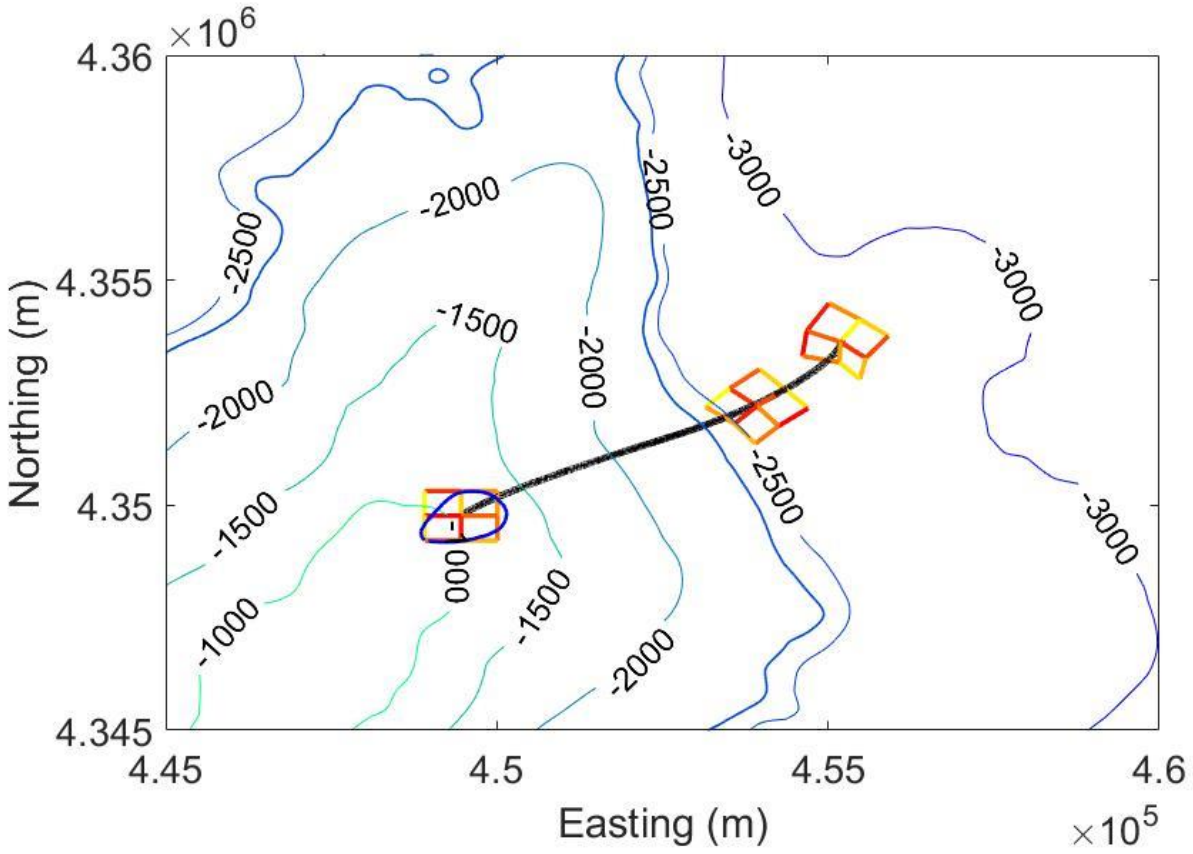

Figure 5.15 Landslide trajectory from the model UBO-Inter is given by the black line. Depth values are in meters. The detachment niche is delimited by the blue line. The side-edge forces magnitude is represented with different colors, ranging from yellow (weaker forces) to red (stronger forces), at the instants $t = [0;\ 115;\ 230]s$.

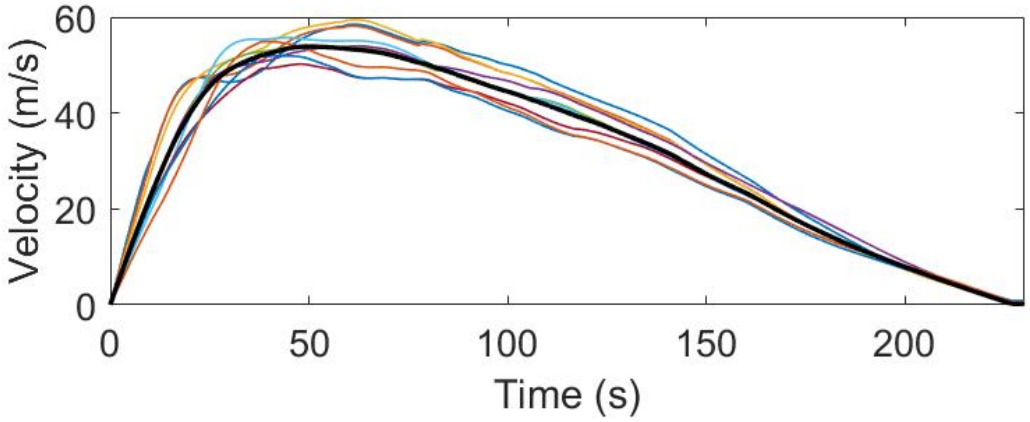

Figure 5.16 Results from the model UBO-Inter. The CoM velocity is represented with the black line. The colored curves refer to the point-mass velocities.

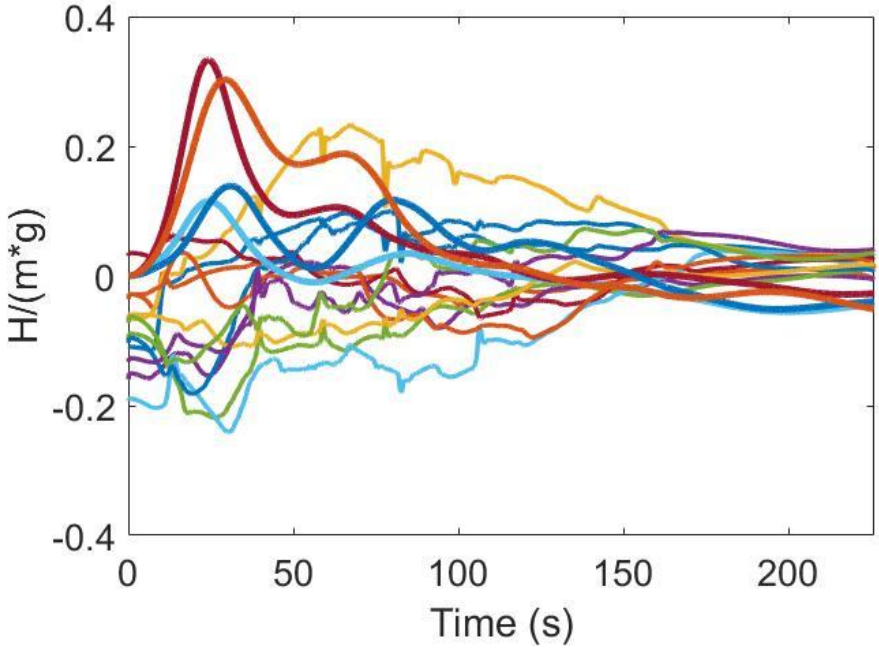

Figure 5.17 Internal forces for the small-size slide. The thicker lines represent the elastoplastic forces, the thinner lines the side-edge forces. Notice that the maximum values of the elastoplastic forces are reached in the initial part of the motion when the point masses possess the largest velocities.

5.3.2. The medium-size slump

The initial medium-size sliding mass covers an area of about 18 km^2. In this case, due to the peculiar bathymetry (see the middle panel in Figure 5.10 right side), we have reconstructed a part of the sliding surface. In fact, we suppose that part of the underlying bedrock is today missing since it was eroded after the mass movement. For the sake of clarity, a cross-section over the central part of the initial sliding area is shown in Figure 5.18.

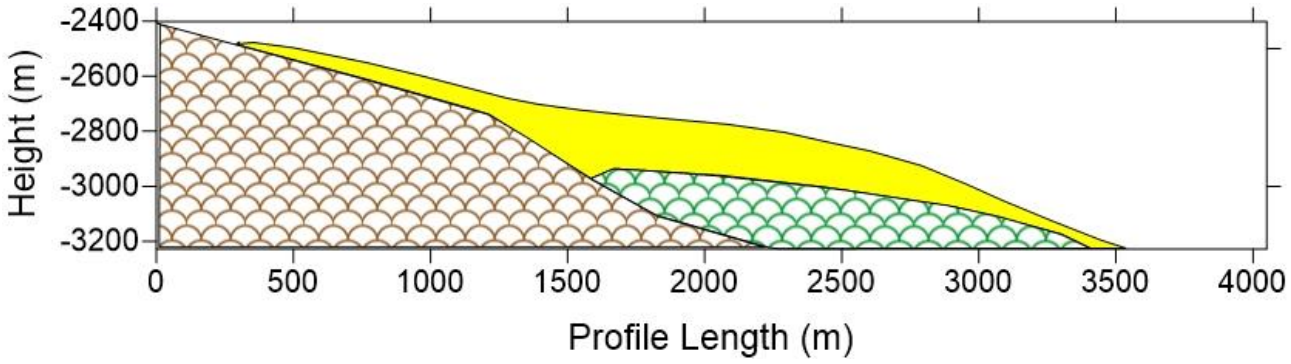

Figure 5.18 Cross-section of the initial sliding area for the medium-size slide. The brown part represents the present-day bathymetry. The green one is the reconstructed part of the slope supposed to be eroded after the slide. The yellow section represents the sliding mass, with an average thickness of 115 m and peaks of 235 m.

The selected parameters and main results for the model UBO-Block are summarized in Table 5.4. The 1.8 km^3 rock volume is portioned is 51 regular blocks. The slide moves downslope, stopping some 1.2 km away from the detachment niche (see Figure 5.19). The slide thickness is preserved during the motion that lasts for 160 s. In fact, the wide flat area facing the scar restricts the motion over a relatively small area. This is the typical behavior of a slump, where the movement time- and space-scales are limited.

The velocity peak is reached after 80 s (see the black line in Figure 5.20). The individual blocks accelerate differently in the first part of the motion, but they slide down similarly in the final part (red lines in Figure 5.21).

Stop time (s)	Number of blocks	Friction coefficient μ	Final average thickness (m)	Deposit area (km^2)	Velocity peak (m/s)	Movement type
160	51	0.09	110	17.8 km^2	27	Slump

Table 5.4 Parameters and results of the medium-size slide, for the model UBO-Block.

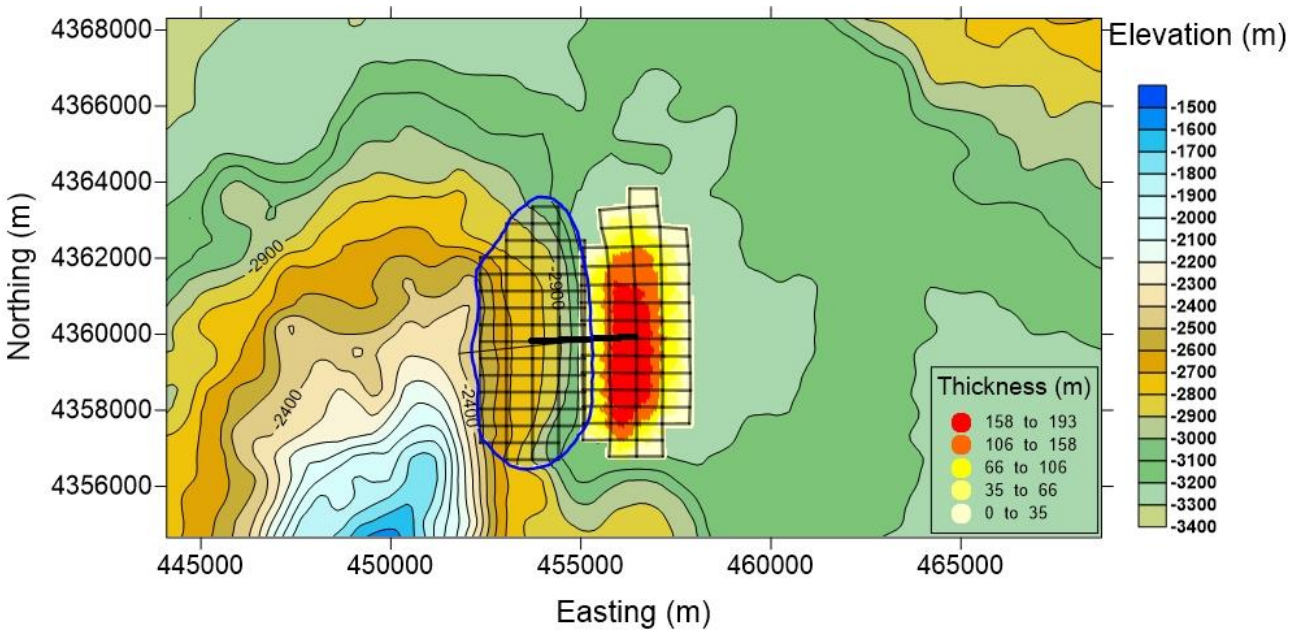

Figure 5.19 Trajectory of the medium-size slide over a contour map of the reconstructed bathymetry. The blue line delimits the initial sliding area. The slide is portioned in 51 blocks, shown in light black. The final slide thickness is depicted with a yellow-red palette.

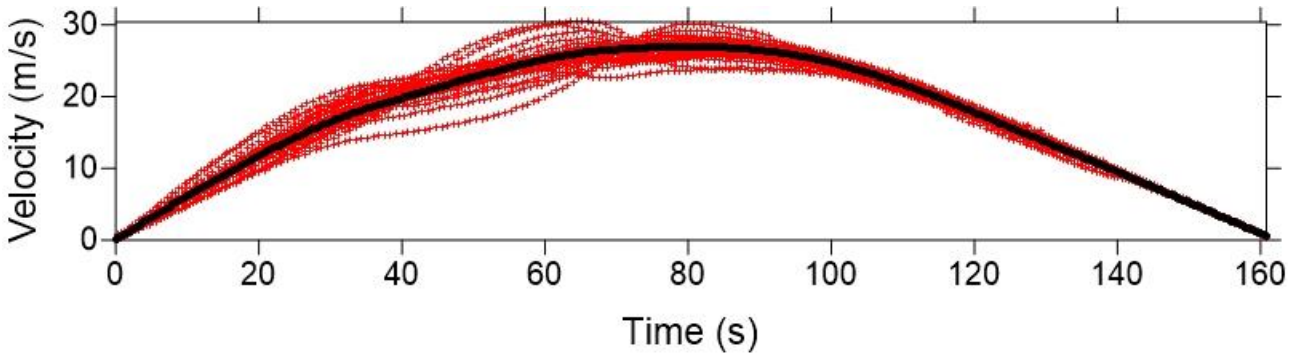

Figure 5.20 Results from the model UBO-Block for the slump. The CoM velocity is shown with the black line, while the red lines are the velocity curves of the constituent blocks.

In the model UBO-Inter, the sliding area is portioned in $N = 71$ point masses, forming $N_Q = 51$ quadrangles. The model input and main results are summarized in Table 5.5. The mass distribution, that is designed according to the slide thickness, shows a broad range of values, between $3.710^6\ kg$ to $1.3\ 10^{11} kg$. The slide CoM trajectory (Figure 5.21) is similar to the one of the UBO-Block case. Nevertheless, in the final position, the mass grid is more deformed. While the system CoM stops at $t = 125\ s$, some point masses are still moving at this stage. This is the case of the particles located in the southern and northern mass grid extremes. In fact, since the strongest interaction forces are the ones of the masses gathered around the CoM, the masses set at the extremes are subject to weaker bounds and have more ability to move. This result reflects the final mass distribution obtained from UBO-Block (see Figure 5.19), where the deposit is thicker in the central part and thinner close to its boundary. The CoM velocity peak is reached at $t = 63\ s$ (Figure 5.22). Thus, even in this case, the maximum is reached in the central part of the motion. The internal forces curves (Figure 5.23) show some peaks of the side-edge forces, with values in the order of $2\bar{m}g$. This reflects the erratic behavior

of some masses due to the peculiar, strongly inhomogeneous, mass distribution. On the contrary, the elastoplastic forces show a more regular behavior. Since we have considered these forces acting on both diagonals of each force quadrangle, a more stable trend with respect to the small-size case was expected. Overall, the ability to deform of each quadrangle is reduced when both diagonals have elastoplastic characteristics. When the CoM stops, the internal forces have a tendency to diverge. As we have shown in other cases, this happens since the point masses would normally tend to spread.

N	N_Q	N_E	N_D	$m(kg)$	Friction coefficient μ	Stop time (s)	Velocity peak (m/s)
71	51	121	102	$3.7\ 10^6 - 1.3\ 10^{11}$	0.09	125	37

Table 5.5 Selected parameters and main results of the model UBO-Inter for the medium-size slide.

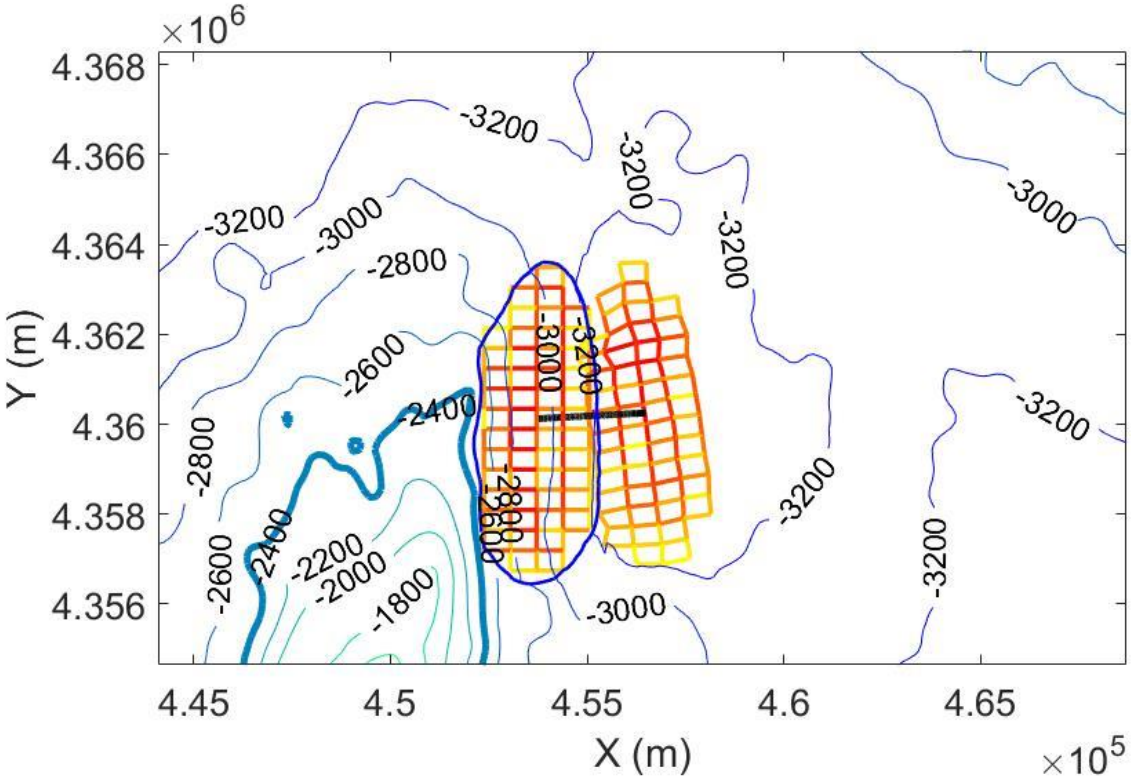

Figure 5.21 Trajectory of the medium-size slide from UBO-Inter. The initial sliding area is depicted with the blue line. The magnitude of the side-edge forces is given by using a color code, ranging from yellow (weaker forces) to red (stronger forces). Its distribution is shown at the time instants $t = [0;\ 160]s$.

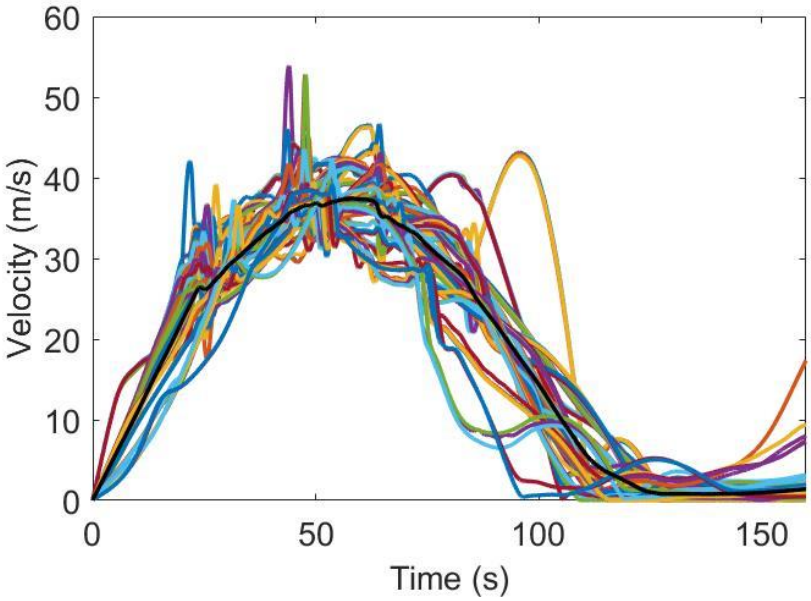

Figure 5.22 Results from the model UBO-Inter for the medium-size slide. The system CoM velocity is shown with the black line. The coloured lines refer to the point-mass velocities. Notice that when the CoM speed is very small, and we assume that it stops (i.e. at $t = 125\ s$), some point masses are still moving.

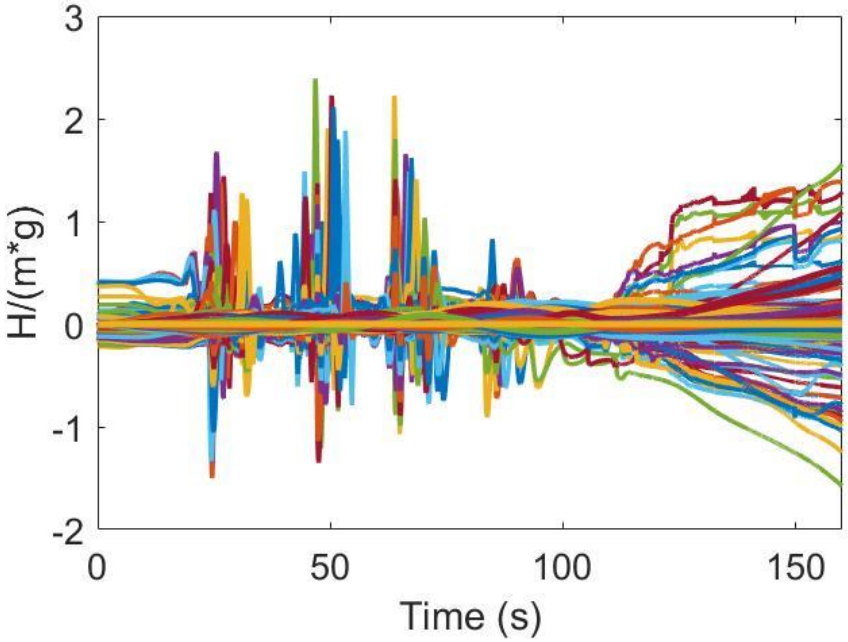

Figure 5.23 Internal forces curves for the medium-size slide. The thicker lines denote the elastoplastic forces, the thinner lines the side-edge ones. Notice that the peaks of the side-edge forces reflect the peaks of velocities of some point masses.

5.3.3. The eastern-flank collapse

The collapse of the eastern flank of the Marsili volcano represents the biggest challenge in terms of computational effort for both models. For the sake of clarity, a series of profiles over this section is shown in Figure 5.24. Clearly the structure is not symmetric. This morphology suggests us that a past collapse of this sector could not be excluded. A 200 m-thick layer facing part of the eastern flank is also clear. This area could represent a part of the slide deposit.

A volume of 20 km^3 is reconstructed over the selected initial sliding area of 102 km^2(see the area enclosed within the red line in Figure 5.10). The area is 5.5 km wide and 18 km long. A cross-section of the central part of this sector is shown in Figure 5.25. The thickness distribution is quite regular in the S-N direction, following the original bathymetry. The average slide thickness is in the order of 180 m, with maximum values around 415 m. The landslide body covers depths from 900 m down to 2900 m.

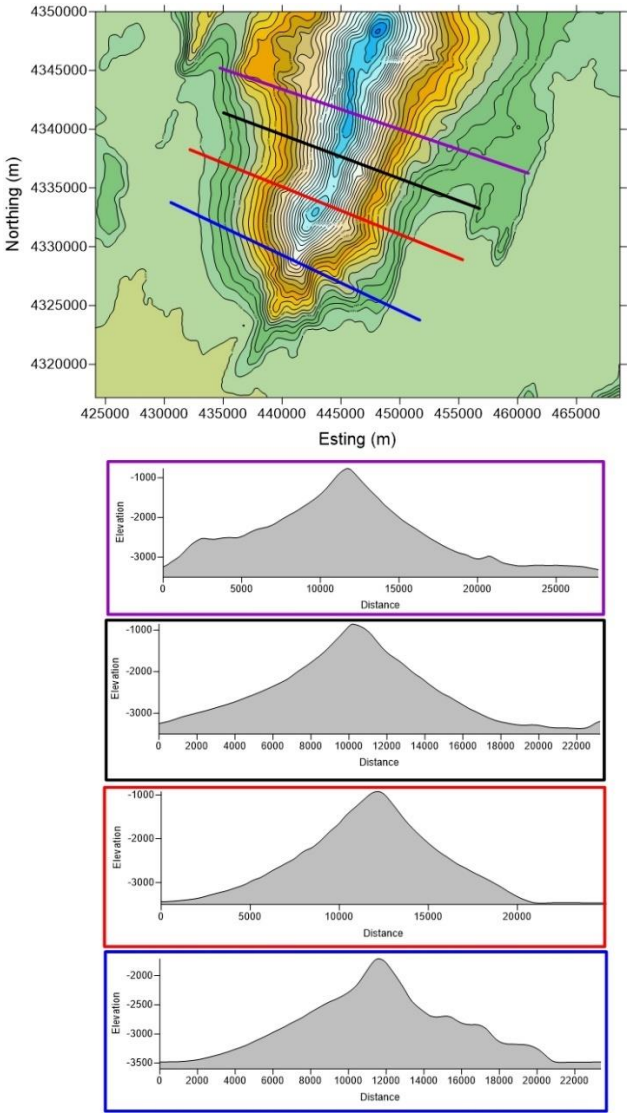

Figure 5.24 In the upper panel, a contour map of the southern part of the Marsili volcano is shown. The transects represent the locations of the cross-sections shown on the bottom panels. Notice the asymmetry between the two volcano's flanks, particularly strong in the northernmost profile.

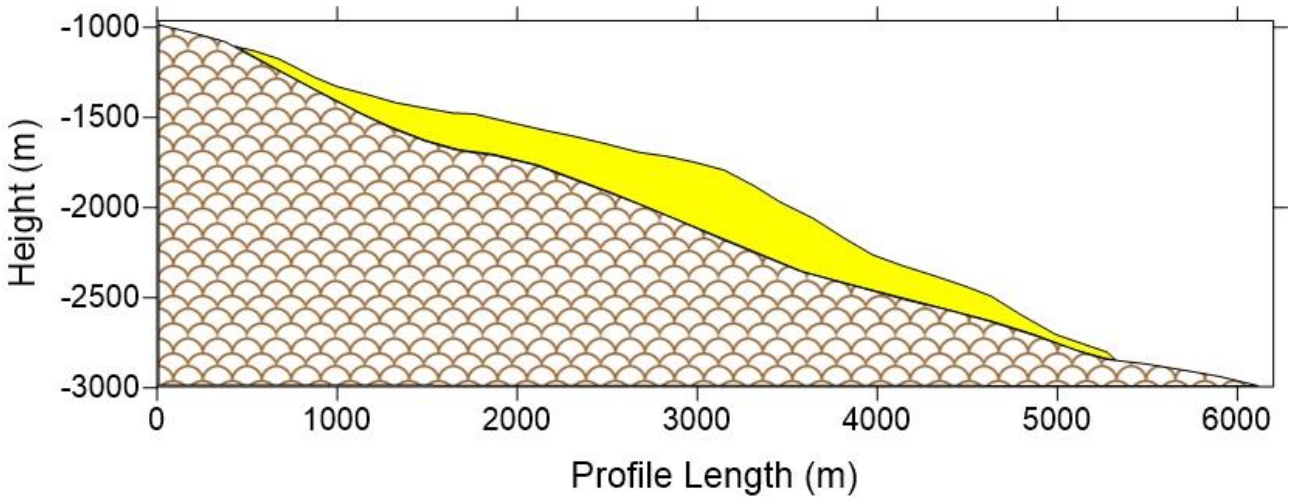

Figure 5.25 Cross-section of the initial sliding area. The underlying bedrock is coloured in brown. The sliding mass is shown in yellow. The initial mean thickness is 180 m, with peaks of 415 m.

Stop time (s)	Number of blocks	Friction coefficient μ	Final mean thickness (m)	Deposit area (km^2)	Velocity peak (m/s)	Movement type
250	85	0.09	150	136 km^2	65	Collapse

Table 5.6 Parameters and main results of the big-size slide simulation for the model UBO-Block.

The landslide body is portioned in 85 blocks. The CoM trajectory follows a NW-SE path, as is clear on looking at Figure 5.26 (black line). The flank collapses rapidly. In approximately 4 min the whole mass leaves the seamount slope and spreads over the basin. In the final position, the originally regular mass distribution is partially lost. Two thicker areas (denoted in red) can be noticed. This distribution is a consequence of a morphological irregularity that breaks the quite regular bathymetry of this side. A bulge on the flank presents a flat top, surrounded by two steep sides. This leads to a sort of a division of the sliding mass. The central and northern parts follow the CoM while the southern part presents a clear drift to the south. The final area is overall broader (about 136 km^2) resulting in a lower average thickness of 150 m. The CoM velocity reaches a peak of 65 m/s at $t = 105\ s$ (see Figure 5.27). Nevertheless, some blocks reach speed values as high as 80 m/s.

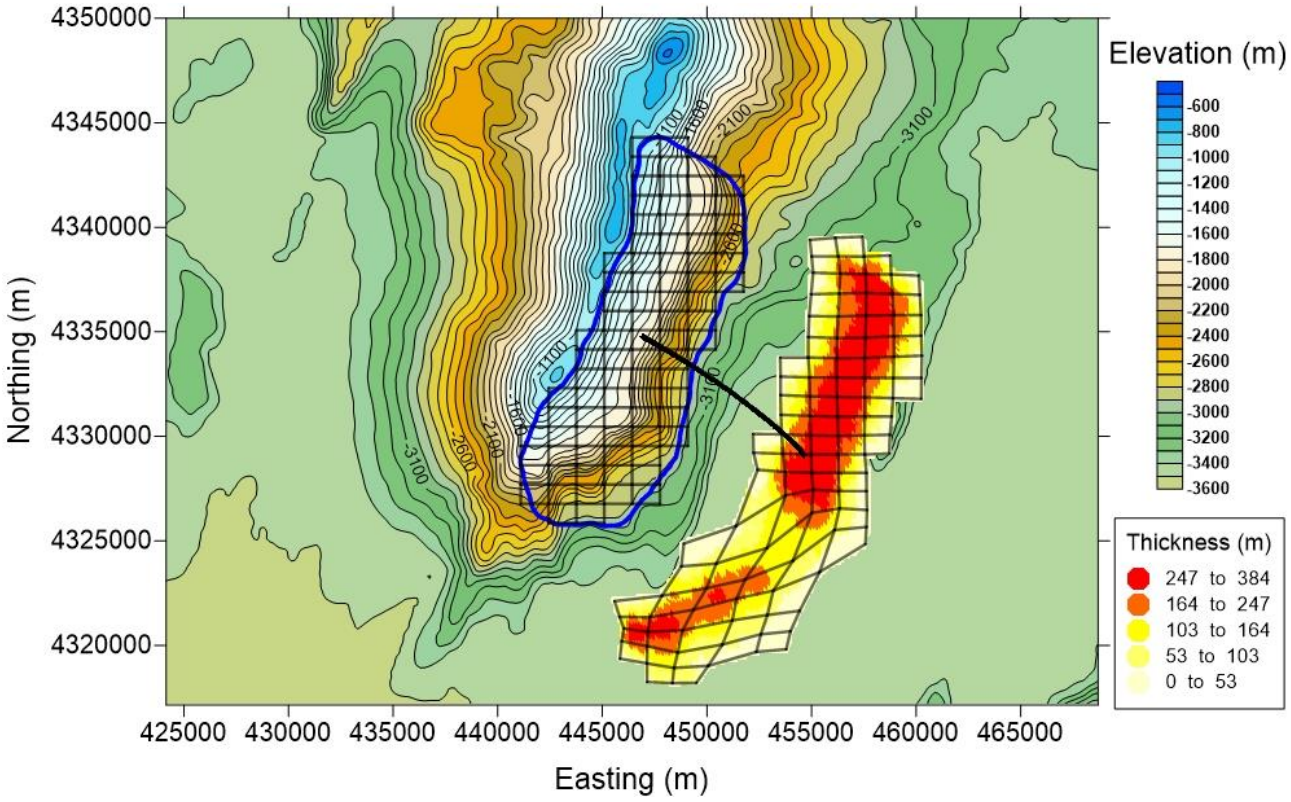

Figure 5.26 The CoM trajectory of the collapsing eastern flank is shown with the black line over a contour map of the reconstructed bathymetry. The block partition is shown in light black, while the initial area is bounded by a blue line. The final slide thickness is given with a yellow-red palette. Notice that the final area is slightly deformed, and the deposit shows an irregular thickness distribution.

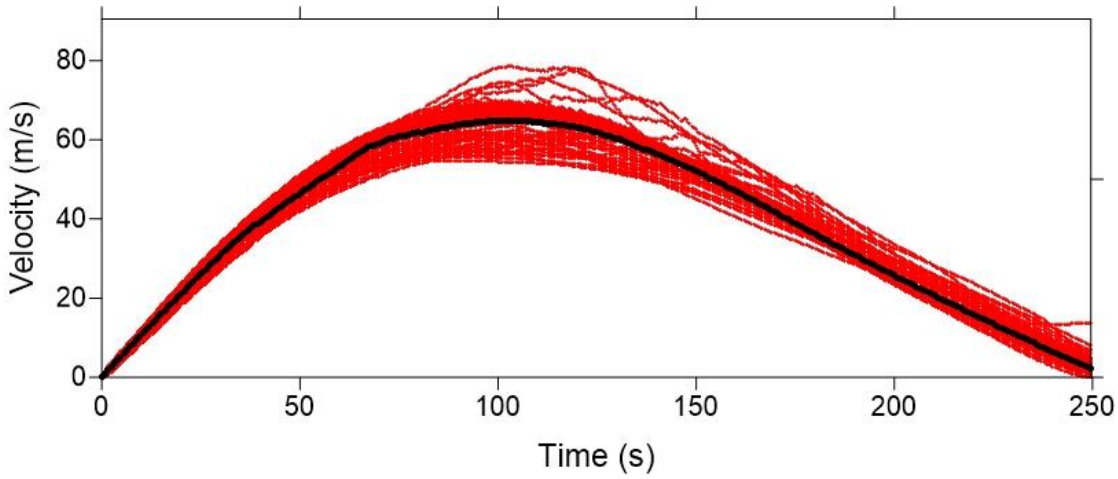

Figure 5.27 Results from the model UBO-Block for the Marsili flank collapse. The CoM velocity is shown with the black line. The red lines depict the blocks' velocities. Notice that some blocks reach a speed as high as 80 m/s.

In the model UBO-Inter, the slide is divided into $N = 133$ points, connected through $N_E = 237$ side edges, forming $N_Q = 104$ force quadrangles. In this case, the mass distribution is considered uniform.

The model input and main results are summarized in Table 5.7. The slide trajectory is shown in Figure 5.28, and is similar to the one computed by means of UBO-Block. Here the slide runs over a slightly longer distance, and the structure clearly loses its initial regularity. During the motion, the mass grid shows an elongation over the SW-NE direction but in the final part of the simulation, the mass grid is twisted around the CoM. Correspondingly, the final distribution of the interaction forces shows peaks around the CoM and lower values in the northern part of the mass grid. The CoM velocity peak is $80\,m/s$, but some point masses reach values around $100\,m/s$ (see Figure 5.29). This wide distribution of velocities is due to the different local slope gradients, that range from 15° in the deeper area, until 40° in the up-hill part. The internal forces curves, normalized over the mean gravity force, are shown in Figure 5.30. Both types of forces (side-edge and elastoplastic forces) present a similar pattern until $100\,s$, with mean values in the order of $1.5\bar{m}g$. Later, a clear divergence can be noticed. We stop the simulation some $15\,s$ before the estimated slide stop. In fact, the high number of point masses and the strong irregularity of the sliding surface lead the system to some instability after $t = 200\,s$, with results that become unreliable. Nevertheless, the system trajectory and velocity are comparable with results from the model UBO-Block and proved to be physically consistent.

N	N_Q	N_E	N_D	$m(kg)$	Friction coefficient μ	Simulation time (s)	Velocity peak (m/s)
133	104	237	208	$2.1\,10^{11}$	0.09	200	80

Table 5.7 Selected parameters and main results of the model UBO-Inter simulation for the Marsili flank collapse.

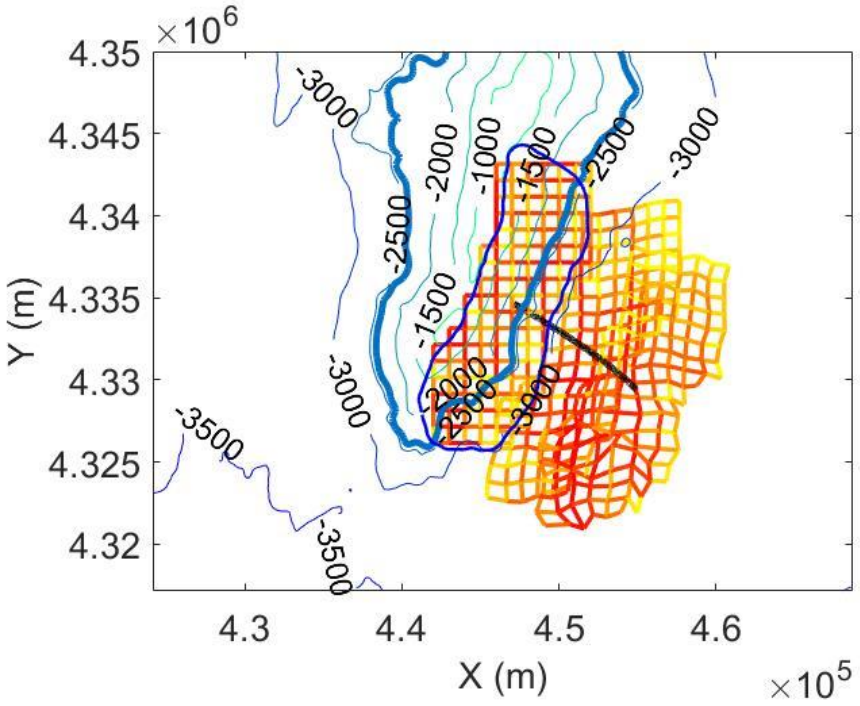

Figure 5.28 The landslide CoM trajectory from the model UBO-Inter is shown with the black line. Depth values are shown in meters. The initial sliding area is delimited by the thin blue line. The magnitude of the side-edge forces is given through a color code, with colors ranging from yellow (weaker forces) to red (stronger forces). Its distribution is shown at instants $t = [0;\ 100;\ 200]\ s$

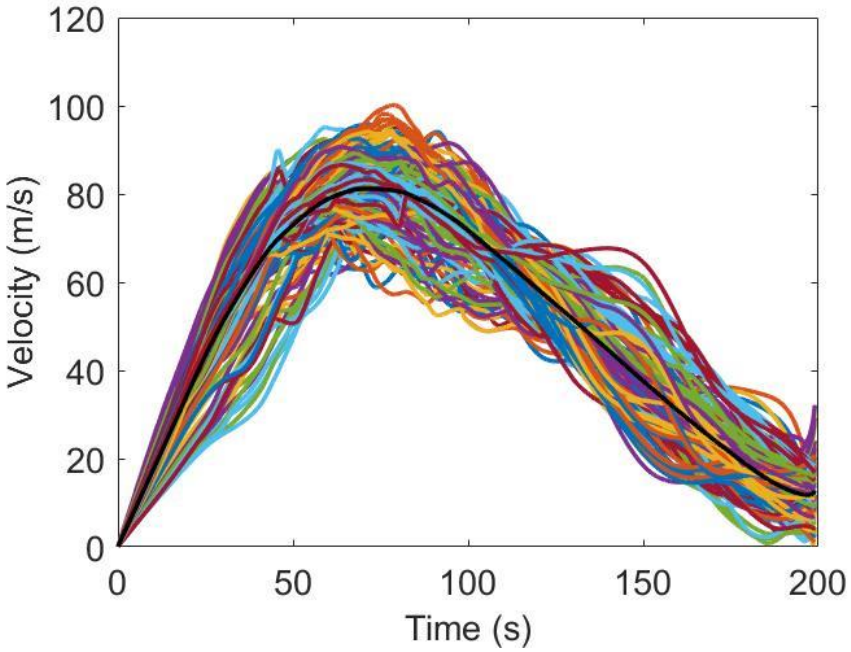

Figure 5.29 Results from the model UBO-Inter for the big-size slide. The system CoM velocity is shown with the black line. The coloured lines denote the point-mass velocities. Notice the wide range of velocities as a consequence of the quite different local slope gradients.

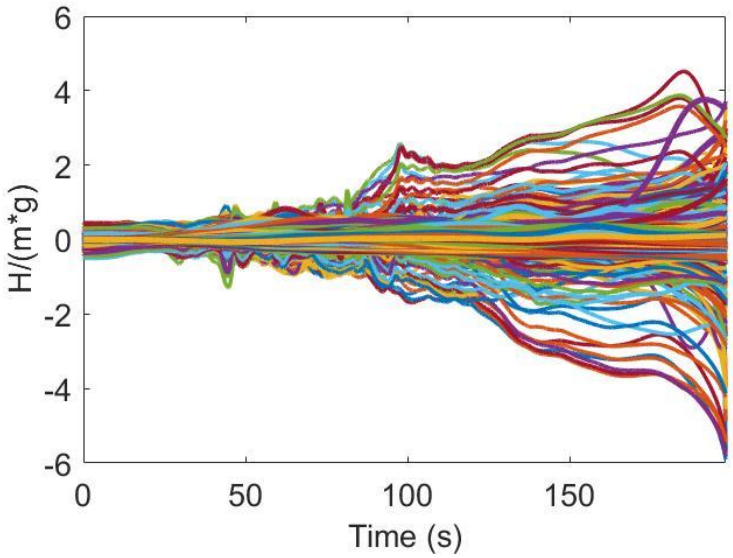

Figure 5.30 Internal forces curves for the collapse of the eastern flank of the Marsili volcano. The thicker lines refer to the elastoplastic forces, the thinner lines to the side-edge ones. Notice the divergence after 100 *s* related to the strong irregularity of the sliding surface and to the considerable number of point-masses.

6. Conclusions

In this work, we have presented a new numerical model (UBO-Inter) capable to simulate the motion of sliding bodies over generic surfaces, adopting an original approach to the problem. The body is portioned in a series of massive points having neither a shape nor a volume. Basically, they represent the CoM of hypothetical blocks that form the sliding body. The point masses are anytime adherent to the surface and some of them are bounded to stay at the same 3D distance. This latter constraint is imposed through the introduction of an interaction force acting between pairs of masses, that can be connected in several ways. Among various explored options, we have observed that a force pattern based on quadrilaterals is the most convenient. Pointedly, we have seen that the best configuration for the mass grid presents constant-distance conditions on the side edges of the quadrilaterals and an elastoplastic behavior on the diagonal ones. Elastoplasticity is ruled by a 6-parameter law giving the strength of the force as a function of changes of the mass distance (i.e. of the diagonal length) and that can describe a wide class of material behaviors. In addition to the internal forces, the point-mass system is subject to external forces: these are gravity, sliding surface reaction, basal friction and water drag when needed. The model UBO-Inter has been developed to model the rock motion. While individual portions of rock systems present rigid body characteristics, the interaction of moving rocks has a more complex nature, which accounts for slide volume changes and deformations. This dual behavior is fully described in our model by the introduction of the side-edge and elastoplastic forces.

In Chapter 3 the model has been presented and tested on cases with simple geometry for some of which analytical exact solutions are available (see also the Appendices). In all these examples the performance of UBO-Inter was proven to be very good. This part of the work has also the merit to allow us to highlight the basic concepts behind the model UBO-Inter in a simple way. The interaction forces, that in this part of the work are only the ones keeping the distance between selected pairs of point masses constant, are evaluated by means of bounds on the point-masses mutual accelerations. Later in the thesis (Chapter 4) we call these forces side-edge forces since we apply them along the side of quadrilaterals forming the force pattern of the point-mass system. Fixed-constant bounds pertain to the rigidity of the body. When only these bounds are present in the system, we speak of a semi-rigid body behavior (see Chapter 4), where “semi” refers to the fact that the system moving on a slope adapts its shape to the slope itself (we recall that masses cannot leave the slope) and is not perfectly rigid. When the number of fixed-constant constraints becomes too high (namely it is such that the system degrees of freedom is less than what is permitted to a rigid body), the system is over-constrained, and the corresponding problem formulation is overdetermined with no admissible solutions. In this case the model does not provide any results either because of impossible calculations or because of numerical instabilities.

The equations of motions are written in terms of the space derivatives of the sliding surface, that can be computed at any point with high accuracy when the slope admits an analytical expression. For real topographies given by elevation regular matrices, specific interpolation procedures have to be adopted since, if derivatives are approximated too rough, then numerical errors can compromise the system motion soon. We have adopted a spline interpolation method (see Section 5.1) with parameters tuned in such a way that the procedure has the advantage of being quick and of providing satisfactory approximations. In general, the selection of the model parameters has to be made with attention since

a wrong selection can lead to unsatisfactory results or even to instabilities. This however is not a specific disadvantage of UBO-Inter since it is common to all simulation models.

In Chapter 5, we have applied the model to simulate selected real scenarios. In these cases, the landslides have been also simulated by means of another model, namely UBO-Block. As explained in Section 2.3, this latter belongs to the category of the block-based models, adopting a Lagrangian approach, and has been validated through laboratory data and geophysical applications. Consistently, we have used the same topography and the same initial slide geometry for UBO-Block and for UBO-Inter. Indeed, in the model UBO-Inter that deals with dimensionless point masses, the only way to consider the thickness of a slide is by associating each point mass m_i with a sort of a virtual block that: 1) has the same mass, 2) has a basal area A_i surrounding the point mass selected in such a way that the set of all A_i constitutes a partition of the basal area of the entire slide, 3) has a height H_i that can be simply computed as $H_i = m_i/(\rho_r A_i)$ where ρ_r is the density of the rock. As a consequence, a variable-thickness homogeneous slide can be represented by a heterogeneous distribution of point masses with a mass grid covering the slide area. As regards the forces typically acting on the surface of the slide, such as the drag, that have a fundamental role when the slide moves underwater, these have been implemented in the model UBO-Inter as additional resistance forces that act on a selected subset of point masses and have a magnitude depending on the square of the mass velocity (see the formula in Section 5.2). The point masses where the drag is active are the ones in the frontal region of the landslide. In this version of the code they are selected statically, that is a priori, but one can easily implement a dynamic identification of the drag-affected point masses that can change during the motion.

The case of the 1783 Scilla slide treated in Section 5.2 represents the benchmark study in this work since it has been widely studied in the literature, and numerical and observational data are available. The UBO-Inter results are similar to the UBO-Block (1D) ones, in terms of slide velocity. The case is however critical as regards the slide mass spreading. The final deposit area is much larger than the area covered initially by the slide, i.e. the niche area. This is an unfavorable condition for UBO-Inter, but not for UBO-Block 1D. Indeed, the blocks of the model UBO-Block (1D) can modify drastically their shape while sliding, though they preserve their volume. Instead, the specific implementation of the side-edge forces and of the elastoplastic forces made in the present version of the model UBO-Inter does not permit large deformations to occur for the point-mass system. This drawback will be the object of future possible post-doctoral work.

The model UBO-Inter has been applied to study mass movements occurring along the slopes of the Marsili submarine volcano (see Section 5.3). These applications depict for the first time some possible past/future scenarios that are relevant also for tsunami generation and hence for natural hazard assessment in the Tyrrhenian region. Nevertheless, one should notice that Marsili is much less known than many other volcanoes in Italy, which means that the available data do not provide very stringent constraints for our simulations and that a number of subjective hypotheses and choices had to be made. It is known that the Marsili dome is still active, but the specific characteristics of a possible eruption and its effects are still mainly uncertain. We have simulated three different slide-scenarios that cover a range of possibilities from a small- to a huge-volume landslide. Size and movement type are different, which also proves that the model UBO-Inter is suitable to describe different kinds of motion. For all cases the results are consistent with the finding from the model UBO-Block (2D) in terms of slide velocity and trajectory. In further studies, the tsunami generation and propagation related to such movements will be studied in detail, which, we believe, will be a significant contribution to evaluate the tsunami hazard for a large part of the coastal areas of the southern Tyrrhenian Sea.

APPENDIX A

The following Appendix is part of a technical paper written by *Gallotti and Tinti* in preparation.

The equations of motion presented in this thesis are written in terms of the space derivatives of the sliding surface. For the sake of clarity, it is useful to consider the motion of a single particle sliding down an analytical surface and bounded to stay adherent to it. This simple case allows us to highlight the general expressions of the forces acting on the system.

Let us assume that a point mass slides on the surface $z = f(x, y)$ under the effect of gravity $\vec{g}$, that in a Cartesian right-hand unit-vector system $\vec{\imath}, \vec{\jmath}, \vec{k}$ with $\vec{k}$ directed upward, can be represented as

$$\vec{g} = -g\vec{k} \tag{A.1}$$

Let us further introduce a local set of three orthonormal vectors $\vec{s}_1,\ \vec{s}_2,\ \vec{n}$, where $\vec{n}$ is normal to the surface and points upward, $\vec{s}_1$ is the maximum-steepness tangential vector (i.e. it belongs to the vertical plane determined by $\vec{n}$ and $\vec{k}$ and points downward), and $\vec{s}_2$ is the horizontal tangent vector orthogonal to $\vec{s}_1$. In terms of the function f and its first derivatives f_x and f_y, the local unit-vectors system can be given through the following expressions:

$$\begin{aligned} \vec{s}_1 &= \frac{1}{\left[f_x^2+f_y^2+\left(f_x^2+f_y^2\right)^2\right]^{\frac{1}{2}}}\left[f_x, f_y, f_x^2+f_y^2\right] \\ \vec{s}_2 &= \frac{1}{\left(f_x^2+f_y^2\right)^{\frac{1}{2}}}\left[-f_y, f_x, 0\right] \\ \vec{n} &= \frac{1}{\left(1+f_x^2+f_y^2\right)^{\frac{1}{2}}}\left[-f_x, -f_y, 1\right] \end{aligned} \tag{A.2}$$

These three unit vectors form the basis of a right-hand Cartesian reference frame and degenerate only in the points of the surface where both derivatives f_x and f_y are equal to zero.

The gravity acceleration $\vec{g}$ can be represented in the local system and, noting that $\vec{g} \circ \vec{s}_2 = 0$, takes the form

$$\vec{g} = g_s\vec{s}_1 + g_n\vec{n} \tag{A.3}$$

where the components are given by: $g_s = \vec{g} \circ \vec{s}_1$ and $g_n = \vec{g} \circ \vec{n}$.

The reaction force exerted by the surface on the moving point is directed along $\vec{n}$ and points upward/downward depending on the local convexity/concavity of the surface. Denoting the reaction acceleration by $T\vec{n}$, one can write the following equation for the acceleration of a point mass:

$$\vec{a} = \vec{g} + T\vec{n} - \mu|T|\hat{v} \tag{A.4}$$

Here, it is further assumed that the friction term is proportional to the surface reaction through the friction coefficient μ and is always directed against the instant unit velocity vector $\hat{v}$. If one designates the point acceleration component normal to the surface by a_n, i.e. $a_n = \vec{a} \circ \vec{n}$, it is straightforward to deduce the expression for T. In fact, after dot multiplying both members of Eq.(A.4) by $\vec{n}$, and noting that $\hat{v} \circ \vec{n} = 0$, one gets

$$T = a_n - g_n \tag{A.5}$$

And, considering the decomposition of Eq. (A.3) the governing equation for the point mass can be given the following form

$$\vec{a} = g_s\vec{s}_1 + a_n\vec{n} - \mu|a_n - g_n|\hat{v} \tag{A.6}$$

It is known that the normal acceleration a_n can be expressed in terms of the point velocity and of the surface geometrical characteristics. For example, one can write $a_n = v^2/R$ where v is the velocity module and R is the local curvature radius. In our approach, it is convenient to express a_n by means of the expression:

$$a_n = \vec{v} \circ (\vec{v} \circ \nabla)\vec{n} \tag{A.7}$$

that is quadratic in the velocity components and where ∇ denotes the gradient operator. Taking advantage of Eq. (A.7) one can observe that in Eq. (A.6) the point acceleration $\vec{a}$ is expressed in terms of the driving gravity acceleration and of a_n, that depends on the local velocity. This property makes this formalization suitable to solve the problem through a Runge-Kutta explicit method.

Since the point is supposedly constrained to move on a surface, the problem can be reduced to a two-degree-of-freedom formulation. Taking into account that from $z = f(x, y)$ it follows that the vertical velocity component v_z is given by

$$\dot{z} = v_z = f_x v_x + f_y v_y$$

and that the vertical acceleration component a_z has the form

$$\dot{v}_z = f_x \dot{v}_x + f_y \dot{v}_y + f_{xx} v_x^2 + 2 f_{xy} v_x v_y + f_{yy} v_y^2$$

the 3D Eq. (A.6) can be solved only for the horizontal components of the point acceleration a_x and a_y. Note that in the above expression the second-order derivatives of the function f have been denoted by f_{xx}, f_{xy} and f_{yy}. After some manipulations, the governing set of equations becomes

$$\dot{v}_x = -\varphi(x,y)^2 [g + \vartheta(x,y)] f_x - \mu \varphi(x,y)\, \chi(x,y) |g + \vartheta(x,y)| v_x$$

$$\dot{v}_x = -\varphi(x,y)^2 [g + \vartheta(x,y)] f_y - \mu \varphi(x,y)\, \chi(x,y) |g + \vartheta(x,y)| v_y$$

where

$$\varphi(x,y) = \left(1 + f_x^2 + f_y^2\right)^{-\frac{1}{2}}$$

$$\chi(x,y) = \left[v_x^2 + v_y^2 + \left(f_x v_x + f_y v_y\right)^2\right]^{-\frac{1}{2}}$$

$$\vartheta(x,y) = f_{xx} v_x^2 + 2 f_{xy} v_x v_y + f_{yy} v_y^2$$

APPENDIX B

The following Appendix is part of a paper written by *Tinti and Gallotti* in preparation.

We formulate the problem of a system of two particles sliding on a surface and interacting with each other and illustrate some analytical examples. Since this thesis work is focused on the UBO-Inter model validation and on its geophysical applications, this formulation and the related examples are presented as an additional contribution to the thesis. This kind of study represents the early-stage of the UBO-Inter model. The related examples, yet necessary, have a theoretical nature.

We assume that two point-like particles with masses m_1 and m_2 are initially in the positions $P_1(x_1, y_1, z_1)$ and $P_2(x_2, y_2, z_2)$ on the surface $z = f(x, y)$, in a Cartesian reference system where x and y are the horizontal coordinates and z is the vertical one. The equations of motion for a couple of interacting particles sliding down a smooth surface are:

$$m_1\ddot{\vec{r}}_1 = \vec{F}_1 + \vec{h} - \left(\vec{h} \circ \vec{n}_1\right)\vec{n}_1 \tag{B.1a}$$

$$m_2\ddot{\vec{r}}_2 = \vec{F}_2 - \vec{h} + \left(\vec{h} \circ \vec{n}_2\right)\vec{n}_2 \tag{B.1b}$$

where $\vec{r}_i$ (i=1,2) are the 3D position vectors and $\vec{F}_i$ are the forces acting on the particles including the effect of gravity and of surface reaction. By $\vec{h}$ we denote the interaction force exerted by mass 2 on mass 1 and is supposed to be equal in intensity and contrary to the force acting on mass 2 by mass 1; $\vec{n}_i$ are unit vectors normal to the surface and pointing upwards in the points $\vec{r}_i$. The last terms of Eqs. (B.1) are the projections of $\vec{h}$ in directions normal to the surface in the points P_1 and P_2. With this addition, the total action of the interaction force $\vec{h} - \left(\vec{h} \circ \vec{n}_i\right)\vec{n}_i$ is tangential to the surface. Further, we can write:

$$\vec{F}_1 = m_1\vec{g} + m_1\left(\ddot{\vec{r}}_1 \circ \vec{n}_1 - \vec{g} \circ \vec{n}_1\right)\vec{n}_1$$

$$\vec{F}_2 = m_2\vec{g} + m_2\left(\ddot{\vec{r}}_2 \circ \vec{n}_2 - \vec{g} \circ \vec{n}_2\right)\vec{n}_2$$

where $\vec{g}$ is the gravity acceleration vector, pointing downwards, and $\left(\ddot{\vec{r}}_i \circ \vec{n}_i\right)\vec{n}_i$ are the centripetal accelerations. In case of friction, the system of Eqs. (B.1) changes to:

$$m_1\ddot{\vec{r}}_1 = \vec{F}_1 + \vec{h} - \left(\vec{h} \circ \vec{n}_1\right)\left(\vec{n}_1 - \mu\vec{t}_1\right) \tag{B.2a}$$

$$m_2\ddot{\vec{r}}_2 = \vec{F}_2 - \vec{h} + \left(\vec{h} \circ \vec{n}_2\right)\left(\vec{n}_2 - \mu\vec{t}_2\right) \tag{B.2b}$$

where μ is the friction coefficient and where $\vec{t}_1$ and $\vec{t}_2$ are unit vector tangential to the surface and parallel to the instantaneous velocity of the respective masses. In parallel, the expression for $\vec{F}_1$ and $\vec{F}_2$ are generalised to:

$$\vec{F}_1 = m_1\vec{g} + m_1(\ddot{\vec{r}}_1 \circ \vec{n}_1 - \vec{g} \circ \vec{n}_1)(\vec{n}_1 - \mu\vec{t}_1) \tag{B.3a}$$

$$\vec{F}_2 = m_2\vec{g} + m_2(\ddot{\vec{r}}_2 \circ \vec{n}_2 - \vec{g} \circ \vec{n}_2)(\vec{n}_2 - \mu\vec{t}_2) \tag{B.3b}$$

Considering that the forces $\vec{F}_i$ include terms depending on the position of the masses and on the centripetal accelerations, that in turn can be written in terms of curvature radiuses R_i and of velocities, we can isolate the mass accelerations in the first member of Eqs. (B.2) and write:

$$\ddot{\vec{r}}_1 = \frac{\vec{F}_1}{m_1} + \frac{1}{m_1}\left[\vec{h} - (\vec{h} \circ \vec{n}_1)(\vec{n}_1 - \mu\vec{t}_1)\right] \tag{B.4a}$$

$$\ddot{\vec{r}}_2 = \frac{\vec{F}_2}{m_2} - \frac{1}{m_2}\left[\vec{h} - (\vec{h} \circ \vec{n}_2)(\vec{n}_2 - \mu\vec{t}_2)\right] \tag{B.4b}$$

where the forces are given by Eqs. (B.3). The interaction force we consider here is such that the distance between the masses is constant, which means that the joining vector $\vec{r}_{12} = \vec{r}_1 - \vec{r}_2$ has a constant magnitude. This constraint can be expressed in terms of the accelerations of the two points:

$$(\ddot{\vec{r}}_1 - \ddot{\vec{r}}_2) \circ (\vec{r}_1 - \vec{r}_2) + (\dot{\vec{r}}_1 - \dot{\vec{r}}_2) \circ (\dot{\vec{r}}_1 - \dot{\vec{r}}_2) = 0$$

The difference between the accelerations expressed in (B.4a) and (B.4b) is:

$$\ddot{\vec{r}}_1 - \ddot{\vec{r}}_2 = = \frac{\vec{F}_1}{m_1} - \frac{\vec{F}_2}{m_2} + \frac{m_1+m_2}{m_1 m_2}\vec{h} - \frac{1}{m_1}(\vec{h} \circ \vec{n}_1)(\vec{n}_1 - \mu\vec{t}_1) - \frac{1}{m_2}(\vec{h} \circ \vec{n}_2)(\vec{n}_2 - \mu\vec{t}_2)$$

By assuming that the force $\vec{h}$ points towards the direction $\vec{r}_{12} = \vec{r}_1 - \vec{r}_2$, i.e.:

$$\vec{h} = h\,\frac{\vec{r}_{12}}{(\vec{r}_{12} \circ \vec{r}_{12})^{1/2}} \tag{B.5}$$

we can obtain the following expression for the interaction force:

$$\vec{h} = -\vec{r}_{12}\left[\frac{m_1 + m_2}{m_1 m_2}\,\vec{r}_{12} \circ \vec{r}_{12}\right.$$

$$-\frac{(\vec{r}_{12} \circ \vec{n}_1)\left[\vec{r}_{12} \circ \left(\vec{n}_1 - \mu\vec{t}_1\right)\right]}{m_1}$$

$$\left.-\frac{(\vec{r}_{12} \circ \vec{n}_2)\left[\vec{r}_{12} \circ \left(\vec{n}_2 - \mu\vec{t}_2\right)\right]}{m_2}\right]^{-1}$$

$$\left[\vec{r}_{12} \circ \left(\frac{\vec{F}_1}{m_1} - \frac{\vec{F}_2}{m_2}\right) + \dot{\vec{r}}_{12} \circ \dot{\vec{r}}_{12}\right] \tag{B.6}$$

Eq. (B.6) shows that $\vec{h}$ depends on the positions and velocities of the masses. It is convenient to rewrite it in the following simplified form:

$$\vec{h} = \Gamma\ \vec{r}_{12}$$

where Γ is defined implicitly. With this in mind, the total forces acting on the masses m_1 and m_2 can be given the expressions:

$$\vec{F}_{1,tot} = \vec{F}_1 + \Gamma\vec{R}_{1T} \tag{B.7a}$$

$$\vec{F}_{2,tot} = \vec{F}_2 - \Gamma\vec{R}_{2T} \tag{B.7b}$$

where $\vec{F}_1$ and $\vec{F}_2$ are given by Eqs. (B.3) and where

$$\vec{R}_{1T} = \vec{r}_{12} - (\vec{r}_{12} \circ \vec{n}_1)\left(\vec{n}_1 - \mu\vec{t}_1\right) \tag{B.8a}$$

$$\vec{R}_{2T} = \vec{r}_{12} - (\vec{r}_{12} \circ \vec{n}_2)\left(\vec{n}_2 - \mu\vec{t}_2\right) \tag{B.8b}$$

Considering Eqs. (B.2), (B.7) and (B.8), we can write the equations of motion for the various components in the form:

$$m_1\ddot{x}_1 = F_{1x} + \Gamma R_{1Tx} \tag{B.9a}$$

$$m_1\ddot{y}_1 = F_{1y} + \Gamma R_{1Ty} \tag{B.9b}$$

$$m_2\ddot{x}_2 = F_{2x} - \Gamma R_{2Tx} \tag{B.9c}$$

$$m_2\ddot{y}_2 = F_{2y} - \Gamma R_{2Ty} \tag{B.9d}$$

If we introduce the arrays $\boldsymbol{p}$ and $\boldsymbol{b}$ such that:

$$\boldsymbol{p^T} = [x_1, y_1, x_2, y_2] \tag{B.10}$$

$$\boldsymbol{b^T} = [F_{1x} + \Gamma R_{1Tx}, \quad F_{1y} + \Gamma R_{1Ty},$$

$$F_{2x} - \Gamma R_{2Tx}, F_{2y} - \Gamma_{12} R_{2Ty}] \tag{B.11}$$

the system of Eqs. (B.9) can be written in the compact form:

$$\boldsymbol{A\ddot{p} = b} \tag{B.12}$$

where $\boldsymbol{A}$ is a $4x4$ diagonal matrix with: $A_{11} = m_1,\ A_{22} = m_1,\ A_{33} = m_2,\ A_{44} = m_2$. Eventually, the system (B.12) can be turned into a system of first-order differential equations as:

$$\boldsymbol{\dot{p} = v} \tag{B.13a}$$

$$\boldsymbol{\dot{v} = A^{-1}b} \tag{B.13b}$$

System (B.13) is suitable for a solution computed by means of Runge-Kutta numerical methods.

The theory just described is first tested through particular cases admitting an analytical solution for the motion of the two-mass system. These solutions allow us to find an exact form for the interaction force given in (B.6).

Case 1

The first case we propose is a constant velocity circular motion on a concave sphere described in a Cartesian reference system by the equation:

$$z = R - \sqrt{R^2 - x^2 - y^2} \qquad z < z_{max} \leq R \tag{B.14}$$

where R is the sphere radius.
A particle on a spherical surface moves along a horizontal circular trajectory if it is posed at a distance $r = R \sin\vartheta_0$ from the vertical axis and pushed with an initial horizontal velocity v_0 equal to:

$$v_0 = \sqrt{gR \sin\vartheta_0 \tan\vartheta_0} \tag{B.15}$$

where ϑ_0 is the slope of the plane tangent in the particle initial position. Notice that the kinetic energy needed to keep the motion on the horizontal circle grows with ϑ_0.
Here, we impose that two masses have initial velocities given by the expression (B.15), are initially placed on a horizontal circumference of radius $r = R \sin\vartheta_0$ and are separated by the angular shift φ_0.
Under these conditions, we expect that, independently from the choice of φ_0, the particles will spin on the same plane keeping their initial velocities and shift constant over time. The equations for the displacement components are given by:

$$x_1(t) = r \sin\omega t$$
$$y_1(t) = r \cos\omega t$$

$$x_2(t) = r \sin(\omega t + \varphi_0)$$
$$y_2(t) = r \cos(\omega t + \varphi_0)$$

with $\omega = v_0/r$. Since the two masses move like they would move if they were free individual systems, the interaction force is expected to be identically zero.

We set up a simulation case with the following parameters. We took a spherical unit-radius surface and two equal masses ($m_1 = m_2 = m$) at the initial positions $P_{01} = (\vartheta_0, 0)$ and $P_{02} = (\vartheta_0, \varphi_0)$, where $\vartheta_0 = 23.6°$ and the phase shift $\varphi_0 = \pi/2$. The initial velocities were correspondingly set to $V_{01} = (0, v_0)$ and $V_{02} = (0, -v_0)$, with v_0 evaluated through Eq. (B.15). We ran the numerical simulations for $t = 5\,T$, where $T = 2\pi r/v_0$ is the motion period. The difference of the numerical and analytical solution is very small. For example, the discrepancy for horizontal displacement $x(t)$ normalized over the motion radius r results to be confined to the order of 10^{-9}. Likewise, from our computations, the interaction force normalized over mg turns out to be in the range of 10^{-13} which is practically zero, as it should be.

The second case we propose regards a system of particles on a sphere where the interaction differs from zero. We set the masses m_1 and m_2 at different heights on the sphere in the same vertical plane. With no loss of generalization, we take the initial horizontal positions in $P_{01} = (R \sin\vartheta_1, 0)$ and $P_{02} = (R \sin\vartheta_2, 0)$. It can be shown that the masses move uniformly on the circles respectively of

radius $r_1 = R_1 \sin\vartheta_1$ and $r_2 = R_2 \sin\vartheta_2$, if their initial velocities are $(\dot{\vec{r}}_1)_0 = (0, v_1, 0)$ and $(\dot{\vec{r}}_2)_0 = (0, v_2, 0)$, with v_1 and v_2 satisfying the expressions:

$$v_1^2 = gR \sin\vartheta_1 \tan\vartheta_1$$

$$\left(1 + (\cos\vartheta_1 - \cos\vartheta_2)\frac{m_2 \sin\vartheta_2}{m_1 \sin\vartheta_1\vartheta + m_2 \sin\vartheta_2 \cos\vartheta_2}\right) \quad \text{(B.16a)}$$

$$v_2^2 = gR \sin\vartheta_2 \tan\vartheta_2$$

$$\left(1 - (\cos\vartheta_1 - \cos\vartheta_2)\frac{m_1 \sin\vartheta_1}{m_1 \sin\vartheta_1 \cos\vartheta_1 + m_2 \sin\vartheta_2 \cos\vartheta_2}\right) \quad \text{(B.16b)}$$

It is worth pointing out that the masses have the same angular velocity, given by:

$$\omega^2 = \frac{g}{R}\,\frac{m_1 \sin\vartheta_1 + m_2 \sin\vartheta_2}{m_1 \sin\vartheta_1 \cos\vartheta_1 + m_2 \sin\vartheta_2 \cos\vartheta_2} \quad \text{(B.17)}$$

Let's suppose that $\vartheta_1 < \vartheta_2$, so that particle 2 moves above particle 1. It is worth observing that if the two particles were free to move (with no binding) the speeds to sustain the horizontal circular trajectories would be given by Eq. (B.15) and would be different from one another. Namely, the speed of particle 1 would be smaller than the velocity v_1 given in (B.16a) and the speed of particle 2 would be larger than v_2 of eq. (B.16b). Hence the interaction in the coupled system has the effect of constraining the masses to the same angular speed pushing the lower mass and slowing down the upper mass.
The analytical solution for the motion of the masses is:

$$x_1(t) = R \sin\vartheta_1 \cos\omega t$$

$$y_1(t) = R \sin\vartheta_1 \sin\omega t$$

$$x_2(t) = R \sin\vartheta_2 \cos\omega t$$

$$y_2(t) = R \sin\vartheta_2 \sin\omega t$$

It can be shown that the interaction force has a constant magnitude given by the following exact expression:

$$h = g\,\frac{|\cos\theta_1 - \cos\theta_2|}{\cos((\vartheta_2 - \vartheta_1)/2)}$$

$$\frac{m_1 m_2 \sin\theta_1 \sin\theta_2}{m_1 \sin\vartheta_1 \cos\theta_1 + m_2 \sin\theta_2 \cos\theta_2} \quad \text{(B.18)}$$

where h is defined in Eq. (B.6). It is worth observing that h does not depend on the sphere radius R. Notice further that if one of the two masses is set at the bottom of the sphere (for example if $\vartheta_1 = 0$), the mass does not move, while the other one spins as it were free, with v_2 taking the form seen in Eq. (B.15).

In Figure B.1 we display the values of h given by Eq. (B.18), in the case of two equal masses ($m_1 = m_2 = m$) normalized to mg, as a function of ϑ_1 and ϑ_2. In virtue of its definition (Eq.(B.4)), when h is positive, it means that mass 1 is pushed away by mass 2 (rejected), which is a reciprocal action. In our case, h as given by Eq. (B.18) is always positive, and hence the interaction is repulsive in character. To explain this, one should consider that mass 1 rotates at a speed higher than the corresponding free particle. A free particle with the same speed would then tend to move outward from the rotation axis and therefore to climb up to higher values of z. Likewise, the upper mass, if free, would tend to move downward. The interaction force opposes this trend and keeps them at their own level pushing them away from one other. Looking at the contour plot of Figure B.1, one sees that, on the bisecting line where $\vartheta_1 = \vartheta_2$, the magnitude of h is zero, because the two-mass system degenerates to a single mass. Expectedly, the plot is symmetric with respect to the bisecting line.

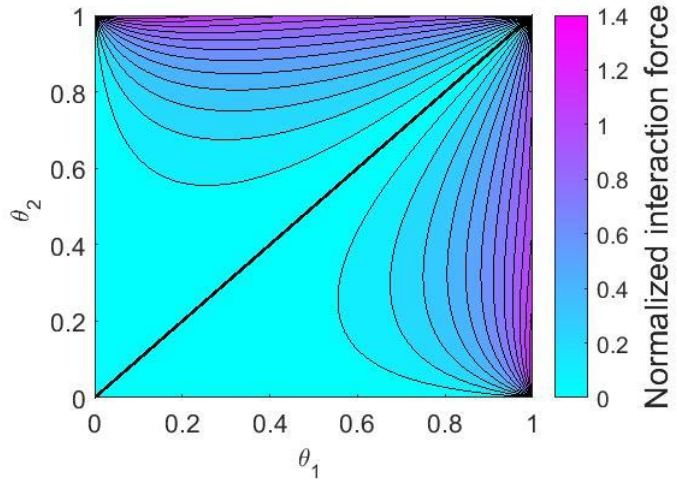

Figure B.1 Interaction force between two equal masses spinning at the same angular velocity but at different heights on a sphere, normalized over mg, as a function of the angles ϑ_1 and ϑ_2 in the range $0{:}\,\pi/2$. Angles are measured in $\pi/2$ units. Contour lines are spaced by 0.1 The black thick line represents the bisecting line where h is zero.

Notice that h results to be a multivalued function in the nodes ($\vartheta_1 = 0$, $\vartheta_2 = \pi/2$) and ($\vartheta_1 = \pi/2$, $\vartheta_2 = 0$), where its value ranges from 0 to $mg\sqrt{2}$. Also in the node ($\vartheta_1 = \pi/2$, $\vartheta_2 = \pi/2$) it is undefined and takes on values in the range from 0 to mg. Figure B.2 shows the contour plot of h for a two-different-mass system. The masses are $m_1 = (1-k)m$ and $m_2 = (1+k)m$, where m is the average mass and k is the mass unbalance coefficient. Looking at the graph, one can see that the bisecting line is still a locus of zero values, but not a symmetry line. It can be shown that in the bottom right corner the function values range from 0 to $mg\sqrt{2}\,(1+k)$, in the upper right corner they are found in the interval from 0 to $mg\,(1+k)$, while in the upper left corner, the interval of variation is between 0 and $mg\sqrt{2}\,(1-k^2)$.

In the numerical simulations, we suppose the initial horizontal positions of the two equal masses to be in $P_{01} = (\vartheta_1, 0)$ and $P_{02} = (\vartheta_2, 0)$ on a unit-radius sphere with $\vartheta_1 = 17.5°$ and $\vartheta_2 = 23.6°$. According to the Eq. (B.17), the period of rotation around the vertical axis is slightly larger (by a factor 7 10^{-3}) than the corresponding period of the free particle 2 (see the previous example). From Eq. (B.18), the interaction force turns out to be quite weak, having the value h/mg = 6.9 10^{-3}. We compute the numerical solution for $t = 5T$, where $T = 2\pi/\omega$.

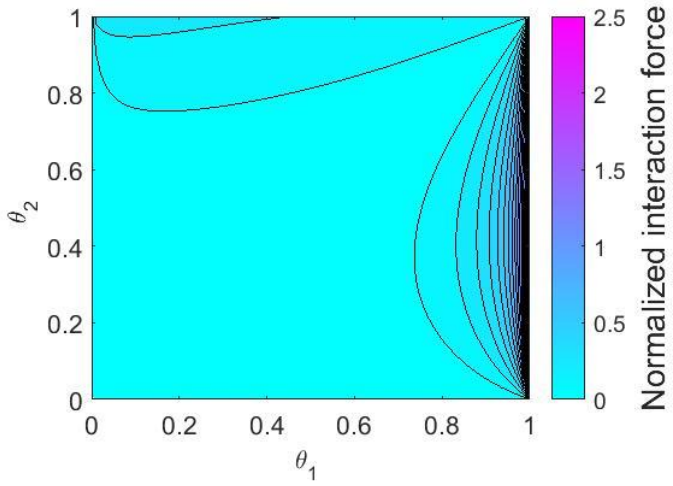

Figure B.2 Interaction force between two different masses spinning with the same angular velocity and at different heights on a sphere, normalized to mg, where m is the average mass of the particles (unbalance coefficient $k = 0.82$). Angles ϑ_1 and ϑ_2 are measured in $\pi/2$ units. Contour lines are spaced by 0.1.

The differences between the numerical and analytical positions on the x axis, i.e. $x(t)$, normalized to the radiuses of the circular motion, are in the order of 10^{-6}. Furthermore, the difference between the interaction force estimated through the RK4 scheme and the analytical expression (B.18) are in the range of 10^{-3}, which suggests that the RK4 scheme provides satisfactory results.

Case 2

The next theoretical case is the motion of two equal masses that start from rest on a spherical surface from the same height. Let's suppose that $m_1 = m_2 = m$, and that the initial positions on the sphere can be described by the colatitude ϑ_0 and the longitude φ_0 as follows:

$$P_{10} = (R\sin\vartheta_0\cos\varphi_0, -R\sin\vartheta_0\sin\varphi_0, R(1-\cos\vartheta_0))$$
$$P_{20} = (R\sin\vartheta_0\cos\varphi_0,\ \ R\sin\vartheta_0\sin\varphi_0, R(1-\cos\vartheta_0))$$

where R is the radius. Due to the perfect symmetry of the problem with respect to the vertical plane $y = 0$, we expect that the two masses have equal latitude ϑ and opposite longitude φ at any time. This means that the instantaneous position of the two masses are:

$$P_1 = (R\sin\vartheta\cos\varphi, -R\sin\vartheta\sin\varphi, R(1-\cos\vartheta))$$

$$P_2 = (R\sin\vartheta\cos\varphi,\ \ R\sin\vartheta\sin\varphi, R(1-\cos\vartheta))$$

and their distance is:

$$d = 2R \sin\vartheta \sin\varphi$$

Since d does not change in time, it implies that the product $\sin\vartheta \sin\varphi$ is a constant of the system motion.
The center of mass (CoM) of this system has the position:

$$P_{CM} = (R \sin\vartheta \cos\varphi, 0, R(1 - \cos\vartheta))$$

and its distance from the sphere center is $R_{CM} = R\sqrt{1 - (\sin\vartheta \sin\varphi)^2}$. Because the product $\sin\vartheta \sin\varphi$ is a motion constant, it follows that during the motion the CoM moves along an arc of radius R_{CM}. If we call γ the angle formed by the radius R_{CM} with the vertical axis at the time t, we can use it as a coordinate describing the instantaneous position of the CoM. It is easy to see that the link between γ and the latitude ϑ is:

$$R_{CM} \cos\gamma = R \cos\vartheta \tag{B.19}$$

Considering that only the gravity forces contribute to the momentum calculated with respect to the center of the sphere, it can be shown that the CoM dynamics is governed by the pendulum equation:

$$\ddot{\gamma} = -\frac{g}{R_{CM}} \sin\gamma \tag{B.20}$$

which is cyclic with a period equal to:

$$T = 4\sqrt{\frac{R_{CM}}{g}} \int_0^{\frac{\pi}{2}} \frac{d\alpha}{\sqrt{1 - \sin^2\left(\frac{1 - \cos\gamma_0}{2}\right)\sin^2\alpha}} \tag{B.21}$$

where γ_0 is the initial position of the center of mass and where angles are measured in radians. In Figure B.3, the oscillation period is displayed as a function of the initial colatitude ϑ_0 and longitude φ_0 in the range $0{:}\,\pi/2$. Values are normalized over $\frac{\pi}{2}\sqrt{\frac{R}{g}}$ that is the expected period for small latitude angles. It is found that the scaled T is almost constant and close to one around the origin. On the contrary, when ϑ_0 is close to $\pi/2$, the variations of φ strongly affect the period. Further, the period tends to zero when also φ_0 approaches $\pi/2$ since the oscillation radius R_{CM} goes to zero.

Passing from γ to the Cartesian coordinates of the CoM and of the masses is straightforward. The Cartesian CoM coordinates are given by:

$$x_{CM}(t) = R_{CM} \sin\gamma(t)$$

$$y_{CM}(t) = 0$$

$$z_{CM}(t) = R - R_{CM} \cos\gamma(t)$$

and the coordinates of the masses are:

$$x_1(t) = x_2(t) = x_{CM}(t)$$
$$y_1(t) = -d/2 \qquad y_2(t) = d/2$$
$$z_1(t) = z_2(t) = z_{CM}(t)$$

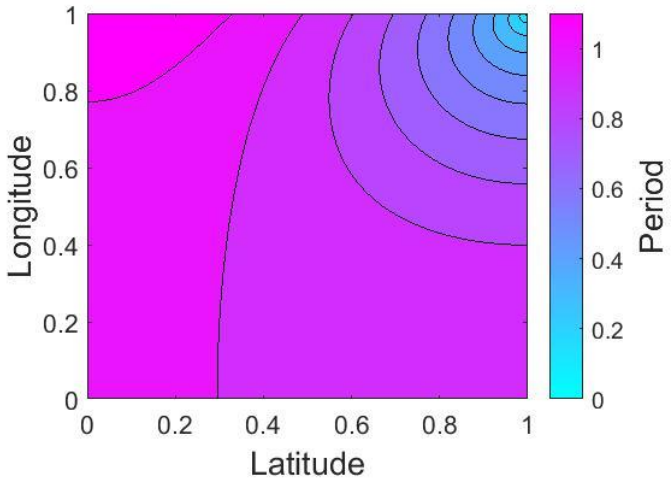

Figure B.3 Period estimated through Eq. (B.21), scaled to $\frac{\pi}{2}\sqrt{\frac{R}{g}}$ as a function of the initial latitude ϑ_0 and longitude φ_0. Angles are in the range $0: \pi/2$ and are measured in $\pi/2$ units.

The interaction force calculated through the Eq. (B.5) can be written as:

$$h(t) = \frac{mgdR_{CM}}{R^2} \frac{\frac{3}{2}\cos\gamma(t) - \cos\gamma_0}{1 - \frac{d^2}{4R^2}} \tag{B.22}$$

In terms of colatitude and longitude, the above expression turns out to be:

$$h(t) = mg \sin\vartheta(t) \sin\varphi(t) \frac{3\cos\vartheta(t) - 2\cos\vartheta_0}{1 - (\sin\vartheta(t)\sin\varphi(t))^2} \tag{B.23}$$

The solution of the problem can only be found numerically by solving Eq. (B.20) providing $\gamma(t)$, and then using the geometrical relation (B.19) and the invariance of the distance d to find ϑ and φ. There are, however, some properties that can be deduced analytically. For example, the interactive repulsive force $h(t)$ oscillates between a minimum and maximum value that can be written as:

$$h_{min} = \frac{mg\ \sin\vartheta_0\ \sin\varphi_0}{1 - \sin^2\vartheta_0\ \sin^2\varphi_0}\cos\vartheta_0 \tag{8.24}$$

and

$$h_{max} = \frac{mg\ \sin\vartheta_0\ \sin\varphi_0}{1-\sin^2\vartheta_0\ \sin^2\varphi_0}\left(3\sqrt{1 - \sin^2\vartheta_0\ \sin^2\varphi_0} - 2\cos\vartheta_0\right) \tag{B.25}$$

One can observe that h does not depend on the radius R, and scales as mg. In Figure B.4 we show a contour plot of h_{max}/mg as a function of the initial colatitude and longitude of the masses. The plot suggests that h_{max} grows larger and larger when ϑ_0 and φ_0 approach $\pi/2$, and provides an example where the interaction force can largely dominate on the weight of the masses.

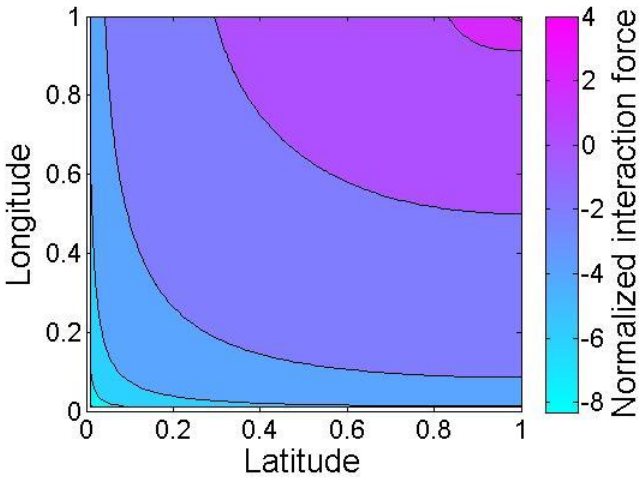

Figure B.4 Maximum interaction force (in logarithmic scale) for two equal masses oscillating in parallel and at the same height on a sphere, scaled to mg, as a function of the initial colatitude and longitude. Angles are in the range 0: $\pi/2$ and are measured in $\pi/2$ units.

The numerical solution of the Eq. (B.20) has been computed through an RK4 scheme. It is taken here as the reference solution against which we compare the solutions of Eqs. (B.13) for the coupled system. On a unit-radius sphere, we select the colatitude $\vartheta_0 = 24.35°$ and the longitude $\varphi_0 = 14.04°$. Initial velocities are set to zero. The oscillation period estimated through Eq. (B.21) and by the numerical solution of the coupled system leads to almost the same value with a relative error in the order of 10^{-5}. Computations are carried out for 5 periods.

The absolute differences between the values of $x(t)$ computed numerically and analytically, normalized to R_{CM}, are equal for both masses, in the order of 10^{-12}. The interaction force h oscillates between the values 0.092 mg and 0.118 mg, as is clear in Figure B.5 where the time history of the interaction force of the numerical solutions is shown. Differences between the numerical and analytical solutions are very small, in the order of 10^{-12}.

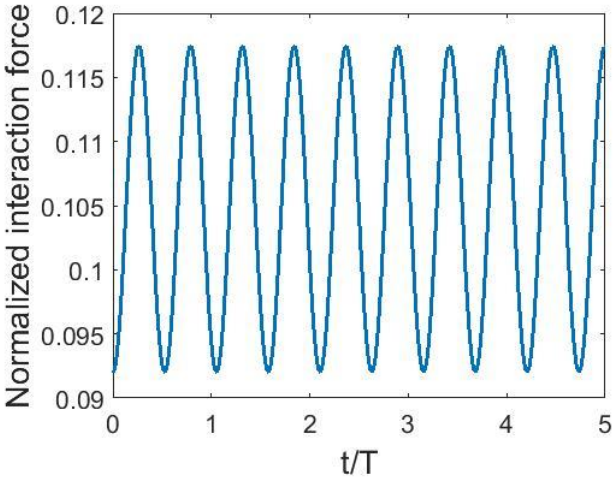

Figure B.5 Interaction force, normalized to mg, vs. time for the numerical solution of the coupled masses problem.

The previous case is also treated considering the presence of the friction force acting on the system. In this case, the CoM dynamics is represented by the equation:

$$\ddot{\gamma} = -\frac{g}{R_{CM}}\sin\gamma - \mu\frac{|\dot{\gamma}|}{R_{CM}}(R\dot{\gamma}^2 + \frac{gR}{R_{CM}}\cos\gamma)$$

The interaction force is independent of basal friction but depends on the particles velocities. Hence, its general trend is not given by Eq. (B.23) since we expect h to decrease as the particles decelerate under the effect of friction. The minimum value is still given analytically by Eq. (B.24), as in the frictionless case, but the maximum value depends on the maximum velocity value that can be obtained only numerically.

To illustrate this case, we set the masses at the same initial positions as for the no-friction example and we use a friction coefficient $\mu = 0.02$. We obtain differences between the $x(t)$ of 10^{-2}, proving a loss of accuracy of the numerical methods with the presence of a dissipative force such as basal friction. The interaction force variations vs. time estimated through the numerical solutions are shown in Figure B.6. As can be easily noticed the first oscillation is similar to the no-friction case since the velocities are quite similar. As the effect of damping becomes more evident, the interaction force clearly decreases reaching a constant value when the particles velocities are close to zero. The differences between the reference and numerical solutions are in the order of 10^{-3}.

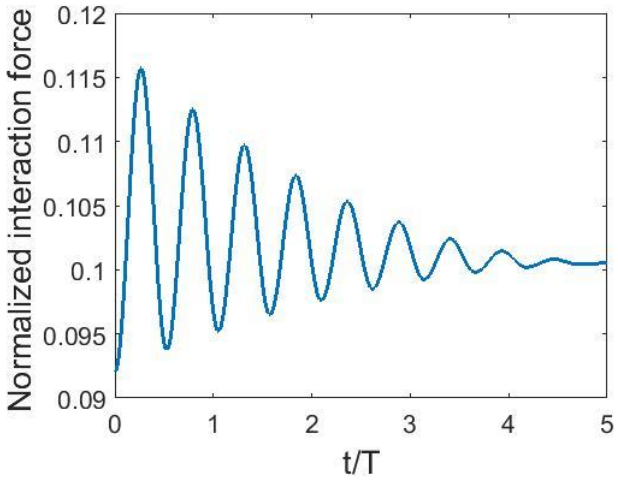

Figure B.6 Interaction force, scaled to mg, vs. time for the numerical solution of the coupled masses moving on a rough surface (friction coefficient $\mu = 0.02$).

APPENDIX C

In this Appendix, we will show the fourth-order Runge-Kutta numerical scheme used to solve the systems of differential equations described in this work. For the sake of clarity, we will illustrate only the case of two coupled masses that was treated in the Appendix B, since the generalization to systems with N point masses is straightforward.

Runge-Kutta methods were introduced to solve ODE problems that can be given the general form:

$$\dot{\boldsymbol{u}} = \boldsymbol{A}(\boldsymbol{u}, t) \tag{C.1}$$

If $\boldsymbol{u}$ and $\boldsymbol{A}$ denote M-component vectors depending on the time t, the above expression (C.1) represents a system of M first-order differential equations that can be also put in some equivalent alternative form, such as

$$\dot{u}_m = A_m(\boldsymbol{u}, t) \quad 1 \leq m \leq M \tag{C.2a}$$

or

$$\dot{u}_m = A_m(u_1, u_2, \dots, u_M, t) \quad 1 \leq m \leq M \tag{C.2b}$$

If one introduces the vector $\boldsymbol{v}^n$ as an approximation of the unknown vector $\boldsymbol{u}$ at the time $t_n = n\Delta t$, the problem of solving the ODE (C.1) reduces to computing the sequence of the approximating vectors $\boldsymbol{v}^n$ from the initial time t_0 up to the final time t_{end}. Runge-Kutta methods use a recursive procedure to compute $\boldsymbol{v}^{n+1}$ starting from $\boldsymbol{v}^n$, which is made through a series of steps. The fourth-order method we denoted as RK4 and we adopted in this thesis, makes use of four intermediate steps. It introduces the intermediate temporary vectors $\widetilde{\boldsymbol{v}}^{p,n}$ and $\widetilde{\boldsymbol{A}}^{p,n}$ (p=1,2,3,4) according to the following scheme:

$$\widetilde{\boldsymbol{v}}^{1,n} = \boldsymbol{v}^n \tag{C.3.1a}$$

$$\widetilde{\boldsymbol{A}}^{1,n} = \boldsymbol{A}(\widetilde{\boldsymbol{v}}^{1,n}, t_n) \tag{C.3.1b}$$

$$\widetilde{\boldsymbol{v}}^{2,n} = \boldsymbol{v}^n + \frac{1}{2}\Delta t \widetilde{\boldsymbol{A}}^{1,n} \tag{C.3.2.a}$$

$$\widetilde{\boldsymbol{A}}^{2,n} = \boldsymbol{A}(\widetilde{\boldsymbol{v}}^{2,n}, t_n + \frac{1}{2}\Delta t) \tag{C.3.2b}$$

$$\widetilde{\boldsymbol{v}}^{3,n} = \boldsymbol{v}^n + \frac{1}{2}\Delta t \widetilde{\boldsymbol{A}}^{2,n} \tag{C.3.3a}$$

$$\widetilde{\boldsymbol{A}}^{3,n} = \boldsymbol{A}(\widetilde{\boldsymbol{v}}^{3,n}, t_n + \frac{1}{2}\Delta t) \tag{C.3.3b}$$

$$\widetilde{\boldsymbol{v}}^{4,n} = \boldsymbol{v}^n + \Delta t \widetilde{\boldsymbol{A}}^{3,n} \tag{C.3.4a}$$

$$\widetilde{\boldsymbol{A}}^{4,n} = \boldsymbol{A}(\widetilde{\boldsymbol{v}}^{4,n}, t_{n+1}) \tag{C.3.4b}$$

Eventually, the next element of the sequence $\boldsymbol{v}^{n+1}$ is computed through the formula:

$$\boldsymbol{v}^{n+1} = \boldsymbol{v}^n + \frac{1}{6}\left(\widetilde{\boldsymbol{A}}^{1,n} + 2\,\widetilde{\boldsymbol{A}}^{2,n} + 2\,\widetilde{\boldsymbol{A}}^{3,n} + \widetilde{\boldsymbol{A}}^{4,n}\right) \tag{C.3.5}$$

The set of expressions (C.3) is the basic recursive scheme of the method RK4 ensuring a fourth-order accuracy of the solution and we used it for all the cases treated in this thesis. The number of elements M of the vectors $\boldsymbol{u}$ and $\boldsymbol{A}$ as well as of all the vectors involved in the discretization formulas depends

on the specific problem at hand. In our cases, $M = 4N$, where N is the number of point-masses of the system.

For the system consisting of two coupled masses given in the Appendix B, the following mapping can be considered for $\boldsymbol{u}$:

$$\boldsymbol{u} = [x_1, x_2, \dot{x}_1, \dot{x}_2, y_1, y_2, \dot{y}_1, \dot{y}_2] \tag{C.4}$$

where (x_1, y_1) and $(\dot{x}_1, \dot{y}_1)$ are the horizontal coordinates and velocity components of the first mass and likewise (x_2, y_2) and $(\dot{x}_2, \dot{y}_2)$ are the corresponding quantities for the second mass. Considering the definition (C.4), one can deduce the expression for $\boldsymbol{A}$. Some of the components of $\boldsymbol{A}$ are very easy to write, while others can be derived after cumbersome manipulations. At the first stage, $\boldsymbol{A}$ can be given in the form:

$$\boldsymbol{A} = [u_3, u_4, A_3, A_4, u_7, u_8, A_{7,} A_8] \tag{C.5}$$

where some components, namely A_1, A_2, A_5 and A_6 have been given an explicit expression. The expressions for the others can be obtained by writing the equation of motions of the masses in terms of the components of the vector $\boldsymbol{u}$ according to the definition (C.4). We will not provide all such expressions, but we will illustrate how to derive the component A_3 as an example. To this purpose, we observe that the equation:

$$\dot{u}_3 = A_3(\boldsymbol{u}, t)$$

is equivalent to:

$$\ddot{x}_1 = A_3(\boldsymbol{u}, t)$$

which means that one can deduce A_3 from the *x*-component of the equation of motion of the first mass given in (B.1a):

$$m_1\ddot{x}_1 = F_{1,x} + h_x - \left(\vec{h} \circ \vec{n}_1\right) n_{1,x}$$

or from the one given in (B.2a), where friction is accounted for:

$$m_1\ddot{x}_1 = F_{1,x} + h_x - \left(\vec{h} \circ \vec{n}_1\right)\left(n_{1,x} - \mu t_{1,x}\right)$$

All the variables in the r.h.s. of the above formula can be expressed in terms of the components of the vector $\boldsymbol{u}$. For instance, by using the definition (A.2), one can write for the vector $\vec{n}_1$:

$$\vec{n}_1 = \frac{1}{\left(1 + f_{x_1}^2(x_1, y_1) + f_{y_1}^2(x_1, y_1)\right)^{\frac{1}{2}}}\left[-f_{x_1}(x_1, y_1), f_{y_1}(x_1, y_1), 1\right]$$

which is an expression containing the position coordinates of the first mass (x_1, y_1). In virtue of the mapping (C.4), it is then easy to write the expression we need for $n_{1,x}$, that is:

$$n_{1,x} = \frac{-f_{u_1}(u_1, u_5)}{\left(1 + f_{u_1}^2(u_1, u_5) + f_{u_5}^2(u_1, u_5)\right)^{\frac{1}{2}}}$$

Following the same procedure, since the tangential vector $\vec{t}_1$ is given by:

$$\vec{t}_1 = \frac{1}{\left(\dot{x}_1{}^2 + \dot{y}_1{}^2 + \left(\dot{x}_1 f_{x_1}(x_1, y_1) + \dot{y}_1 f_{y_1}(x_1, y_1)\right)^2\right)^{\frac{1}{2}}}\left[\dot{x}_1, \dot{y}_1, \dot{x}_1 f_{x_1}(x_1, y_1) + \dot{y}_1 f_{y_1}(x_1, y_1)\right]$$

the *x*-component $t_{1,x}$ can be rewritten as:

$$t_{1,x} = \frac{u_3}{\left({u_3}^2 + {u_7}^2 + \left(u_3 f_{u_1}(u_1, u_5) + u_7 f_{u_5}(u_1, u_5)\right)^2\right)^{\frac{1}{2}}}$$

The formulas deduced for $n_{1,x}$ and for $t_{1,x}$ can be used to write the proper expression for A_3. However, to obtain the final form for A_3, also the expressions for $F_{1,x}$, for $\vec{n}_1$ and for the interaction vector $\vec{h}$ have to be derived. They can be obtained from the formulas of the Appendix B by mapping the horizontal positions and velocities of the masses to the new variables $u_m (1 \leq m \leq 8)$ through the correspondence rule (C.4). Likewise, all the components of the vector $\boldsymbol{A}$ can be written in the appropriate way for the application of the RK4 procedure.

References

Abramson, L.W., Lee, T.S., Sharma, S., Boyce, G.M. (2001). *Slope stability and stabilization*. New York: John Wiley and Sons.

Bortolucci, E. (2001). *Modelli dinamici di frane e dei maremoti indotti*. PhD Thesis, Bologna: University of Bologna.

Boschi, E., Guidoboni, E., Ferrari, G., Mariotti, D., Valensise, G., Gasperini, P. (2000). *Catalogue of strong Italian earthquakes from 461 B.C. to 1997*. Ann. Geophys., 43: 609-868.

Bosman, A., Bozzano, F., Chiocci, F., Mazzanti, P. (2006). *The 1783 Scilla tsunami: evidences of a submarine landslide as a possible cause*. Geophys. Res. Abstr., 10558.

Bozzano, F., Lenti, L., Martino, S., Montagna, A., Paciello, A. (2011). *Earthquake triggering of landslides in highly jointed rock masses: Reconstruction of the 1783 Scilla rock avalanche (Italy).* Geomorph., 129: 294-308.

Brunsden D. (1985) *Landslide types, mechanisms, recognition, identification.* In: Morgan CS (ed.) Landslides in the South Wales Coalfield, Proceedings Symposium, 1–3 April, 1985. The Poly. of Wales, 19–28.

Caratori Tontini, F., Cocchi, L., Muccini, F., Carmisciano, C., Marani, M., Bonatti, E., Ligi, M., Boschi, E. (2010). *Potential-field modelling of collapse-prone submarine volcanoes in the southern Tyrrhenian Sea (Italy)*. Geophys. Res. Lett., 37: L03305, doi:10.1029/2009GL041.

Cas, R.A.F., Wright, J.V. (1993). *Volcanic Successions. Modern and Ancient, A geological approach to processes, products and successions*. Chapman & Hall, London, UK.

Cocchi, L., Caratori Tontini, F., Muccini, F., Marani, M.P., Bortoluzzi, G., Carmisciano, C. (2009). *Chronology of the transition from a spreading ridge to an accretional seamount in the Marsili backarc basin (Tyrrhenian Sea).* Terra Nova, 21: 369-374.

Coe, J.A., Ellis, W.L., Godt, J.W., Savage, W.Z., Michael, J.A., Kibler, J.D., Powers P.S., Lidke, D.J., Debray, S. (2003). *Seasonal movement of the Slumgullion landslide determined from GPS surveys and field instrumentation, July 1998-March 2002*. Eng. Geol., 68: 67-101.

Cornforth, D. (2005). *Landslides in practice: investigation, analysis and remedial/ preventive options in soils.* New York: John Wiley and Sons.

Cristescu, N.D. (2000). *A model of stability of slopes*, in Slope Stability 2000, D.V. Griffiths, G.A. Fenton, d T.R. Martin (Eds.), Proc. GeoDenver 2000, August 5-8, 2000, Denver, Colorado, Geotechnical Special Publication N.101, 86-98.

Cruden, D.M., Varnes, D.J. (1996). *Landslide types and processes.* Special Report, Transportation Research Board, National Academy of Sciences, 247:36-75.

D'Alessandro, A., Mangano, G., D'Anna, G. (2012). *Evidence of persistent seismo-volcanic activity at Marsili seamount*. Ann. Geophys., 55: 213-214.

Davies, H.L., Davies, J.M., Perembo, R.C.B., Lus, W.Y. (2003). *The Aitape 1998 Tsunami: Reconstructing the Event from Interviews and Field Mapping.* Pure Appl. Geophys., In: Bardet JP.,

Imamura F., Synolakis C.E., Okal E.A., Davies H.L. (eds) Landslide Tsunamis: Recent Findings and Research Directions. Pageoph Topical Volumes. Birkhäuser, Basel.

De Lorenzo, A. (1873). *Memorie da servire alla storia sacra e civile di Reggio e delle Calabrie.* Reggio Calabria, Tipografia Siclari.

Dikau, R., Brunsden, D., Schrott, L., Ibsen, M.L. (1996). *Landslide recognition: identification, movement and causes.* Chichester, UK: John Wiley and Sons.

Dutykh, D., Dias, F. (2009). *Tsunami generation by dynamic displacement of seabed due to dip-slip faulting.* Math.Comp.Simul., 80: 837-848.

Fagents, S.A., Gregg, T.K.P., Lopes, R.M.C. (2013). *Modelling volcanic processes. The physics and mathematics of volcanism.* Cambridge University Press, Cambridge, UK.

Florio, G., Fedi, M., Cella, F. (2011). *Insights on the spreading of the Tyrrhenian Sea from the magnetic anomaly pattern.* Terra Nova, 23: 127-133.

Fritz, H.M., Fahad, M., Jeseon, Y. (2009). *Lituya bay landslide impact generated mega tsunami 50th anniversary.* Pure Appl. Geophys. 166: 153-175.

Furuya, G., Sassa, K., Hiura, H., Fukuoka, H. (1999). *Mechanism of creep movement caused by landslide activity and underground erosion in crystalline schist, Shikoku Island, southwestern Japan.* Eng. Geol., 53: 311-325.

Gao, J. (1993). *Identification of topographic settings conductive to landslide from DEM in Nelson Country.* Earth Surf. Proc. Land., 18: 579-591.

Gerardi, F., Barbano, M.S., De Martini, P.M., Pantosti, D. (2008). *Discrimination of tsunami sources on the basis of historical data in eastern Sicily and southern Calabria.* Bull. Seismol. Soc. Am., 98: 2795-2805.

Graziani, L., Maramai, A., Tinti, S. (2006). *A revision of the 1783–1784 Calabrian tsunamis.* Nat. Hazards Earth Syst. Sci., 6: 1053-1060.

Grosse, P., van Wyk de Vries, B., Petrinovic, I.A., Euillades, P.A., Alvarado, G.E. (2009). *Morphometry and evolution of arc volcanoes*. Geology., 7: 651-654.

Gupta, R.P., Joshi, B.C. (1990). *Landslide hazard zoning using the GIS approach - a case study from the Ramganga Catchment, Himalayas*. Eng. Geol., 28: 119-131.

Hampton, M.A., Lee, H.J., Locat, J. (1996). *Submarine landslides*. Rev. Geophys., 34: 33-59.

Harbitz, C.B. (1992). *Model simulations of tsunamis generated by the Storegga slides*. Mar. Geol., 105: 1-21.

Harp, E.L., Jibson, R.W. (1996). *Landslides triggered by the 1994 Northridge, California earthquake*. Bull. Seism. Soc. Am., 86: 319-332.

Harp, E.L., Wilson, R.C., Wieczorek, G.F. (1981). *Landslides from the February 4, 1976, Guatemala earthquake*. USGS Prof. Pap., 1204-A, 35.

Havenith, H.B., Vanini, M., Jongmans, D., Faccioli, E. (2003). *Initiation of earthquake-induced slope failure: influence of topographical and other site-specific amplification effects*. J. Seismol., 7: 397-412.

Hild, P., Ionescu, I.R., Lachand-Robert, T., Roşca, I. (2002). *The blocking of an inhomogeneous Bingham fluid. Applications to landslides.* Math. Model. Numer. Anal., 36: 1013–1026.

Howes, D.E., Kenk, E. (1988). *Terrain classification system for British Columbia.* Victoria, BC, Canada: Ministry of Environment, Ministry of Crown Lands, MOE Manual 10.

Hungr, O. (1995). *A model for the run-out analysis of rapid flow slides, debris flow, and avalanches.* Can. Geotech. J., 32: 610-623.

Hunt, J.E., Jarvis, I. (2017). *Prodigious submarine landslides during the inception and early growth of volcanic islands.* Nat. Com., 8: Article Number 2061, doi:10.1038/s41467-017-02100-3.

Hutchinson, J.N. (1986). *A sliding-consolidation model for flow slides.* Can. Geotech. J., 23: 115-126.

Iezzi, G., Caso, C., Ventura, G., Vallefuoco, M., Cavallo, A., Behrens, H., Mollo, S., Paltrinieri. D., Signanini, P., Vetere, F. (2014). *First documented deep submarine explosive eruptions at the Marsili Seamount (Tyrrhenian Sea, Italy): A case of historical volcanism in the Mediterranean Sea*. Gondwana Research, 25: 764–774

Italiano, F., De Santis, A., Favali, P., Rainone, M.L., Rusi, S., Signanini, P. (2014). *The Marsili Volcanic Seamount (Southern Tyrrhenian Sea).* Energies, 7: 4068-4086.

Ives, J.D., Messerli, B. (1981). *Mountain hazards mapping in Nepal. Introduction to an applied research project.* Mt. Res. Dev., 1: 223-230.

Keefer, D.K. (2002). *Investigating landslides caused by earthquakes - A historical review.* Surv. Geophys., 23: 473-510.

Keefer D.K., Wilson R.C., Mark R.K., Brabb E.E., Brown W.M., Ellen S.D., Harp E.L., Wieczorek G.F., Alger C.S., Zatkin R.S., 1987, *Real-time landslide warning during heavy rainfall,* Science, 238: 921-925

Keller, J., Leiber, J. (1974) *Sedimente, Tephralagen und Basalte der Südtyrrhenische Tiefsee-Ebene im Bereich des Marsili-Seeberges*, Meteor. Forschung, 19: 62-76.

Khazai, B., Sitar, N. (2004). *Evaluation of factors controlling earthquake-induced landslides caused by Chi-Chi earthquake and comparison with the Northridge and Loma Prieta events*. Eng. Geol., 71: 79-95.

Kienholz, H., Scheineider, G., Bischel, M., Grunder, M., Mool, P. (1984). *Mapping of mountain hazards and slope stability*. Mt. Res. Dev., 4: 247-266.

Krastel, S., Schmincke, H.U., Jacobs, C.L., Rihm, R., Le Bas, T.P., Alibes, B. (2001). *Submarine landslides around the Canary Islands.* J. Geophys. Res., 106: 3977-3997.

Larsen, M.C., Simon, A. (1993). *A rainfall intensity-duration threshold for landslides in a humid-tropical environment.* Puerto Rico. Geograph. Ann., Series A, Physical Geography, 75: 13-23.

Lenti, L., Martino, S. (2012). *The interaction of seismic waves with step-like slopes and its influence on landslide movements*. Eng. Geol., 126: 19-36.

Locat, J., Lee, H.J. (2002). *Submarine landslides: advances and challenges*. Can. Geotech. J., 39: 193-212.

Marani, M.P., Trua, T. (2002). *Thermal constriction and slab tearing at the origin of a super-inflated spreading ridge: Marsili volcano (Tyrrhenian Sea)*. J Geophys. Res., doi: 10.1029/2001JB000285.

Mazzanti, P., Bozzano, F. (2011). *Revisiting the February 6th Scilla (Calabria, Italy) landslide and tsunami by numerical simulation.* Mar. Geophys. Res., 32: 273–286.

McDougall, S., Hungr, O. (2004). *A model for the analysis of rapid landslide motion*. Can. Geotech. J., 41: 1084–1097.

Miller, D. (1995). *Coupling GIS with physical models to assess deep-seated landslide hazards*. Environ. Eng. Geosci., 1: 263-276.

Morelli, C. (1970). *Physiography, gravity and magnetism of the Tyrrhenian Sea*. Boll. Geof. Teor. Appl., 12: 275-288.

Murphy, W. (1995). *The geomorphological controls on seismically triggered landslides during the 1908 Straits of Messina earthquake, southern Italy*. Q.J. Eng. Geol., 28: 61-74.

Murty, T.S. (2003). *Tsunami Wave Height Dependence on Landslide Volume*. Pure Appl. Geophys., 160: 2147-2153.

Nelson Caine, T. (1976). *Summer rainstorms in an alpine environment and their influence on soil erosion, San Juan Mountains, Colorado*. Arct. Alp. Res., 8: 183-196.

Nicolosi, I., Speranza, F., Chiappini, M. (2006). *Ultrafast oceanic spreading of the Marsili Basin, southern Tyrrhenian Sea: Evidence from magnetic anomaly analysis.* Geology., 34: 717-720.

Nishimura, K., Morii, W. (1984). *An observed effect of topography on seismic ground motions*. Bull. Disas. Prev. Res. Inst., 34: 203-214.

Ocakoglu, F., Gokceoglu, C., Ercanoglu, M. (2002). *Dynamics of a complex mass movement triggered by heavy rainfall: a case study from NW Turkey.* Geomorph., 42: 329-341.

Okunishi, K., Sonoda, M., Yokoyama, K. (1999). *Geomorphic and environmental controls of earthquake-induced landslides*. Trans. Jpn. Geomorph. Union, 20: 351-368.

Pachauri, A.K., Pant, M. (1992). *Landslide hazard mapping based on geological attributes.* Eng. Geol., 32: 81-100.

Palacios, D., Garcia, R., Rubio, V., Vigil, R. (2003). *Debris flow in a weathered granitic massif: Sierra de Gredos, Spain*. Catena, 51: 115-140.

Paterson, M.S., Wong, T. (2005). *Experimental rock deformation - The brittle field (II ed.)*. Berlin: Springer.

Peccerillo, A., Taylor, S.R. (1976). *Geochemistry of Eocene calc-alkaline volcanic rocks from the Kastamonu area, northern Turkey*. Contrib. Mineral. Petrol., 58: 63-81.

Pelinovsky, E., Poplavsky, A. (1996). *Simplified model of tsunami generation by submarine landslides.* Phys. Chem. Earth, 21: 13-17.

Perla, R., Cheng, T.T., McClung, D.M. (1980). *A two-parameter model of snow-avalanche motion.* J. Glac., 26: 197-207.

Pontevivo, A., Panza, G. (2006). *The Lithosphere-Asthenosphere System in the Calabrian Arc and Surrounding Seas – Southern Italy.* Pure Appl. Geophys., 163: 1617-1659.

Pradhan S.P., Siddique T. (2019) *Mass Wasting: An Overview*. In: Pradhan S., Vishal V., Singh T. (eds) Landslides: Theory, Practice and Modelling. Advances in Natural and Technological Hazards Research, vol 50. Springer, 3-20.

Principe I., (1986) *La specola del filosofo: natura e storia nelle incisioni di Antonio Minasi*, Mapograf., Vibo Valentia.

Rohn, J., Fernandez–Steeger, T., Sidow, D., Czurda, K. (2003). *Rockfall triggers earthflow by undrained loading at Steinbach, Austria, April 1995*. Land. News, 14: 33-35.

Rovelli, A., Caserta, A., Marra, F., Ruggiero, V. (2002). *Can seismic waves be trapped inside an inactive fault zone? The case study of Nocera Umbra, Central Italy*. Bull. Seism. Soc. Am., 92: 2217-2232.

Sarconi, M. (1784). *Istoria de fenomeni del tremuoto avvenuto nelle Calabrie, e nel Valdemone nell'anno 1783.* Napoli: Reale Accademia delle Scienze e delle Belle Lettere di Napoli.

Sasaki, Y., Fujii, A., Asai, K. (2000). *Soil creep process and its role in debris slide generation - field measurements on the north side of Tsukuba Mountain in Japan.* Eng. Geol., 56: 163-183.

Sassa, K., Dang, K., Yanagisawa, H., He, B. (2016). *A new landslide-induced tsunami simulation model and its application to the 1792 Unzen-Mayuyama landslide-and-tsunami disaster*. Landslides, 13: 1405-1419.

Satake, K. (2001). *Tsunami modelling from submarine landslides*. Proc.Intern. Tsunami Symp, 2001.

Savelli, C., Schreider, A.A. (1991). *The opening processes in the deep Tyrrhenian basins of Marsili and Vavilov, as deduced from magnetic and chronological evidence of their igneous crust.* Tectonophysics, 190: 119-131.

Selli, R., Lucchini, F., Rossi, P., Savelli, C., Del Monte, M. (1977). *Dati geologici, petrochimici e radiometrici sui vulcani centro-tirrenici.* Giornale di Geologia, 2: 221-246.

Shigihara, Y., Godo, D., Imamura, F., Kitamura, Y., Matsubara, T., Takaoka, K., Ban, K. (2006). *Hydraulic and numerical study on the generation of a subaqueous landslide-induced tsunami along the coast*. Nat. Hazards, 39: 159-177.

Shoaei, Z., Ghayoumian, J. (2000). *Seimareh landslide, western Iran, one of the world's largest complex landslides*. Land. News, 13: 23-27.

Sidle R.C., Dhakal, A.S. (2002) *Potential effects of environmental change on landslide hazards in forest environments*. In: Sidle R.C. (ed.) Environmental change and geomorphic hazards in forests, IUFRO research series, 9. CABI Publishing, Wallingford, Oxen, 123–165.

Sigurdsson, H. (2015). *The encyclopedia of volcanoes,* San Diego, CA, USA, Elsevier Science.

Skempton, A.W., Hutchinson, J. (1969). *Stability of natural slopes and embankment foundations*. Soil Mech. & Fdn. Eng. Conf. Proc., Mexico, 291-340.

Sonoda, M. (1998). *A numerical simulation of displacement of weathered granite on a forest slope.* Trans. Jpn. Geomorph. Union, 19: 135-154.

Staudigel, H., Schimincke, H.U. (1984). *The Pliocene seamount series of La Palma/Canary Islands.* J. Geophys. Res., 89: 11195-11215.

Swanston, D.N. (1969). *Mass wasting in coastal Alaska*. USDA Forest Service Res. Paper, Juneau, Alaska.

Swanston, D. N., Swanson, F. J. (1976). *Timber harvesting, mass erosion, and steep land forest geomorphology in the Pacific Northwest*. In Coates, D.R., ed., Geomorphology and Engineering. Dowden, Hutchinson, and Ross, Inc. Stroudsburg, Pa, 199-221.

Tang, C., Grunert, J. (1999). *Inventory of landslides triggered by the 1996 Lijiang earthquake, Yunnan province, China.* Trans. Jpn. Geomorph. Union, 20: 335-349.

Tinti, S., Piatanesi, A. (1997). *Finite-element simulations of the 5 February 1783 Calabrian tsunami.* Phys. Chem. Earth, 12: 39-43.

Tinti, S., Bortolucci, E., Vannini, C. (1997). *A block-based theoretical model suited to gravitational sliding.* Nat. Hazards, 16: 1-28.

Tinti, S., Bortolucci, E., Armigliato, A. (1999). *Numerical simulation of the landslide-induced tsunami of 1988 on Vulcano Island, Italy*. Bull. Volcanol., 61: 121-137.

Tinti, S., Pagnoni, G., Armigliato, A., Zaniboni, F. (2005). *The 30 December 2002 landslide-induced tsunamis in Stromboli: sequence of the events reconstructed from the eyewitness accounts.* Nat. Hazards Earth Syst. Science, 5: 763-775.

Tinti, S., Pagnoni, G., Zaniboni, F. (2006). *The landslides and tsunamis of the 30th of December 2002 in Stromboli analysed through numerical simulations*. Bull. Volcanol., 68: 462-479.

Trollope, D.H. (1980). *The Vajont slope failure.* Rock Mech., 13: 71-88.

Trua, T., Serri, G., Marani, M.P., Renzulli, A., Gamberi, F. (2002). *Volcanological and petrological evolution of Marsili Seamount (southern Tyrrhenian Sea).* J. Volcan. Geotherm. Res., 114: 441-464.

Turner, A., Schuster, R. (1996). *Landslides - Investigation and Mitigation*. Special Report 247, National Res. Council, 129-177. Washington, D.C.: Academic Press.

Varnes, D.J. (1978) *Slope Movement Types and Processes*. In: Schuster, R.L. and Krizek, R.J., Eds., Landslides, Analysis and Control, Transportation Research Board, Special Report No. 176, National Academy of Sciences, 11-33.

Vivenzio, G. (1788). *Istoria de' tremuoti avvenuti nella provincia di Calabria ulteriore e nella città di Messina nell'anno 1783*. Stamperia Regale, Napoli.

Wang, Z., Shen, H. (1999). *Lagrangian simulation of one-dimensional dam-break flow*. J. Hydraul. Eng., 125: 1217–1220.

Ward, S.N. (2001). *Landslide tsunami*. J. Geophys. Res., 106: 11201-11215.

Ward, S.N., Day, S. (2001). *Cumbre Vieja Volcano - Potential collapse and tsunami at La Palma, Canary Islands.* Geophys. Res. Lett., 28: 3397-3400.

Watt, S.F.L., Jutzeler, M., Talling, P.J., Carey, S.N., Sparks, R.S.J., Tucker, M., Stinton, A.J., Fisher, J.K., Wall-Palmer, D., Hühnerbach, V., Moreton, S.G. (2015). *New insights into landslide processes around volcanic islands from Remotely Operated Vehicle (ROV) observations offshore Montserrat.* Geochem. Geophys. Geosyst., 16: 2240-2261.

Wentworth, C.K., (1943). *Soil avalanches on Oahu, Hawaii*. Geol. Soc. Am. Bull., 54: 53-64.

Wu, W., Sidle, R.C. (1995). *A distributed slope stability model for steep forested hillslopes*. Water Resour. Res., 31: 2097-2110.

Zaniboni, F. (2004). *Modelli numerici di evoluzione di frane con applicazione a casi di frane tsunamigeniche subaeree e sottomarine*. Bologna: University of Bologna.

Zaniboni, F., Tinti, S. (2014). *Numerical simulations of the 1963 Vajont landslide, Italy: application of 1D Lagrangian modelling*. Nat. Hazards, 70: 567-592.

Zaniboni, F., Armigliato, A., Tinti, S. (2016). *A numerical investigation of the 1783 landslide-induced catastrophic tsunami in Scilla, Italy*. Nat. Hazards, 82, S2, 455-470.

Zaniboni, F., Tinti, S. (2018). *The 1963 Vajont Landslide: A Numerical Investigation on the Sliding Surface Heterogeneity*, Pure App. Geoph., https://doi.org/10.1007/s00024-018-2023-6.

Zito, G., Mongelli, F., De Lorenzo, S., Doglioni, C. (2003). *Heat flow and geodynamics in the Tyrrhenian Sea.* Terra Nova, 15: 425-432.